

Report to:

National Earthquake Hazards Reduction Program,  
External Research Program  
Reston, VA

Award Number G11AP20039

Nonlinear Site Response and Seismic Compression at Vertical Array  
Strongly Shaken by 2007 Niigata-ken Chuetsu-oki Earthquake

by

Jonathan P. Stewart (PI)  
Eric Yee (Graduate Student)

University of California, Los Angeles  
Civil & Environmental Engineering Department

March, 2012

## **ACKNOWLEDGMENTS**

Support for this work was provided by the U.S. Geological Survey (USGS), Department of the Interior, under USGS award No. G11AP20039. The views and conclusions contained in this document are those of the authors and should not be interpreted as necessarily representing the official policies, either expressed or implied, of the U.S. Government.

## ABSTRACT

USGS/NEHRP Award No. G11AP20039

### NONLINEAR SITE RESPONSE AND SEISMIC COMPRESSION AT VERTICAL ARRAY STRONGLY SHAKEN BY 2007 NIIGATA-KEN CHUETSU-OKI EARTHQUAKE

PI: Jonathan P. Stewart  
Civil & Environmental Engineering Department  
University of California  
Los Angeles, CA 90095-1593  
Tel: (310) 206 2990 Fax: (310) 206 2222  
[jstewart@seas.ucla.edu](mailto:jstewart@seas.ucla.edu)

Strong ground motions from the  $M_w$  6.6 2007 Niigata-ken Chuetsu-oki earthquake were recorded by a free-field downhole array installed near the Service Hall at the Kashiwazaki-Kariwa nuclear power plant. Site conditions at the array consist of about 70 m of medium-dense sands overlying clayey bedrock, with ground water located at 45 m. Ground shaking at the bedrock level had geometric mean peak accelerations of 0.55 g which is reduced to 0.4 g at the ground surface, indicating nonlinear site response. Ground settlements of approximately  $15 \pm 5$  cm occurred at the site. A site investigation was performed to develop relevant soil properties for ground response and seismic compression analysis, including shear wave velocities, shear strength, relative density, and modulus reduction and damping curves.

Ground response analysis of relatively weak motion aftershock data provides good matches of the observed resonant site frequencies and amplification levels, suggesting that the velocity profile and assumption of 1D response may be reasonable over the frequency range of interest. Initial analysis of the aftershock data was performed using equivalent-linear and nonlinear ground response procedures in which soil backbone curves are matched to test data for modest strain levels  $< \sim 0.5\%$ . These analyses over-predict high frequency ground response, suggesting that the laboratory-based small strain damping level is too low for field conditions. Increasing the small strain damping to about 2-5% in the sand layers provides improved results. Subsequent ground response analysis of strong motion data produces a strain localization phenomenon where large strains develop at a depth having a velocity contrast. Accordingly, we introduce a

procedure to modify the large-strain portion of backbone curves to asymptotically approach the shear strength. When implemented in nonlinear and equivalent linear ground response, the strain localization phenomenon is removed, strains in the upper portion of the soil profile are increased, and predicted ground motions match observations reasonably well.

Measured relative densities ( $D_R$ ) at the site range from approximately 40% (from tube samples) to 65% (from SPT correlations). A material specific volumetric strain material model for that range of  $D_R$  was developed, which when coupled with the shear strain demands from the ground response analysis, predicts ground settlements ranging from 8-12 cm for horizontal ground shaking and 12-18 cm when vertical ground motions are considered. Those settlement estimates are reasonably consistent with the observations from the site.

## TABLE OF CONTENTS

<b>ACKNOWLEDGMENTS .....</b>	<b>II</b>
<b>ABSTRACT.....</b>	<b>III</b>
<b>TABLE OF CONTENTS .....</b>	<b>V</b>
<b>LIST OF FIGURES .....</b>	<b>VII</b>
<b>LIST OF TABLES .....</b>	<b>XI</b>
<b>1. INTRODUCTION .....</b>	<b>1</b>
<b>2. PREVIOUS STUDIES .....</b>	<b>6</b>
2.1 Nonlinear Site Response .....	6
2.2 Seismic Compression Case Studies .....	10
<b>3. SITE CHARACTERIZATION.....</b>	<b>16</b>
3.1 Results of geotechnical exploration (current and prior studies) .....	16
3.2 Laboratory testing .....	19
3.2.1 Index tests.....	19
3.2.2 Relative densities.....	19
3.2.3 Shear strength and modulus reduction and damping relations.....	19
3.2.4 Cyclic volume change .....	21
<b>4. GROUND MOTION DATA FROM SERVICE HALL ARRAY .....</b>	<b>27</b>
<b>5. GROUND RESPONSE ANALYSIS .....</b>	<b>33</b>
5.1 Dynamic soil properties for analysis.....	33
5.2 Ground response analysis using aftershock data.....	39
5.3 Initial ground response analysis using main shock recordings .....	49
5.4 Revised ground response analysis considering strength adjusted backbone curves and increased damping.....	53
5.4.1 Modification of backbone curve to capture shear strength .....	53
5.4.2 Effects of modified backbone curves on analysis results.....	55
5.4.3 Damping adjustment .....	59
<b>6. GROUND FAILURE ANALYSIS .....</b>	<b>64</b>
6.1 Potential for liquefaction at depth.....	64

6.2 Seismic Compression .....	65
<b>7. SUMMARY AND CONCLUSIONS.....</b>	<b>69</b>
<b>REFERENCES.....</b>	<b>72</b>
<b>APPENDIX A: DETAILED BORING LOG (ELECTRONIC SUPPLEMENT).....</b>	<b>75</b>
<b>APPENDIX B: ACCELERATION, VELOCITY, AND DISPLACEMENT HISTORY FOR MAIN SHOCK .....</b>	<b>76</b>
<b>APPENDIX C: ACCELERATION, VELOCITY, AND DISPLACEMENT HISTORY FOR AFTERSHOCK L .....</b>	<b>85</b>
<b>APPENDIX D: ACCELERATION, VELOCITY, AND DISPLACEMENT HISTORY FOR AFTERSHOCK S .....</b>	<b>94</b>

## LIST OF FIGURES

Figure 1.1 Map of Kashiwazaki area showing location of KKNPP site relative to fault rupture plane by Miyake et al. (2010). Shading on fault plane indicates slip in meters. ....	1
Figure 1.2 Map of Kashiwazaki-Kariwa nuclear power plant showing locations of downhole arrays and geometric mean peak accelerations from 2007 Niigata-ken Chuetsu-oki earthquake. Peak accelerations are shown for surface ('sur') and bedrock ('br') conditions. 3	
Figure 1.3 Geologic log at SHA site including instrument locations and results of penetration and suspension logging geophysical testing .....	4
Figure 1.4 Photographs of (a) raised pile at vertical array, showing ground settlement; and (b) settlement around Service Hall building.....	5
Figure 2.1 Acceleration histories for data from the 2004 Parkfield earthquake and simulation results from site response program DeepSoil. Results are shown for two horizontal directions and two elevations (V1, ground surface; D2, 10-m depth) with the recorded input motions at elevation D3 (Kwok et al. 2008).....	7
Figure 2.2 Comparison of interpreted soil behavior by extracting soil parameters using two different methods, with curves from laboratory tests (Anderson and Tang 1989) and those from system identification (Elgamal et al. 2001), Lotung array (Tsai and Hashash 2009).....	8
Figure 2.3 Transfer functions at two stations, illustrating inter-event variability: (a) IWTH25 is characteristic of a site with a large degree of inter-event variability, and (b) IWTH05 is characteristic of a site with low inter-event variability. The median prediction of the transfer function is shown as a black line, and the 95% confidence band is shown in gray (Baise et al. 2011). ....	9
Figure 2.4 Transfer functions at two stations, illustrating goodness-of-fit: (a) IWTH04 is characteristic of a site where the SH1D model accurately predicts the transfer functions, and (b) IWTH12 is characteristic of a site where the SH1D model poorly predicts a transfer function (Baise et al. 2011).....	9
Figure 2.5 Jensen Filtration Plant profile (Pyke et al. 1975). ....	10

Figure 2.6 Comparison of settlements under (a) components and combined random motions and (b) in three-dimensional shake table tests (Pyke et al. 1975). .....	11
Figure 2.7 Plan and settlement of Santa Clarita Site B (Stewart et al. 2004). .....	12
Figure 2.8 (a) Seismic compression and (b) variation of normalized vertical strain with number of cycles of soil from Site B (Stewart et al. 2004).....	13
Figure 2.9 Vertical profiles of shear strain from site response analyses (top frame) and lateral profiles of observed and calculated settlement (bottom frame) along a cross section for site B (Stewart et al. 2004). .....	14
Figure 2.10 Schematic of observed ground deformation at a highway embankment site (Wartman et al. 2003). .....	15
Figure 3.1 Variation with depth of energy ratio in standard penetration tests.....	18
Figure 3.2 Modulus reduction and damping curves from resonant column and torsional shear tests performed on specimens from four samples.....	21
Figure 3.3 Results of simple shear tests showing cyclic volume change characteristics of sandy materials in upper 70 m of SHA site. ....	23
Figure 3.4 Comparison of parameter $a$ for KKNPP sand with slope parameter $b = 1.2$ against the clean sand model by Duku et al. (2008). .....	24
Figure 3.5 Simple shear results from applying ground motions at 8.2 m depth taken from site response analyses and the resultant settlement time history. FN and FP ground motions were also applied separately. ....	26
Figure 4.1 Main shock velocity histories from the upper three instruments at the SHA site rotated into the fault normal (FN) and fault parallel (FP) directions. ....	29
Figure 4.2 Pseudo acceleration response spectra for the three components of recorded main shock ground motions at SHA site. ....	30
Figure 4.3 Surface-to-rock (2.4 m / 99.4 m) transfer functions and surface (2.4 m) H/V spectral ratios for main shock and aftershock recordings .....	32
Figure 5.1 Variation of pseudo reference strain with mean confining pressure from RCTS tests (this study), previous RCTS tests (neighboring site), and model predictions. ....	35



Figure 5.2 Values of pseudo reference strain used for analysis as function of with confining pressure and depth through the soil column. ....	37
Figure 5.3 Comparison of the Darendeli (2001) and Menq (2003) (a) modulus reduction and (b) damping curve models to sample test data from 20 m deep. Resultant modulus reduction and damping curves are labeled as “Model”. ....	38
Figure 5.4 Comparison of Menq (2003) minimum damping and the range of damping values at shear strains less than 0.05% from RCTS testing. ....	39
Figure 5.5 Results of EQL and NL ground response analyses for aftershock L. ....	42
Figure 5.6 Peak strain profiles from EQL and NL analyses for aftershock L. ....	43
Figure 5.7 Peak accelerations from EQL and NL analyses for aftershock L. ....	44
Figure 5.8 Results of EQL and NL ground response analyses for aftershock S. ....	45
Figure 5.9 Peak strain profiles from EQL and NL analyses for aftershock S. ....	46
Figure 5.10 Peak accelerations from EQL and NL analyses for aftershock S. ....	47
Figure 5.11 Transfer function and coherence for the main shock and two aftershocks. ....	47
Figure 5.12 Response spectra at 5% damping for aftershock L and EQL analysis results for varying levels of small strain damping. ....	48
Figure 5.13 Response spectra at 5% damping for aftershock S and EQL analysis results for varying levels of small strain damping. ....	49
Figure 5.14 Results of EQL and NL ground response analyses using increased damping ( $D_{min}=2\%$ ). ....	51
Figure 5.15 Peak strain profiles from EQL and NL analyses with increased damping ( $D_{min}=2\%$ ). ....	52
Figure 5.16 Comparison of backbone curve from fault normal nonlinear site response analysis at 50.8 m depth and estimated drained shear strength. ....	52
Figure 5.17 Diagram for constructing shear strength adjusted modulus reduction curves. ....	54
Figure 5.18 Comparison of the original and strength adjusted (a) modulus reduction and (b) damping models for the layer of soil containing the first sensor, (c) modulus reduction and	

(d) damping models for a layer at 8.2 m depth, and (e) modulus reduction and (f) damping models for the layer of soil containing the second sensor. ....	56
Figure 5.19 Results of strength adjusted EQL and NL ground response analyses. ....	57
Figure 5.20 Peak strain profiles from strength adjusted EQL and NL analyses. ....	58
Figure 5.21 Peak accelerations from strength adjusted EQL and NL analyses. ....	59
Figure 5.22 Response spectra at 5% damping for main shock and NL analysis results using strength adjusted backbone curves and varying levels of small strain damping .....	60
Figure 5.23 Peak accelerations from increased damping on strength adjusted NL analyses. ....	61
Figure 5.24 Results of strength adjusted EQL and NL ground response analyses with increased damping. ....	62
Figure 5.25 Peak strain profiles from strength adjusted EQL and NL analyses with increased damping. ....	63
Figure 6.1 Relationship between shear strain amplitude, $\gamma_c$ , and number of cycles, $N$ , to cause selected amounts of vertical strain, $\varepsilon_v$ . ....	66
Figure 6.2 Number of cycles from strength adjusted EQL analysis. ....	66
Figure 6.3 Sample effective strain demand profiles, vertical strain profiles, and resultant settlements from a site specific analysis for $D_R = 40$ and 65%. ....	68

## LIST OF TABLES

Table 3.1 Summary of soil index tests, triaxial compression shear strength tests, and resonant column-torsional shear tests for dynamic soil properties. ....	20
Table 3.2 Suites of cyclic simple shear tests and regressed parameters. ....	24
Table 4.1 Ground motions used for this study. ....	28
Table 4.2 Filter frequencies applied to vertical array data. ....	28
Table 4.3 PGA and PGV from rotated motions. ....	29

# 1. Introduction

The  $M_w$  6.6 Niigata-ken Chuetsu-oki earthquake occurred on July 16, 2007 off the west coast of Niigata Prefecture, Japan. An overview of the damage from this important earthquake is provided by Kayen et al. (2009) and references therein. As shown in Figure 1.1, the main shock ruptured a buried reverse-slip fault, rupturing up-dip from a focal depth of 9 km. The focal mechanism for this event, based on source inversions by Miyake et al. (2010), has conjugate fault planes with a strike of  $34^\circ$  and dips of  $54^\circ$  to the northwest and  $36^\circ$  to the southeast. The southeast-dipping plane is preferred (and is shown in Figure 1.1) based on asperities analysis, the aftershock pattern observed from ocean-bottom seismometers, and results of reflection surveys (Miyake et al., 2010).

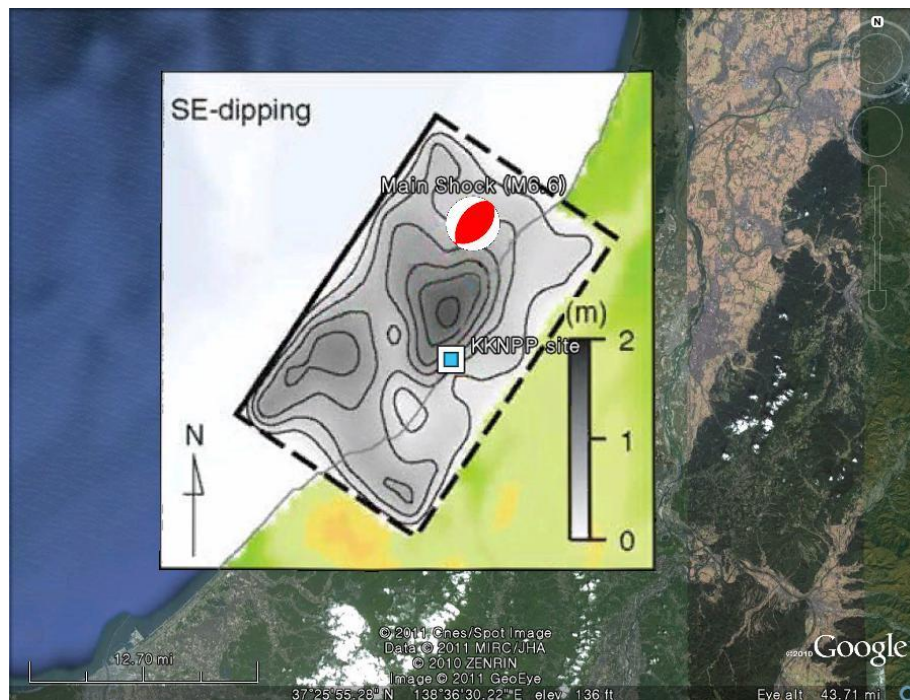


**Figure 1.1 Map of Kashiwazaki area showing location of KKNPP site relative to fault rupture plane by Miyake et al. (2010). Shading on fault plane indicates slip in meters.**

As shown in Figure 1.1, the Kashiwazaki-Kariwa Nuclear Power Plant (KKNPP) is located on the hanging wall of the fault above a region of relatively high slip. Accordingly, the distance of this site to the surface projection of the fault (the Joyner-Boore distance) is  $R_{jb} = 0$  km, whereas the rupture distance is  $R_{rup} = 16$  km. As described in Tokimatsu et al. (2009), the KKNPP suspended operations due to earthquake damage until partially re-opening in 2009. Figure 1.2 shows a map of the KKNPP including its seven generators (marked as Units 1-7) and three free-field downhole seismic arrays near Units 1 and 5 and the Service Hall. Recordings from the Unit 1 and 5 downhole arrays were overwritten with aftershock data and only peak accelerations remain. The Service Hall Array (SHA) recordings are intact, and as shown in Figure 1.3, this array contains four three-component accelerometers at depths of 2.4 m (Holocene dune sand), 50.8 m (Pleistocene Banjin Formation), 99.4 m (Pliocene Nishiyama Formation), and 250 m (Pliocene Nishiyama Formation) (Tokimatsu and Arai, 2008). Figure 1.2 also shows the peak near surface geometric mean accelerations, which are 0.54, 0.72, and 0.40 g for vertical arrays at Unit 1, 5, and SHA respectively. Motions near the top of the Pliocene bedrock (Nishiyama formation) were 0.69, 0.41, and 0.52 g for vertical arrays at Unit 1, 5, and SHA respectively. The lowering of peak accelerations from bedrock to surface in the Unit 1 array and SHA indicates nonlinear site response for those soil columns. In contrast, downhole to surface motions are amplified in the Unit 5 array, which is in rock. The data shown in Figure 1.2 for instruments other than the SHA are taken from Tokimatsu (2008) and TEPCO (2007).

Access to the KKNPP site was limited following the earthquake, but reconnaissance was performed by Sakai et al. (2009) and Tokimatsu (2008), who observed widespread settlement both in free-field areas and adjacent to reactor structures. Settlement near the reactors was especially large and damaged utility connections. The settlements occurred in unsaturated sandy soils, some natural and some backfilled. In the vicinity of the SHA, two lines of evidence suggest settlements of approximately  $15 \pm 5$  cm. First, as shown in Figure 1.4a, the top of one of the deep steel pipes housing a vertical array instrument extended above the ground surface by 15 cm. We infer that the pipe, whose toe is founded in competent materials, remained essentially in place while the surrounding soil settled. We are uncertain why other deep pipes housing different accelerometers in the array did not show similar extensions above the ground surface. Second, as shown in Figure 1.4b, settlement was evident around the pile-supported Service Hall building structure by amounts ranging from 10-25 cm. Settlements were larger immediately adjacent to

the structure, presumably because of poorly compacted backfill around the basement walls for this structure.

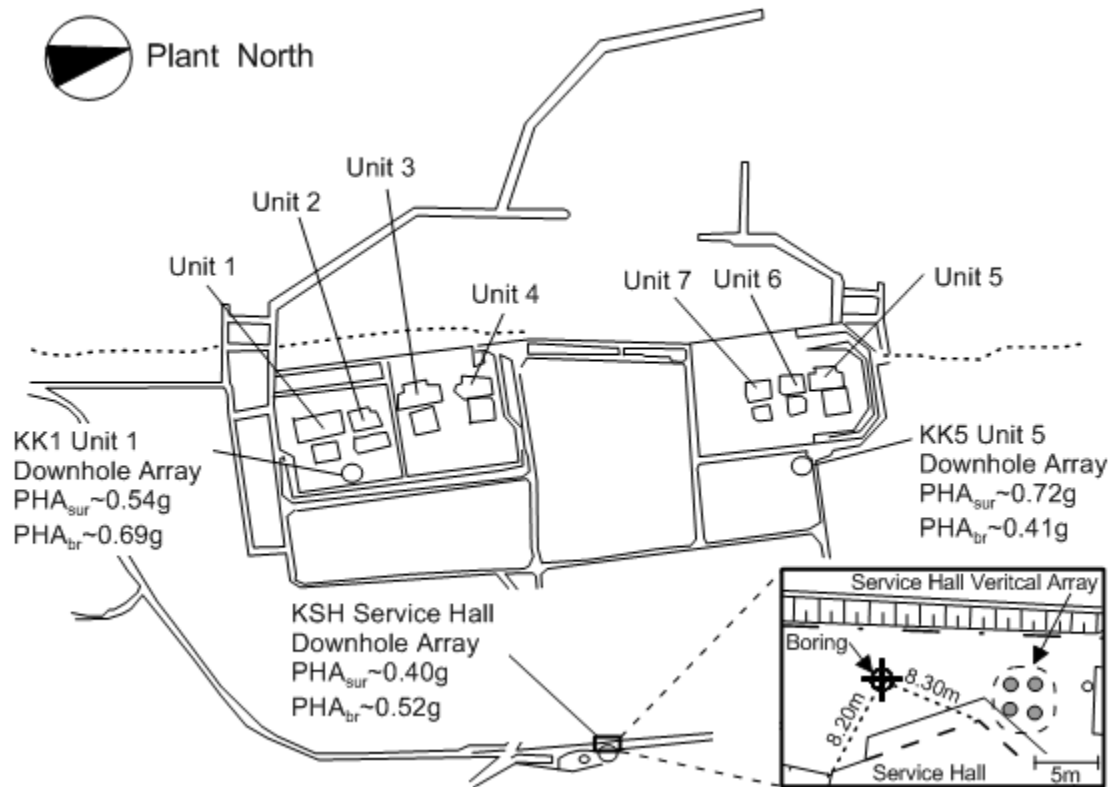


**Figure 1.2 Map of Kashiwazaki-Kariwa nuclear power plant showing locations of downhole arrays and geometric mean peak accelerations from 2007 Niigata-ken Chuetsu-oki earthquake. Peak accelerations are shown for surface ('sur') and bedrock ('br') conditions.**

The data set from the SHA site at KKNPP is uniquely valuable in two respects. First, prior to the 2011 Tohoku Japan earthquake, the SHA recorded the strongest motions for a vertical array in soil. Vertical array recordings enable validation of ground response analysis codes and studies of dynamic soil behavior under in situ conditions (e.g., Zeghal et al., 1995; Cubrinovski et al. 1996; Kwok et al., 2008; Tsai and Hashash, 2009). With the exception of a few arrays in liquefiable materials, previous vertical array data has generally been at low to modest shaking levels that would not be expected to induce large shear strains associated with strongly nonlinear soil behavior. It is the nonlinear condition where the need for code validation is greatest, and the strong ground motions at SHA are known to have produced nonlinear site response.

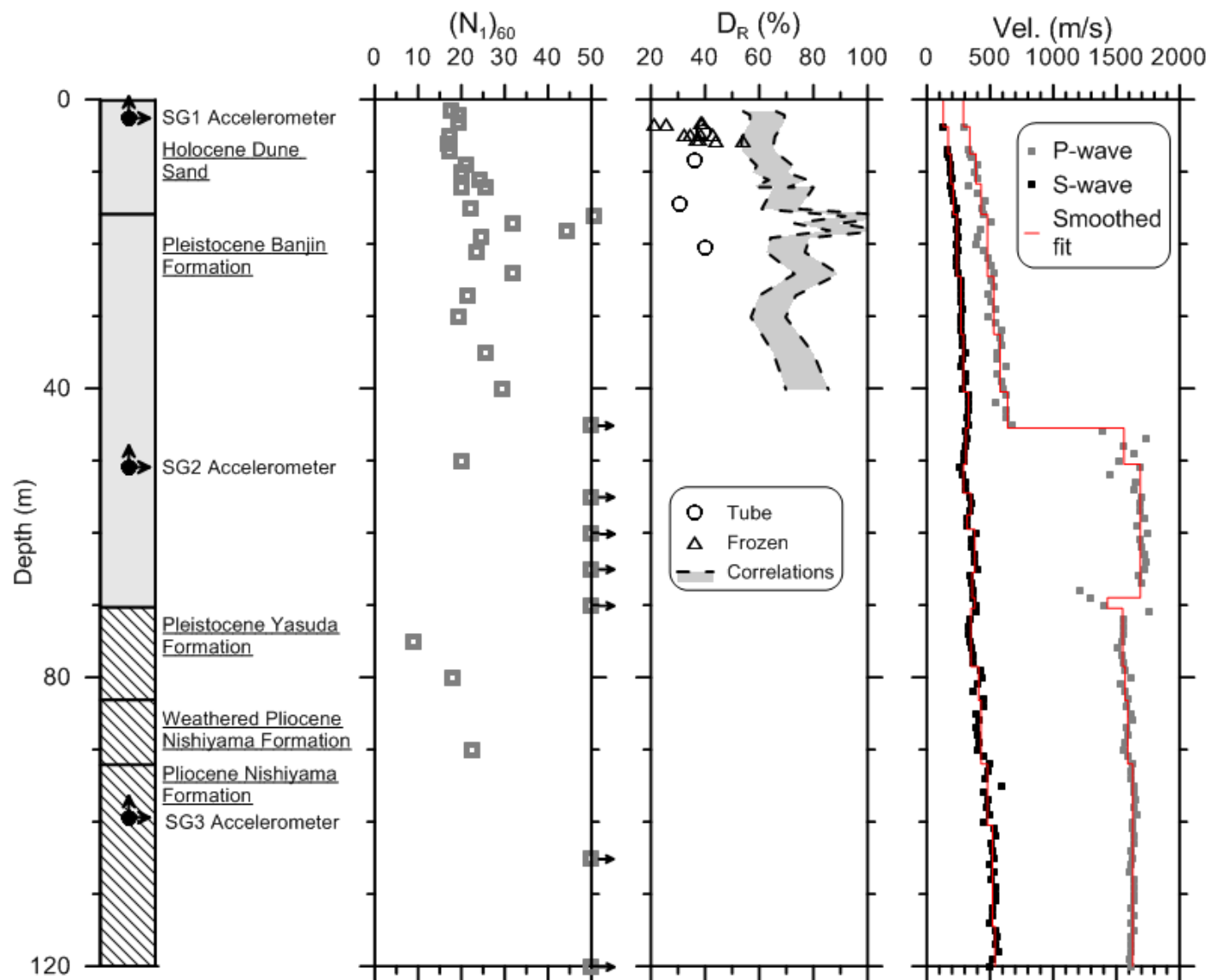
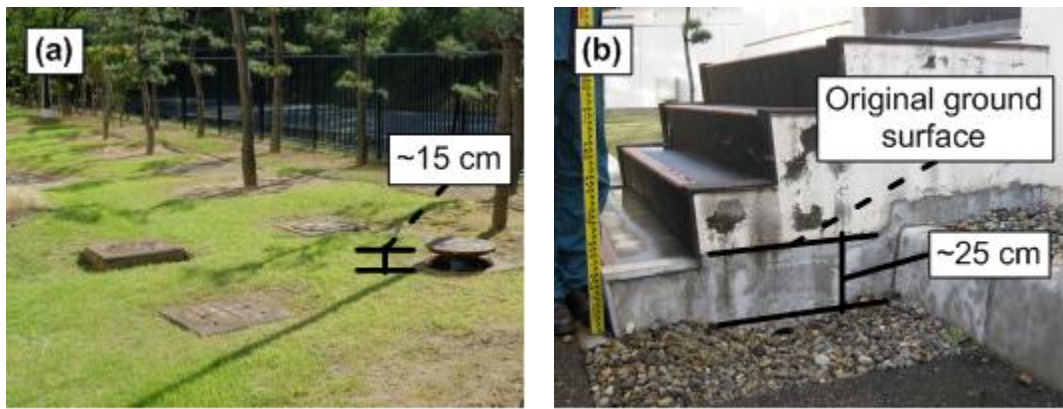


Figure 1.3 Geologic log at SHA site including instrument locations and results of penetration and suspension logging geophysical testing

Second, while ground settlements in unsaturated soils have been observed previously in strongly shaken filled ground (e.g., Pyke et al., 1975; Stewart et al., 2002; Wartman et al., 2003), there are very few cases in which the pre-earthquake ground elevations are known so that grade changes induced by the earthquake can be measured (Stewart et al., 2004). Moreover, there are no previous seismic compression case studies in which ground motions were recorded at the site. Because the SHA site has both reasonably well-defined ground settlements and vertical array recordings, it is a unique resource for validating seismic compression analysis procedures (e.g., Tokimatsu and Seed, 1987; Duku et al., 2008).



**Figure 1.4 Photographs of (a) raised pile at vertical array, showing ground settlement; and (b) settlement around Service Hall building.**

Following this introduction, we provide a brief review of previous studies on nonlinear site response at vertical array sites and seismic compression case histories. We then describe the geotechnical characterization of materials from the SHA site and the recorded ground motions followed by a description of equivalent linear and nonlinear ground response analyses and their ability to replicate the observed near-surface recordings. Using shear strains predicted from these analyses, we then estimate ground settlement based on material-specific testing of the shallow soil materials at the SHA site and compare those predictions to the observed settlement of  $15 \pm 5$  cm.



## **2. Previous Studies**

It is important to place the value of this case history in context by comparing it to previously available case studies for nonlinear site response and seismic compression. This is undertaken in the following sections.

### **2.1 NONLINEAR SITE RESPONSE**

With regard to nonlinear site response, Stewart and Kwok (2008) led a multi-investigator project developing parameter selection and code usage protocols for nonlinear ground response analysis. The codes/protocols were tested against the best available vertical array data not involving soil liquefaction (because the codes are for total stress analysis). The arrays utilized were a series of stiff soil sites in Japan (Kiknet), the Lotung array in Taiwan (soft silts), the La Cienega array in California (soft clay), and the Turkey Flat array in California (shallow, stiff soil). At the Turkey Flat site (Kwok et al., 2008), peak velocities from the 2004  $M_w$  6.0 Parkfield earthquake were in the range of 7-8 cm/s and calculated peak ground strains were as large as  $10^{-2}\%$ . Figure 2.1 compares predicted and observed acceleration histories at the surface and an intermediate depth, showing good comparisons.

At the other sites considered by Stewart and Kwok (2008), peak velocities were 11-18 cm/s (La Cienega), 5-6 cm/s (Kiknet), and 17-31 cm/s (Lotung). Ground strains from these other sites were of the same order as those at Turkey Flat (slightly larger at Lotung). The level of strain is important, because one of the key attributes of the parameter selection protocols is the manner by which soil backbone curves are extended from the small strain range where dynamic soil testing is reliable (strains  $< 0.5\%$ ) to relatively large strains associated with the shear strength (1% or more). This is of considerable practical significance, because it is for these large strain problems that nonlinear ground response analysis procedures are selected for use in practice in lieu of simpler equivalent-linear methods. The SHA site provides the first example of highly

nonlinear soil behavior not involving liquefiable soils in which the induced ground strains are likely in the range of 1%.

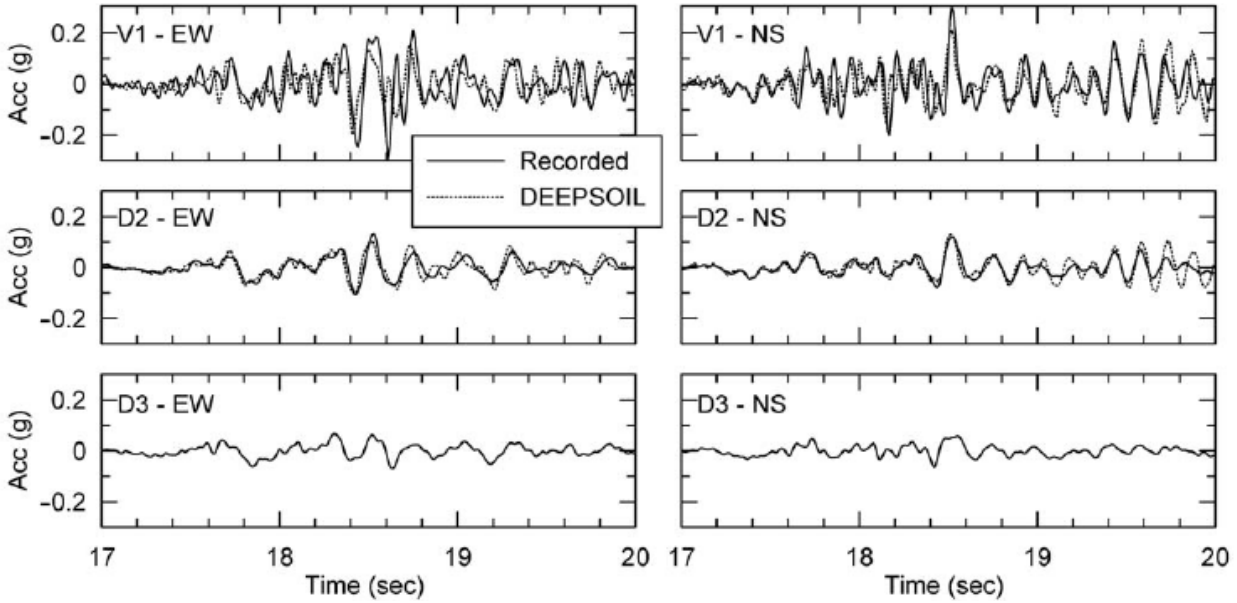


**Figure 2.1 Acceleration histories for data from the 2004 Parkfield earthquake and simulation results from site response program DeepSoil. Results are shown for two horizontal directions and two elevations (V1, ground surface; D2, 10-m depth) with the recorded input motions at elevation D3 (Kwok et al. 2008).**

Tsai and Hashash (2009) used some of the same vertical array data as Stewart and Kwok (2008) in a neural network based inverse analysis of vertical arrays to extract soil properties. Their analyses were not constrained by model-based assumptions of soil behavior and hence hold the potential to provide new insights into in situ soil behavior. However, the approach does have the potential to map modeling errors unrelated to soil behavior (e.g., lack of 1D response) into inverted soil properties. The approach was applied to the Lotung and La Cienega arrays. Shear wave velocity models were slightly adjusted from data in the “learning” process and stress-strain loops were extracted. As shown in Figure 2.2, modulus reduction and damping curves were then computed from the loops, which demonstrate stronger nonlinearity than lab-based curves (lower modulus reduction, higher damping). The higher damping is also in agreement with system identification of Lotung data from Elgamal et al. (2001). We note in Figure 2.2 that the damping increase from the vertical array analysis seems to affect the small strain damping ( $D_{min}$ ) but not the overall shape of the damping-strain relationship.

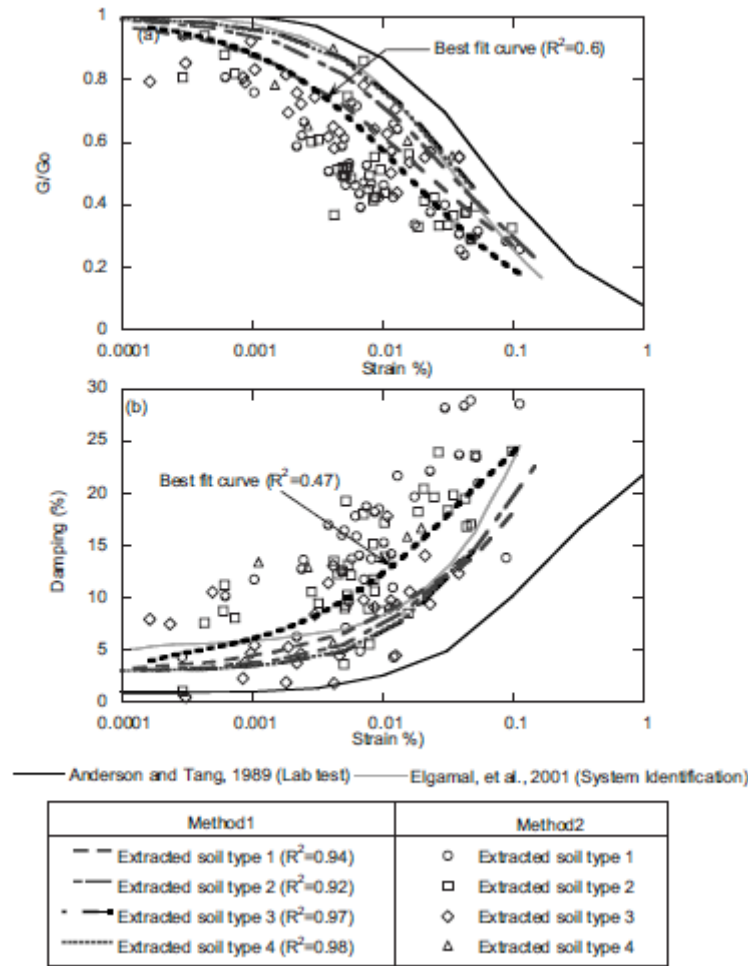


**Figure 2.2 Comparison of interpreted soil behavior by extracting soil parameters using two different methods, with curves from laboratory tests (Anderson and Tang 1989) and those from system identification (Elgamal et al. 2001), Lotung array (Tsai and Hashash 2009).**

Baise et al. (2011) examine weak motion data from a large number of sites in the Kiknet vertical array network in Japan to investigate event-to-event consistency in site transfer functions (surface/downhole) and the degree to which those transfer functions are compatible with theoretical models for 1D vertical shear wave propagation (SH1D). Figure 2.3 shows examples of small and large event-to-event variability in weak motion amplification from their analysis, while Figure 2.4 shows examples of good and poor fit of the SH1D model to data. Of the 74 sites considered, only 11 had good fits to the SH1D model, although an unknown number of the misfits may be simply associated with modest errors in the shear wave velocity profile. Nonetheless, large misfits as shown in Figure 2.4 (right side) indicate a clearly more complex

site response than SH1D. Sites such as those would not be good candidates for calculating 1D nonlinear site response for comparison to observation.

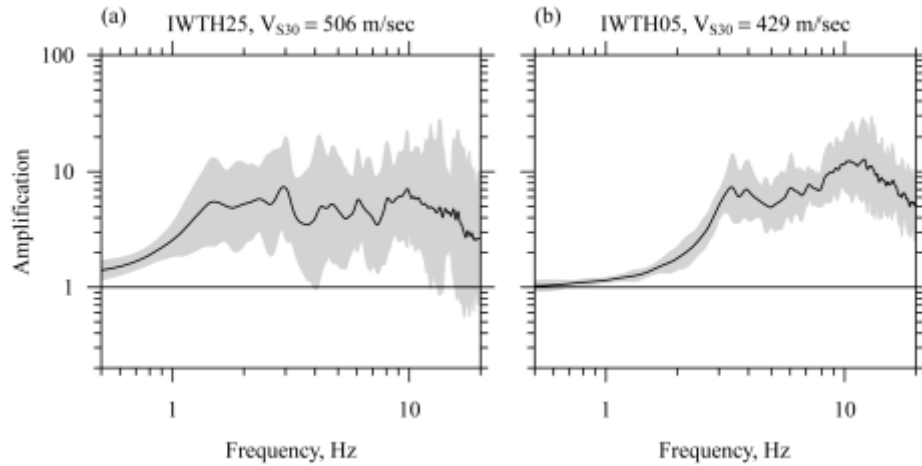


**Figure 2.3 Transfer functions at two stations, illustrating inter-event variability: (a) IWTH25 is characteristic of a site with a large degree of inter-event variability, and (b) IWTH05 is characteristic of a site with low inter-event variability. The median prediction of the transfer function is shown as a black line, and the 95% confidence band is shown in gray (Baise et al. 2011).**

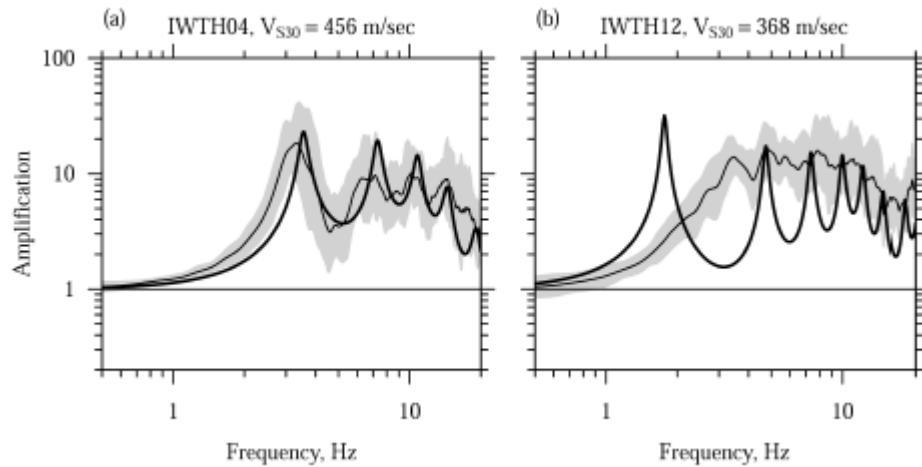


**Figure 2.4 Transfer functions at two stations, illustrating goodness-of-fit: (a) IWTH04 is characteristic of a site where the SH1D model accurately predicts the transfer functions, and (b) IWTH12 is characteristic of a site where the SH1D model poorly predicts a transfer function (Baise et al. 2011).**

## 2.2 SEISMIC COMPRESSION CASE STUDIES

There are several well documented field case histories of settlements from seismic compression. These include the Jensen Filtration Plant shaken by the 1971 San Fernando earthquake (Pyke et al., 1975), two sites in Santa Clarita shaken by the 1994 Northridge earthquake (Stewart et al., 2004), damaged embankments from the 2001 Southern Peru earthquake (Wartman et al., 2003), and ground failure patterns from the 2003 Colima earthquake (Wartman et al., 2005).

The Joseph Jensen Filtration Plant site in Granada Hills, California was formed by a cut-and-fill operation. The compacted clayey sand fill was up to 17 m thick overlying 1.5-6 m of alluvium. The groundwater table was located in the alluvial layer, which liquefied from estimated peak horizontal accelerations of about 0.5-0.6 g from the  $M_w$  6.6 San Fernando earthquake. As shown in Figure 2.5, recorded settlements were about 12.7 cm along a survey baseline. However, Pyke et al. (1975) attributed some of the observed settlement to lateral spreading and estimated settlements due to seismic compression to be around 8.9-10.2 cm, which was about 0.7% of the fill thickness.

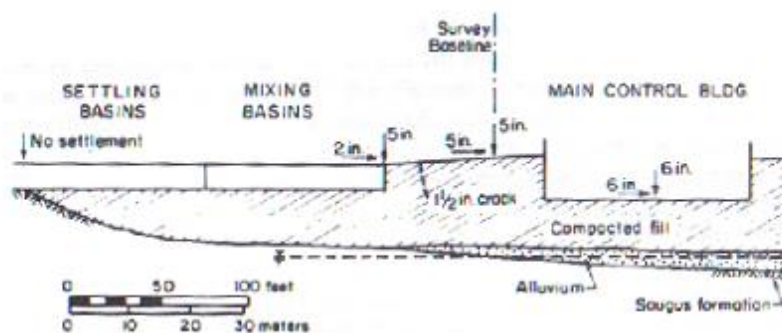


**Figure 2.5 Jensen Filtration Plant profile (Pyke et al. 1975).**

In their analysis, Pyke et al. (1975) conducted a series of strain-controlled cyclic simple shear tests on the site fill material. Subsurface investigations revealed the clayey sand fill to be uniformly compacted with an average dry density of  $1,937 \text{ kg/m}^3$  and an average water content of 10%. This equated to a relative compaction of approximately 92%. The strain histories from their site response analysis were used to determine the equivalent number of uniform shear strain cycles, which they found to be five with a shear strain of two-thirds the peak value. Applying these values to the simple shear tests produced an estimate of settlement that was approximately one third of that observed in the field. As shown in Figure 2.6a, Pyke et al. (1975) went on to

conduct multi-directional shake table tests and found that the total settlement caused by the combined horizontal motions are approximately equal to the sum of the settlements caused by the horizontal motions acting separately. As shown in Figure 2.6b, the application of vertical shaking combined with horizontal further increased measured settlements by amounts ranging from approximately 20 to 50% for effective vertical accelerations ranging from 0.15-0.3g. Considering this, Pyke et al. (1975) applied a correction factor for multi-directional loading which increased their computed settlement to within the range of observed field settlements.

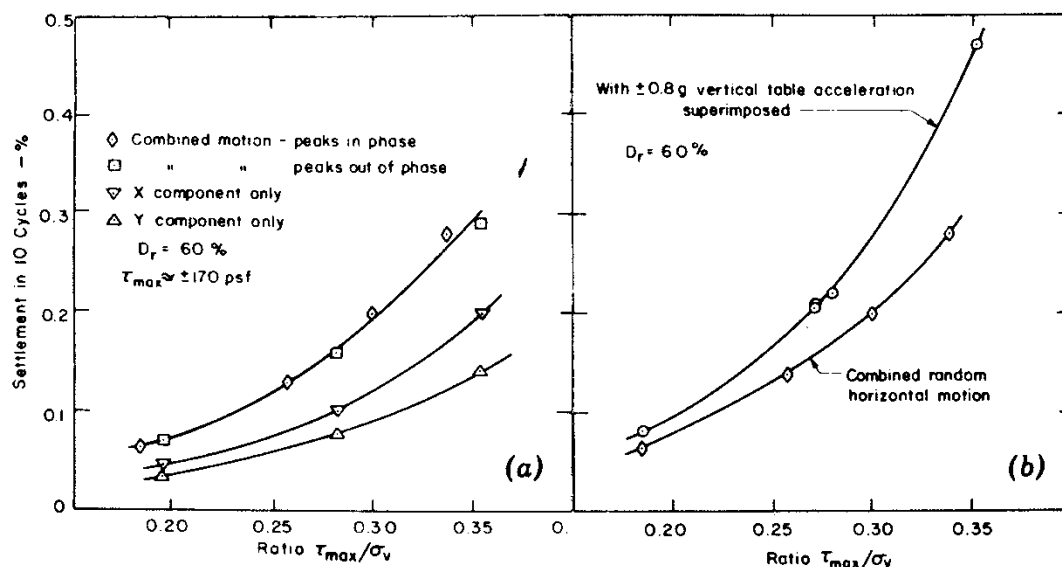


**Figure 2.6 Comparison of settlements under (a) components and combined random motions and (b) in three-dimensional shake table tests (Pyke et al. 1975).**

After the 1994  $M_w$  6.7 Northridge earthquake, two sites in Santa Clarita, California (denoted Sites A and B) had settlements from seismic compression that could be reliably estimated. For Santa Clarita Site A, the soils consisted of a sandy clay and clayey sand fill up to 24 m thick underlain by shallow alluvium and rock. Soil conditions show the fill generally being compacted to approximately 88% modified Proctor relative compaction and dry of optimum. Stewart et al. (2004) estimated peak horizontal accelerations of 0.5-0.7 g with measured settlements of up to 22 cm from pre and post-earthquake surveys. For Santa Clarita Site B, the soils consisted of a silty sand fill 15-30.5 m thick lying over rock. Soil conditions indicate modified Proctor relative compactions of about 92-93% near the surface and about 95% at depth. Stewart et al. (2004) estimated peak horizontal accelerations of 0.8-1.2 g with measured

settlements of 1.3-6.1 cm from pre and post-earthquake surveys. Figure 2.7 shows a plan of Site B indicating fill depths and measured settlements.

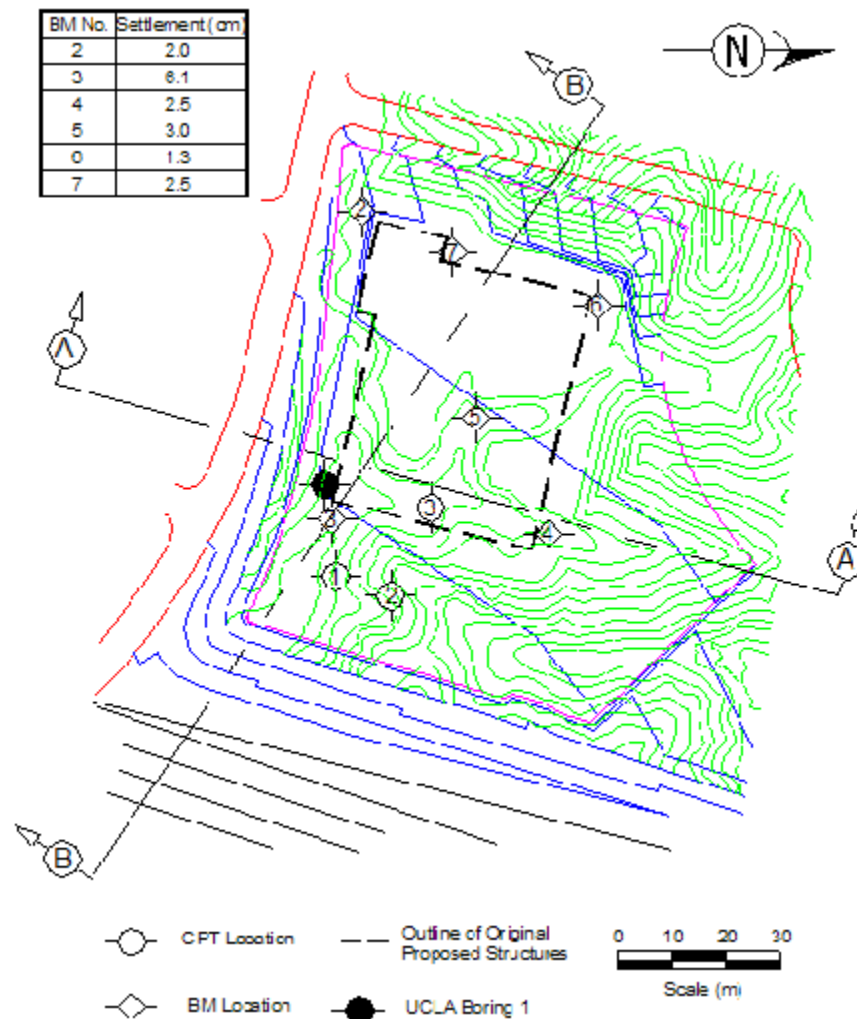


**Figure 2.7 Plan and settlement of Santa Clarita Site B (Stewart et al. 2004).**

In their analysis, Stewart et al. (2004) used an approach that was similar to Pyke et al. (1975). For each site, they performed decoupled analyses of shear and volumetric strain. Shear strain was calculated using one-dimensional and two-dimensional ground response analyses, while volumetric strain was evaluated from shear strain using material-specific models derived from simple shear laboratory testing that incorporated important effects of fines content and as-compacted density and saturation. Figure 2.8 shows the material-specific model used to estimate vertical strains for Site B. These vertical strains were integrated over the height of the fill to estimate the total settlement from seismic compression. Figure 2.9 summarizes this process for a

cross section at Site B. The top plot in Figure 2.9 displays the shear strain profile from 2D ground response analyses while the bottom plot displays the estimated settlement obtained when the shear strain results are combined with the material-specific volumetric strain model from Figure 2.8. Overall, the computed settlements were in good agreement with the observed settlements at both Site A and Site B.

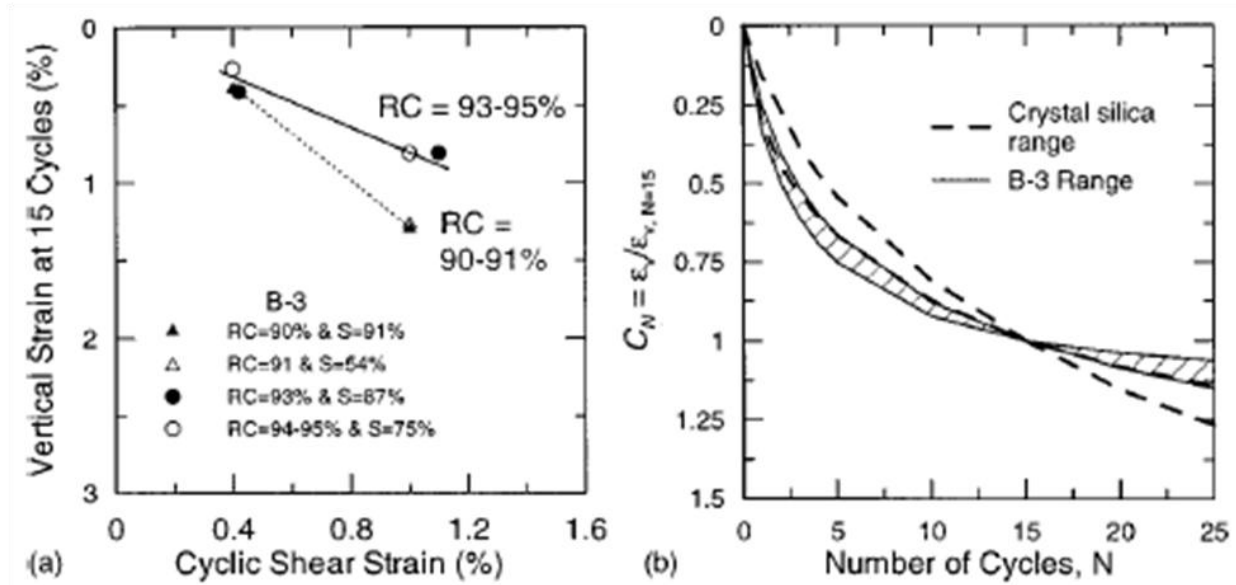


**Figure 2.8 (a) Seismic compression and (b) variation of normalized vertical strain with number of cycles of soil from Site B (Stewart et al. 2004).**

In the 2001  $M_w$  8.4 Southern Peru earthquake, many highway embankment sites were damaged due to seismic compression and these damaged areas were almost entirely underlain by fill materials. Wartman et al. (2003) describe these fills as consisting of gravelly, sandy, and silty soils with measured settlements of at least 10 cm for 2-4 m high embankments. The investigators noted that settlements were typically proportional to the height of the embankment and uniform across the road, with a sample schematic of observed ground deformations shown in Figure 2.10. Wartman et al. (2003) also observed seismic compression in a natural silty fine Aeolian sand overlaid by a highway road. Measured settlement was about 10-25 cm with lateral offsets of 5-10 cm. The investigators found that newer embankments performed better than older embankments and attributed it to improved compaction. Detailed back-analyses to evaluate the predictability of these deformations have not been completed.



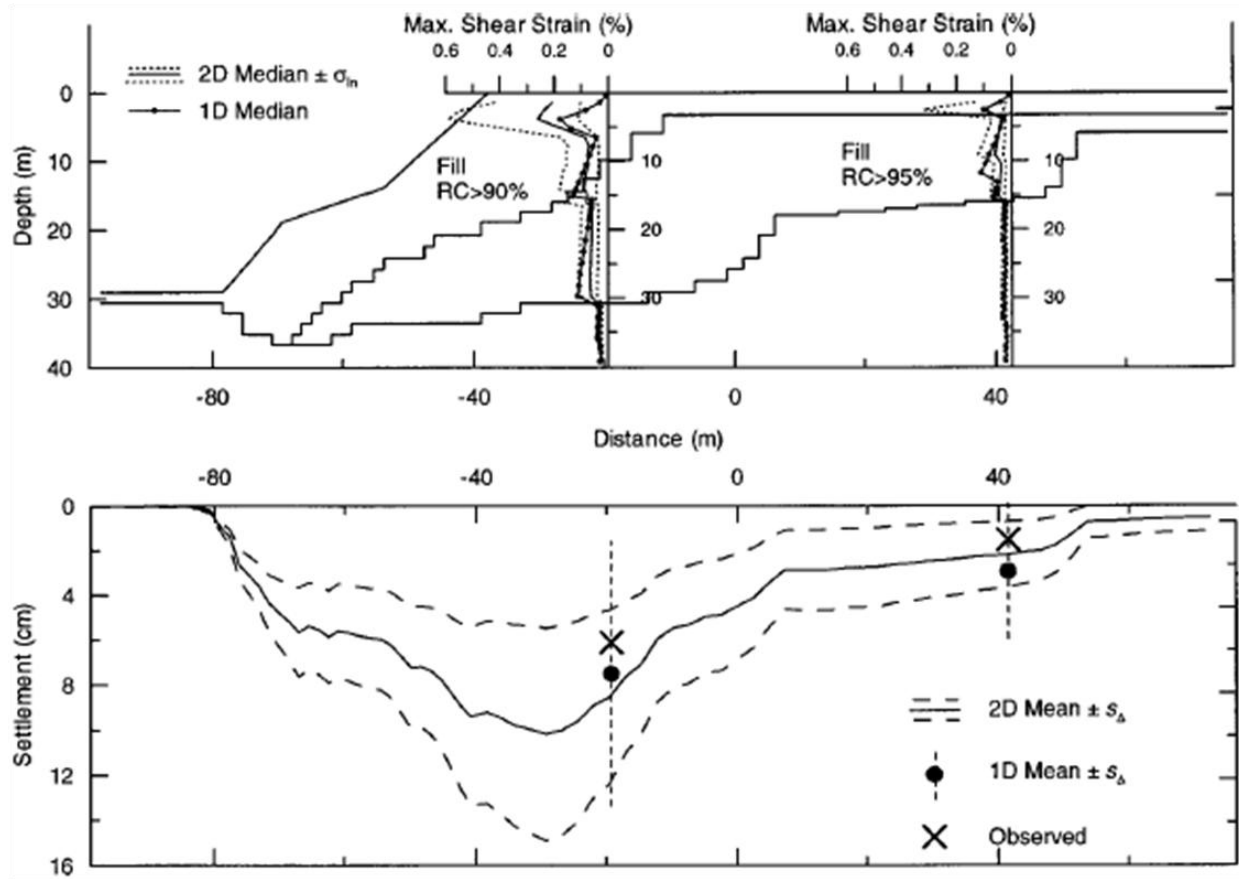


**Figure 2.9 Vertical profiles of shear strain from site response analyses (top frame) and lateral profiles of observed and calculated settlement (bottom frame) along a cross section for site B (Stewart et al. 2004).**

Wartman et al. (2005) also observed seismic compression induced damage at bridge embankments from the 2003  $M_w$  7.6 Colima earthquake. These embankments were typically 7 to 8 m high and were constructed of local sandy and silty soils compacted to 90 to 95% relative compaction, based on the modified Proctor standard. Earthquake induced settlements were uniform across the width of the roadway, with differential settlements of 4 to 10 cm at the bridge-embankment interface. They also found widespread ground failures in a neighborhood that was developed on top of uncontrolled fill consisting of sandy and gravelly soils. Portions of this neighborhood underlain by a shallow groundwater table typically liquefied while portions founded on unsaturated soils experienced seismic compression, manifested through ground cracking and settlements ranging from 5 to 20 cm. Additionally, several similarly backfilled mining pits also experienced seismic compression. These settlements were typically 15 to 30 cm,

with certain areas settling as much as 1.5 m. Detailed back-analyses to evaluate the predictability of these deformations have not been completed.

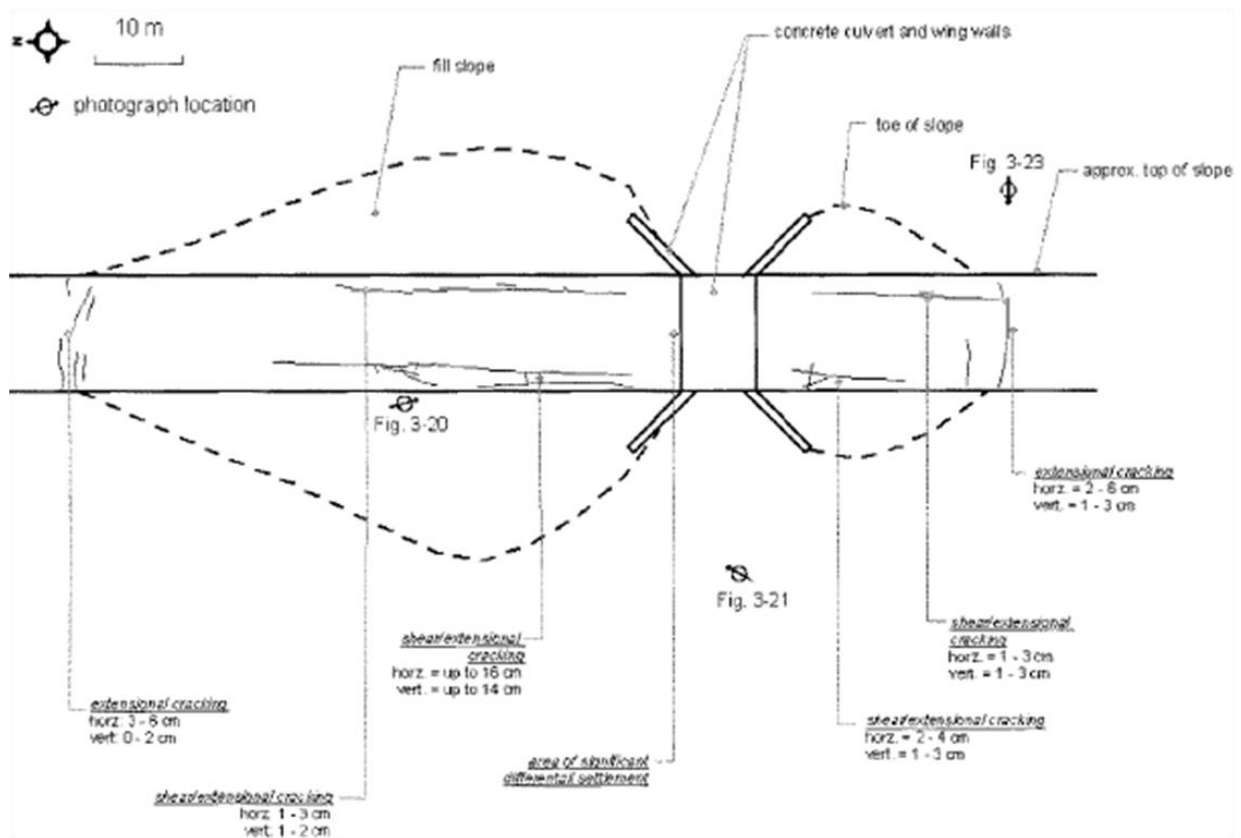


**Figure 2.10 Schematic of observed ground deformation at a highway embankment site (Wartman et al. 2003).**

### **3. Site Characterization**

We undertook a site exploration program for the Service Hall site at the Kashiwazaki-Kariwa Nuclear Power Plant site that included review of prior investigations, the drilling of a borehole including standard penetration testing with energy measurements, and suspension logging of seismic velocities. The results of this work are described in this chapter. Our field exploration work was performed in October 2009 under contract with Tokyo Soil Research.

#### **3.1 RESULTS OF GEOTECHNICAL EXPLORATION (CURRENT AND PRIOR STUDIES)**

The location of the borehole drilled at the SHA site is shown in the inset of Figure 1.2. The borehole was drilled using rotary wash procedures with a hole diameter of 116 mm for the upper 20 m and a hole diameter of 86 mm thereafter. The exploration reached a maximum depth of 120.4 m after 11 days of drilling. A relatively detailed boring log is provided in Appendix A (Electronic Supplement), which is summarized in Figure 1.3. The surface geology consists of the Holocene Arahama sand dune formation. This sand overlies the Pleistocene Banjin formation, the Pleistocene Yasuda formation, and the Pliocene Nishiyama formation. We also obtained selected results from previous geotechnical and geophysical site characterization that was conducted about 170 m from the Service Hall site (Tokyo Soil Research, 2009). Those data are generally consistent with the stratigraphy revealed by our exploration, as shown in Figure 1.3.

We sampled soil materials using an SPT sampler driven with an automatic trip-release safety hammer with mass 63.5 kg dropping 75 cm. The SPT sampler had an outer diameter of 51 mm and an inner diameter of 35 mm. Additional relatively undisturbed samples were obtained by pushing a triple-barrel pitcher sampler (similar to a Shelby tube) with an outer diameter of 76 mm and an inner diameter of approximately 74 mm. SPT samples were used for classification purposes only, whereas specimens from the pitcher sampler were used for dynamic testing as

described below. The boring logs from the previous investigation include blowcounts, but do not indicate the energy delivered. Average compression and shear wave velocities are also shown, but they appear to be at low resolution. Moreover, a limited number of shallow frozen samples have been collected in the vicinity of the SHA site.

For SPT sampling, we measured the percentage of the total theoretical energy delivered to the split-spoon sampler, or energy ratio, using procedures in ASTM D6066-98 and ASTM D1586 (see also Abou-Matar and Goble, 1997). The rods used in SPT sampling conformed with Japanese Industrial Standards (JIS), which are slightly different from AW rods (JIS rod outer diameter = 40.5 mm, inner diameter = 31 mm). The instrumented rod section used for energy measurement was AW, and couplers were machined to connect it to the JIS rods. Additionally, Japanese practice has the driller tap the first 10 cm of sampler penetration from the bottom of the borehole before the SPT is conducted. The SPT blowcount is then taken as the total number of blows to lower the rod 30 cm, in 10 cm intervals. Refusal was set at 60 blows. As shown in Figure 3.1, the energy ratios obtained in these tests range from 84 to 94% with an average of 87%. There does not appear to be a strong, systematic depth-dependence to the energy ratios. Energy-corrected blow counts were then calculated as:

$$N_{60} = N \times \frac{ER}{60} \quad (3.1)$$

Overburden corrections were then applied as:

$$N_{1-60} = N_{60} \times \left( \frac{p_a}{\sigma'_v} \right)^m \quad (3.2)$$

where  $m$  is a function of relative density per Boulanger (2003),  $p_a=101.3$  kPa, and  $\sigma'_v$  is the effective vertical stress at the sample depth (approximated as the total stress above the water table, which neglects matric suction). The resulting energy and overburden-corrected blow counts generally range from 15 to 30 in the sandy materials, as shown in Figure 1.3. No clean sand corrections are applied because fines contents are low (< 5%).

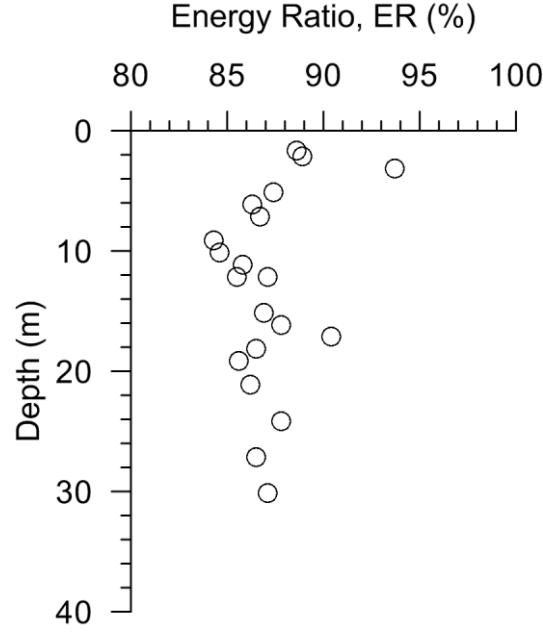


**Figure 3.1 Variation with depth of energy ratio in standard penetration tests.**

Relative densities ( $D_R$ ) can be estimated from the corrected blow count data as (Idriss and Boulanger, 2008):

$$D_R = \sqrt{\frac{N_{1\ 60}}{C_d}} \quad (3.3)$$

where  $C_d$  has been proposed as 44 by Tokimatsu and Yoshimi (1983); 55 to 65 for fine and coarse sands, respectively, by Skempton (1986); 26 and 51 for silty and clean sands, respectively, by Cubrinovski and Ishihara (1999); and 46 for generic clean sands by Idriss and Boulanger (2008). Given the low fines content and small mean grain size ( $D_{50}$ ) of the sandy soils (see following section for data), we estimate an applicable range of  $C_d$  of 40 to 60. This produces the relative densities shown in Figure 1.3, which generally range from about 50% to 80%.

Suspension logging was performed in our borehole to measure P and S wave velocities at 1 m intervals (Nigbor and Imai, 1994). Resulting interval velocities are shown in Figure 1.3. The results show the Holocene dune sand (0-16 m deep) to have  $V_s = 130$ -240 m/s. Underlying Pleistocene materials (16-70 m deep) have  $V_s = 240$ -390 m/s and the bedrock materials have velocities increasing from  $V_s = 330$ -450 m/s (70-83 m) to  $V_s = 400$ -600 m/s (> 83 m). The P-wave profile indicates a groundwater depth of about 45 m.

## **3.2 LABORATORY TESTING**

### **3.2.1 Index tests**

Soil materials recovered from the SPT split spoon sampler were combined to form bulk samples for index tests including grain size distribution, Atterberg Limits, and maximum and minimum unit weight. One bulk sample was prepared from sandy materials (from the Holocene and Pleistocene materials in the upper 70 m), whereas SPT samples from two relatively cohesive materials (Pleistocene mudstone from 70-83 m and Pliocene mudstone from 83-120 m) were kept in individual packages. Results of these index tests are given in Table 3.1. The Holocene and Pleistocene sands are classified as poorly graded sands (SP) using the unified soil classification system with a fines content of 4.1%. Mean grain size  $D_{50}$  is approximately 0.25 mm and coefficient of uniformity,  $C_u$  is approximately 2.55. The two cohesive Pleistocene samples had liquid limits of 65-69 and plasticity indices of 22-33. The cohesive Pliocene sample had a liquid limit of 69 and a plasticity index of 22. Maximum and minimum dry unit weights (and void ratios) were evaluated for the sand bulk sample using the Japanese method and dry tipping (ASTM D4253 and D4254, respectively).

### **3.2.2 Relative densities**

Triple-barrel pitcher samples were obtained at depths of 4, 8, 14 and 20 m. Dry unit weights and water contents were measured from these samples, from which void ratios could be computed using a specific gravity of  $G_s = 2.74$ . Results of these index tests are shown in Table 3.1. As shown in Figure 1.3, these results can be combined with the minimum and maximum densities from the bulk sample to evaluate relative densities, which are mostly near 40%. These  $D_R$  are smaller than those estimated from penetration resistance correlations. Additional  $D_R$  from shallow frozen samples obtained in a separate investigation elsewhere near the Service Hall site range from 20-50%, as shown in Figure 1.3.

### **3.2.3 Shear strength and modulus reduction and damping relations**

Soil specimens were carefully extracted from the sample tubes, trimmed, and re-consolidated for monotonic and cycle shear testing. Because the specimens are unsaturated, no B-value

measurements were made and volume change was allowed during shear. Soil specimens were found to have sufficient cementation/cohesion to maintain their integrity upon extraction.

Consolidated-drained triaxial compression tests were performed in the Tokyo Soil Research Laboratory after consolidating three specimens from each tube to isotropic stresses of 0.5, 1.0, and  $2.0 \times \sigma_v$ , where  $\sigma_v$  = in situ total stress. Table 3.1 summarizes the test results, which indicate drained friction angles of 36 to 39° (average of 37.6°) for the confining pressures considered. These results are comparable to estimates from  $\phi'$ -blow count correlations by Hatanaka and Uchida (1996), which are 35 to 41° for  $(N_1)_{60} = 15$  and 30, respectively.

**Table 3.1 Summary of soil index tests, triaxial compression shear strength tests, and resonant column-torsional shear tests for dynamic soil properties.**

Sample									Triaxial		RCTS	
Depth	$\sigma_c$	$\gamma_{dry}$	w	LL	PI	e	$e_{min}$	$e_{max}$	$\phi$	$G_{max}$	$D_{min}$	$\gamma_r$
(m)	(kPa)	(kN/m <sup>3</sup> )	(%)						(°)	(MPa)	(%)	(%)
4-5 <sup>P</sup>	81	14.95	19.9		NP	0.794			39.4	50	1.3	0.057
8-9 <sup>P</sup>	153	14.23	15.0		NP	0.886			36.4	74	0.9	0.1
14-15 <sup>P</sup>	256	14.42	23.3		NP	0.859			38.7	88	1.7	0.15
20-21 <sup>P</sup>	361	14.18	11.9		NP	0.899			35.9	112	0.8	0.163
Bulk (sand) <sup>S</sup>			16.6		NP		0.538	0.930				
75.15 <sup>S</sup>				69	33							
80.15 <sup>S</sup>				65	22							
90.15 <sup>S</sup>				69	22							

P – Pitcher sample

S – SPT samples

Using the same triple-barrel pitcher samples from the four sample depths, additional specimens were prepared for resonant column/torsional shear testing in the Tokyo Soil Research Laboratory. These specimens were isotropically consolidated to in situ stresses prior to cyclic testing. Each individual sample was subjected to a series of 10 cycles at 12-13 strain amplitudes. The small-strain shear modulus ( $G_{max}$ ) and material damping ( $D_{min}$ ) were taken from the resonant column tests per ASTM D4015. At each respective strain amplitude from the torsional shear tests, secant modulus ( $G$ ) and material damping ( $D$ ) were evaluated at the 5<sup>th</sup> and 10<sup>th</sup> cycle per

Japanese Standard JGS 0543-2000 (similar to ASTM D4015). We did not observe significant changes in  $G$  and  $D$  between cycles. Figure 3.2 plots the modulus reduction ( $G/G_{max}$ ) and damping curves for the 5<sup>th</sup> loading cycle. The pseudo reference strain from these tests,  $\gamma_r$ , which is the shear strain at which  $G/G_{max} = 0.5$ , is listed in Table 3.1.

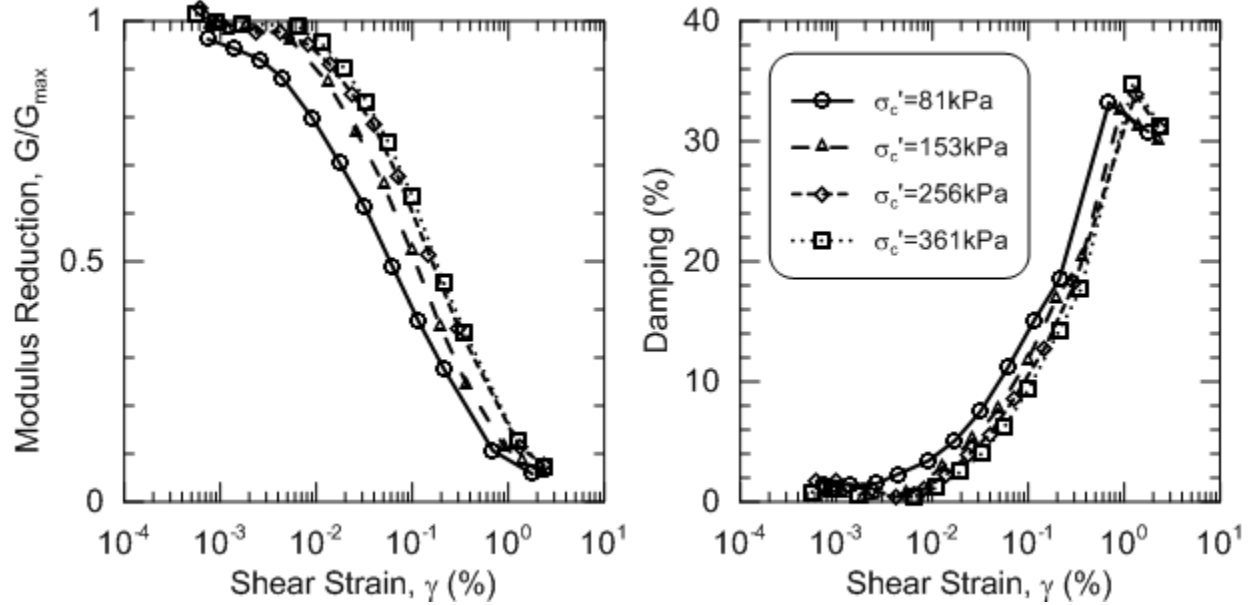


**Figure 3.2 Modulus reduction and damping curves from resonant column and torsional shear tests performed on specimens from four samples.**

### 3.2.4 Cyclic volume change

In order to estimate cyclic volume change of the Holocene and Pleistocene sand materials, reconstituted specimens were prepared from the bulk samples for cyclic simple shear testing at a range of strain amplitudes. While volume change also occurred during the torsional shear tests, they are not suitable for estimation of seismic compression because of the successively larger strain cycles applied to the specimens, which biases volumetric strains relative to what would occur in virgin loading for the same shear strain amplitude (e.g., Seed et al., 1977). While it would be preferable for the simple shear tests to be on intact specimens, we anticipate the results are suitable because fabric effects on dynamic soil properties have been found to be modest for strain-controlled testing (e.g. Dobry and Ladd, 1980; NRC, 1985; Polito and Martin, 2001).

Specimens for simple shear testing were prepared to field moisture contents (6 to 18%) and compacted via moist tamping to target relative densities near 35% and 65% to reflect the



possible range of in situ conditions as revealed by laboratory tests and SPT correlations. Other sample preparation procedures match those described by Duku et al. (2008). Specimens were confined laterally by a wire-reinforced Norwegian Geotechnical Institute (NGI) membrane with a diameter of 102 mm. Specimens were consolidated under vertical stresses of  $\sigma_v = 50, 100, 200$  or 400 kPa and then sheared under constant displacement amplitudes (corresponding to shear strains between 0.01 to 1%) at a frequency of 1 Hz using the digitally controlled simple shear device described by Duku et al. (2007). Figure 3.3a and Figure 3.3c summarize the vertical strain at 15 cycles  $[(\varepsilon_v)_{N=15}]$  from these tests and show no apparent influence of water content. Power law fits to the data were established as (Duku et al., 2008):

$$(\varepsilon_v)_{N=15} = a (\gamma - \gamma_{tv})^b \quad (3.4)$$

where  $a$  and  $b$  are regression coefficients listed in Table 3.2 and  $\gamma_{tv}$  is the volumetric threshold shear strain estimated from test data using the method by Yee et al. (2011).

Parameter  $b$  can be thought of as the slope of the best fit line through test data in log-log space, while parameter  $a$  can be thought of as the vertical strain at about 1% shear strain. Figure 3.4 illustrates the effect of relative density on parameter  $a$  with slope parameter  $b$  fixed to 1.2. The value of  $b = 1.2$  is an average obtained from prior testing of 16 clean sands (Duku et al., 2008) and represents reasonably well the SHA data as well. As shown in Figure 3.4, the SHA data are consistent with a  $D_R$ - $a$  model for clean sands by Duku et al. (2008).

Eq. (3.4) represents the vertical strains from seismic compression at a total stress overburden pressure of  $\sigma_v = 100$  kPa. For other overburden pressures, a correction factor  $K_{\sigma,\varepsilon}$  can be applied to parameter  $a$ , which has been found in previous work to be reasonably represented as (Duku et al., 2008):

$$K_{\sigma,\varepsilon} = \left( \frac{p_a}{\sigma_v} \right)^{0.29} \quad (3.5)$$

Parameter  $K_{\sigma,\varepsilon}$  represents of the ratio of  $a$  for arbitrary  $\sigma_v$  to  $a$  at  $\sigma_v = 100$  kPa. Figure 3.3e shows that test results for the SHA soils fit this overburden model well.

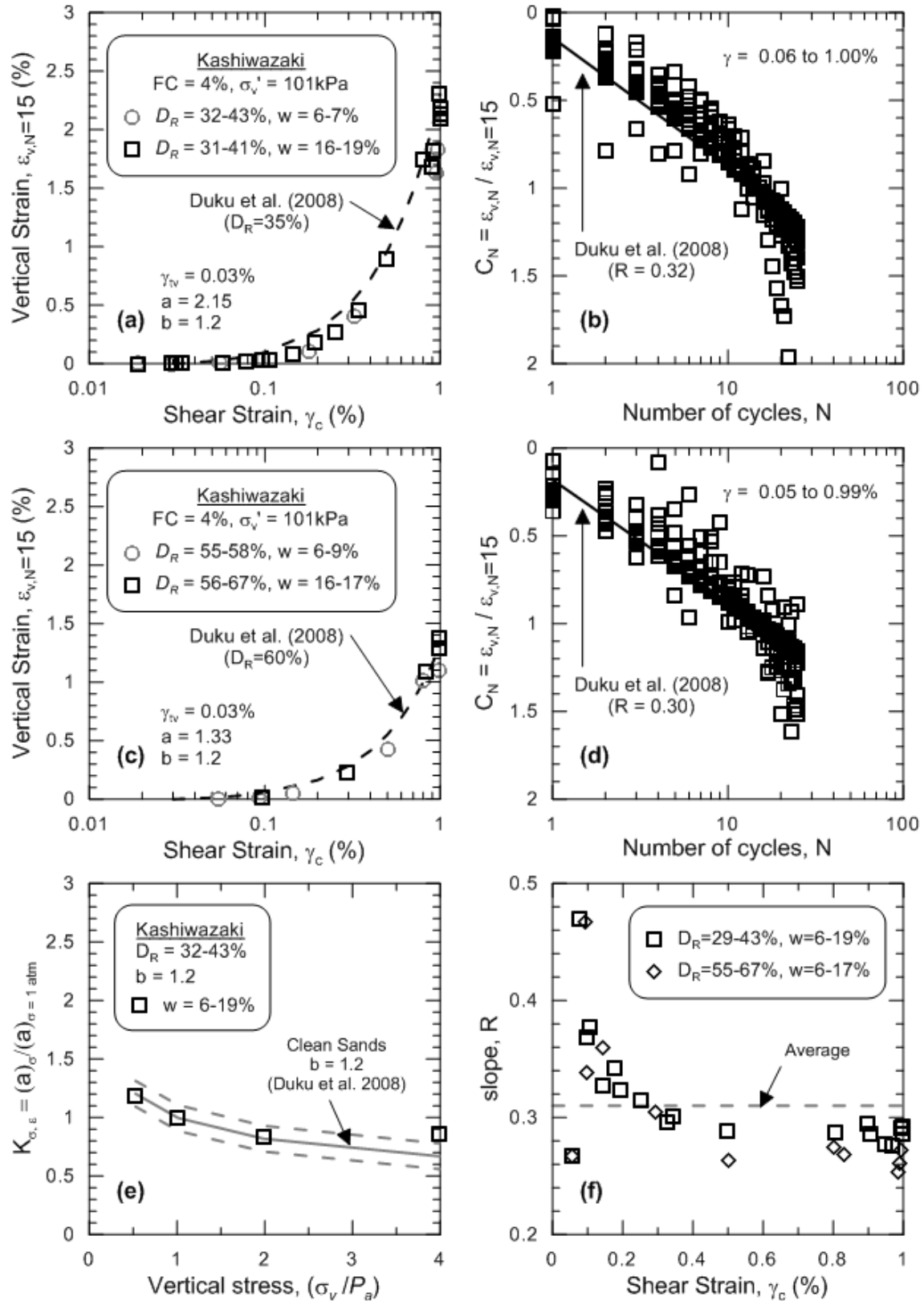


**Figure 3.3 Results of simple shear tests showing cyclic volume change characteristics of sandy materials in upper 70 m of SHA site.**

**Table 3.2 Suites of cyclic simple shear tests and regressed parameters.**

$D_R$	w	$\sigma_v$	a	b	$\gamma_{tv}$	$a^{**}$
(%)	(%)	(kPa)			(%)	
32-43	6-7	100	1.91	1.34	0.03	1.88
28-42	17-18	50	2.50	1.11	0.038	2.56
31-41	17-19	100	2.27	1.33	0.034	2.23
33-43	17-18	200	1.86	1.42	0.03*	1.79
31-41	17-18	400	1.95	1.54	0.044	1.86
55-58	6-9	100	1.24	1.28	0.03*	1.22
56-67	16-17	100	1.42	1.33	0.03*	1.40
62-62	17-18	400	0.82	1.39	0.05*	0.63

\* assumed values due to lack of data for  $\gamma_{tv}$

\*\* b fixed at 1.2

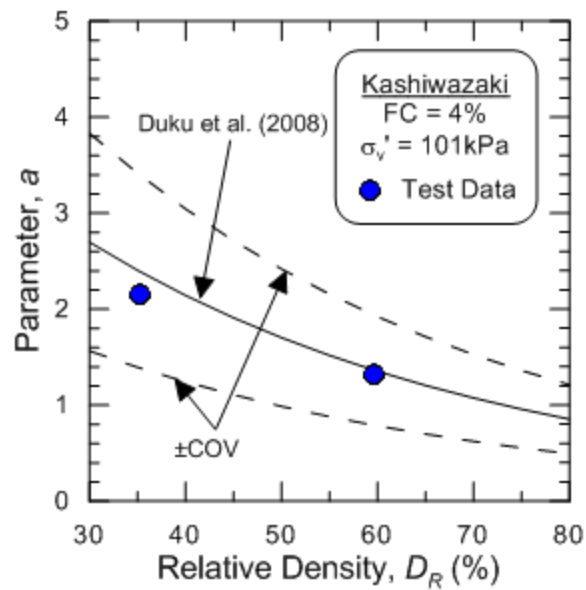


**Figure 3.4 Comparison of parameter  $a$  for KKNPP sand with slope parameter  $b = 1.2$  against the clean sand model by Duku et al. (2008).**

Duku et al. (2008) also provided a relationship to describe the effect of the number of loading cycles, given as:

$$C_N = R \ln N + c \quad (3.6)$$

where  $C_N = (\varepsilon_v)_N / (\varepsilon_v)_{N=15}$ ,  $R$  = regressed slope parameter,  $N$  = number of loading cycles, and  $c = 1 - [\ln(15)R]$ . Data for  $C_N$  and  $R$  is shown in Figure 3.3b, d, and f, giving an average value around 0.31, which is close to the average value of 0.29 obtained by Duku et al. (2008).

Eq. (3.4) and its modifiers (Eqs. 3.5 and 3.6) apply for ground shaking in a single horizontal direction. We examined the degree to which multi-directional shaking affects seismic compression behavior through a series of 1-D and 2-D simple shear tests. As shown in Figure 3.5, sample shear strain histories computed from preliminary ground response analyses at about 8 m depth for orthogonal fault normal (FN) and fault parallel (FP) directions were imparted to three similarly prepared soil specimens under three conditions: (1) both FN and FP applied together in a 2-D test; (2) FN only applied in a 1-D test; (3) FP only applied in a 1-D test. The vertical strain histories resulting from this sequence of three tests are shown in Figure 3.5 and indicate that the cumulative vertical strain from multi-direction shaking is practically identical to summation of vertical strains evaluated independently in the two 1-D tests. These results support the findings of Pyke et al. (1975), described previously in Section 2.2.

The results of these tests, as parameterized above, comprise a material-specific volumetric strain material model (VSMM) for the dune sand materials at the SHA site conditional on a relative density of about 35% and 65%. This VSMM will be used subsequently for estimation of settlement from seismic compression.

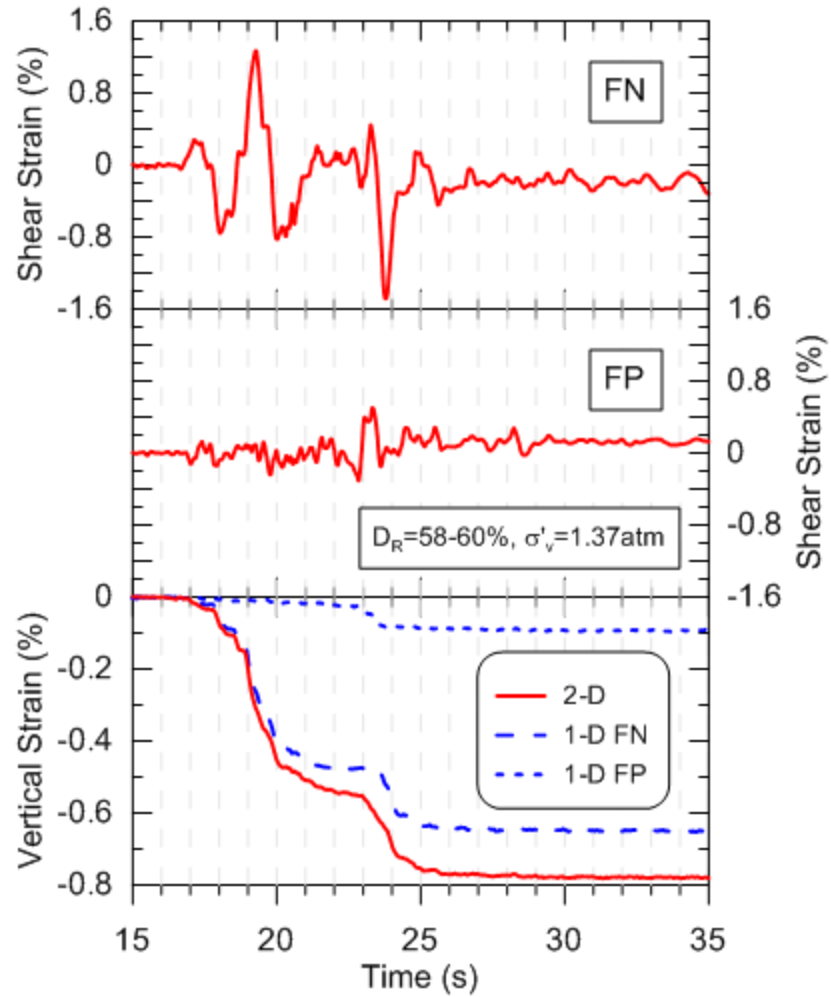


**Figure 3.5 Simple shear results from applying ground motions at 8.2 m depth taken from site response analyses and the resultant settlement time history. FN and FP ground motions were also applied separately.**

## 4. Ground Motion Data from Service Hall Array

Accelerometers at the KKNPP are owned and maintained by the Tokyo Electric Power Company (TEPCO). The horizontal accelerometers have azimuths of  $18.9^\circ$  and  $108.9^\circ$  (measured east from due north to reflect the power plant's orientation). These data have not been publically released but were made available to the third author and approved for use in the present work. These data include acceleration recordings for the main shock and two subsequent aftershocks, named L and S herein, with their epicentral and hypocentral information listed in Table 4.1. The SHA accelerometer data provided by TEPCO was in digital form and had engineering units, but was otherwise unprocessed. The unprocessed data has baseline drift, which necessitated corrections to remove low frequency noise. We employed the data processing procedures described by Boore (2005) and Boore and Bommer (2005):

- Zero pads are added to the beginning and end of each record. The number of zeros added is equal to  $1.5n/(f_c * dt)$  where  $n$  = butterworth filter order (integer),  $f_c$  = filter corner frequency, and  $dt$  = sampling interval (0.01s).
- An acausal high-pass filter is applied at a specified corner frequency. The frequency is selected on a record-by-record basis so as to remove baseline drift while minimally affecting the amplitudes of velocity and displacement histories. These frequencies ranged from 0.03 to 0.10 Hz. We utilized a high pass acausal butterworth filter of order 4 as implemented in Matlab. These frequencies are presented in Table 4.2.
- The filtered acceleration history is integrated to velocity and displacements using the full duration of the time series.

Acceleration, velocity, and displacement histories are shown in Appendices B, C, and D, for the main shock and two subsequent aftershocks, L and S respectively (Electronic Supplement). The same filter frequencies as presented in Table 4.2 were also used for the subsequent aftershocks. Summary velocity histories are shown for the main shock in Figure 4.1

after rotation into the fault strike normal (FN) and parallel (FP) directions. Resultant peak ground accelerations (PGA) and peak ground velocities (PGV) are also shown in Table 4.3 for each seismic event. Figure 4.2 shows the main shock 5% damped pseudo acceleration response spectra at each instrument in the FN, FP and vertical directions. For each component, the spectra are similar at depths of 99.4 and 250 m (both in bedrock). As the motions travel upwards through the soil column, low period ( $T < \sim 0.6$  sec) horizontal components are reduced and longer period horizontal components are progressively amplified as shown in the spectra at 50.8 and 2.4 m. Comparing the FN and FP response spectra, we see larger accelerations in the FN direction, particularly in bedrock motions at 0.1-0.2 sec and near 2.0 sec in bedrock and surface motions. The FN amplification near 2.0 sec period could be a forward directivity pulse period, because it lies in the range of previously observed pulse periods for shallow crustal earthquakes ( $\sim 1.3$ - 4.0 sec, with median of 2.2 sec; Shahi and Baker, 2011).

**Table 4.1 Ground motions used for this study.**

Event	Magnitude			Distance				
	$M_w$	Latitude	Longitude	Depth	$R_{rup}$	$R_{jb}$	$R_{epi}$	$R_{hyp}$
				(km)	(km)	(km)	(km)	(km)
Main shock	6.6	37.53	138.45	9	16	0		
Aftershock L	5.7	37.50	138.47	15			15	21
Aftershock S	4.4	37.51	138.63	20			9	22

**Table 4.2 Filter frequencies applied to vertical array data.**

Array Sensor Depth	Filter corner frequency		
	EW	NS	UD
(m)	(Hz)	(Hz)	(Hz)
2.4	0.05	0.10	0.10
50.8	0.03	0.05	0.10
99.4	0.03	0.05	0.05
250	0.03	0.10	0.05

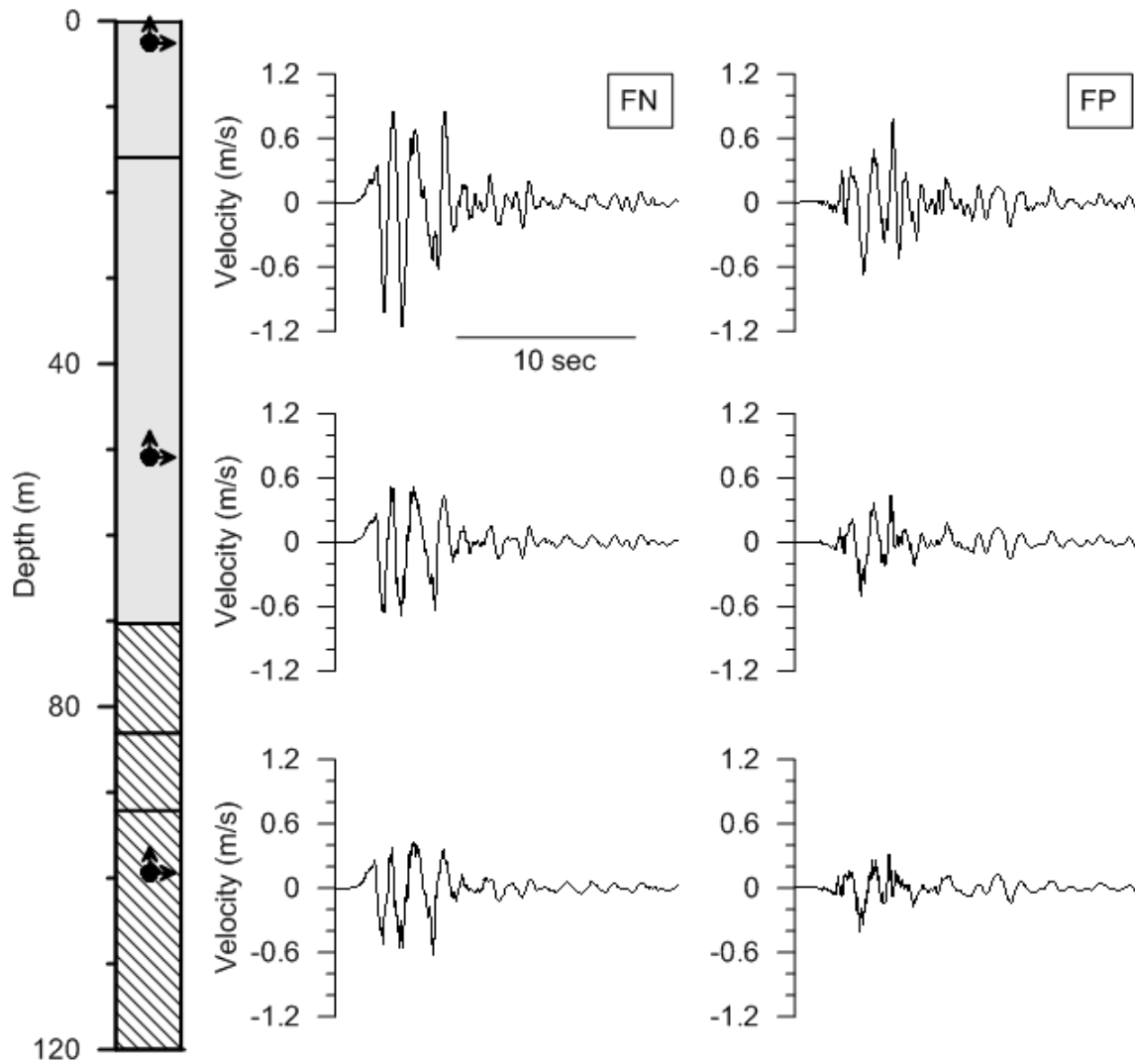


**Figure 4.1 Main shock velocity histories from the upper three instruments at the SHA site rotated into the fault normal (FN) and fault parallel (FP) directions.**

**Table 4.3 PGA and PGV from rotated motions.**

Event	FN		FP		UD	
	PGA	PGV	PGA	PGV	PGA	PGV
	(g)	(cm/s)	(g)	(cm/s)	(g)	(cm/s)
Main shock	0.42	116	0.38	79	0.6	44
Aftershock L	0.18	24	0.17	10	0.2	9
Aftershock S	0.04	1	0.04	1	0.04	1



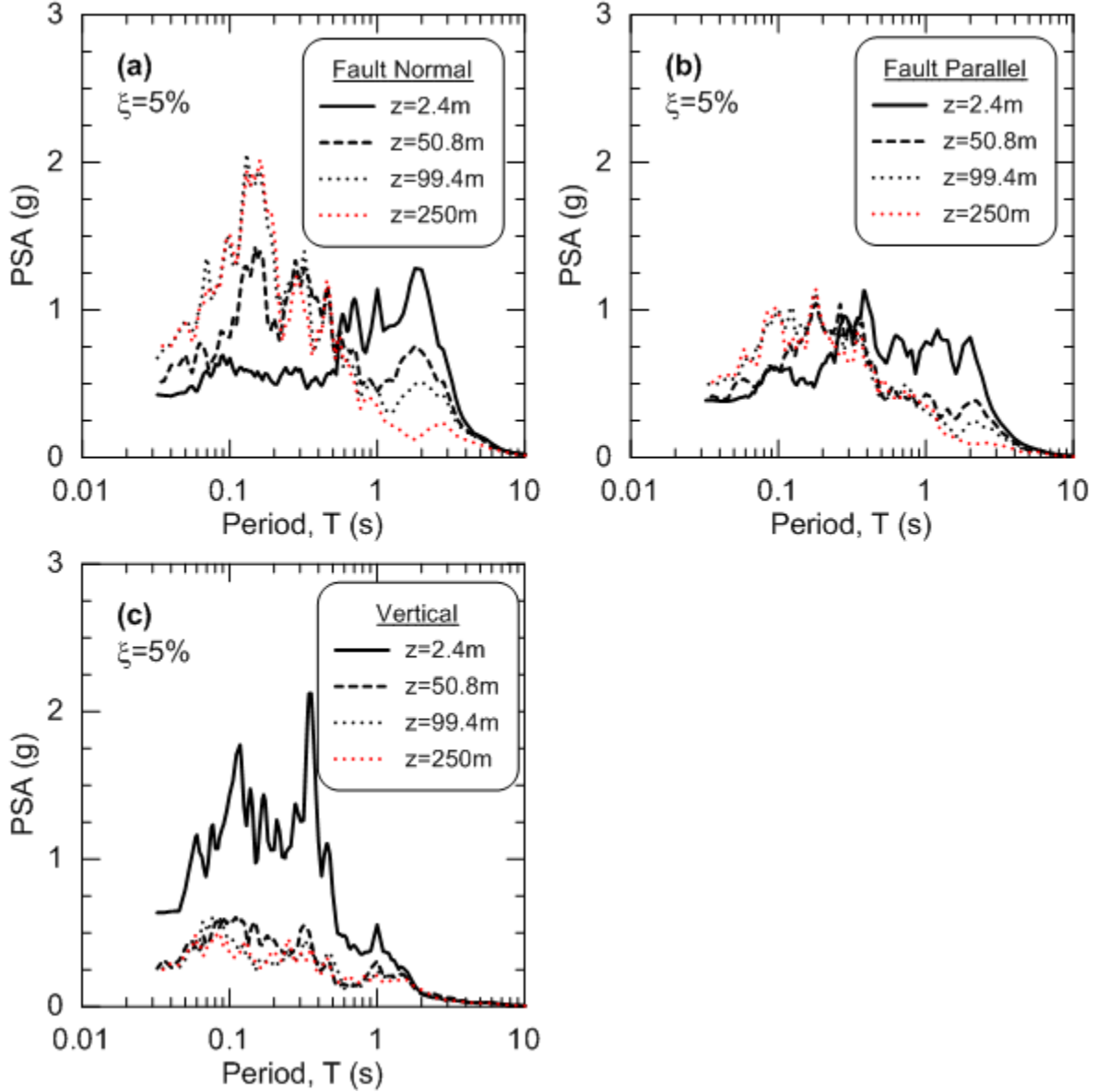


**Figure 4.2 Pseudo acceleration response spectra for the three components of recorded main shock ground motions at SHA site.**

In Figure 4.2c, the vertical spectra are relatively consistent at 50.8, 99.4, and 250 m, but significant amplification occurs across all periods near the surface. The vertical bedrock response spectra are lower than either of the horizontal bedrock response spectra at all periods. Near the surface, the vertical spectra for  $T < 0.4$  sec exceed the horizontal spectra, which are typical of near-fault recordings (Bozorgnia and Campbell, 2004).

Figure 4.3 shows surface-to-rock (SR) transfer functions of horizontal components of the ground motions from 2.4 m and 99.4 m depth as well as horizontal-to-vertical (H/V) spectral

ratios of the surface (2.4 m) recordings. Transfer functions were computed from power spectral density functions and time-domain smoothing procedures with an effective bandwidth of 0.195 Hz using procedures described by Mikami et al. (2008). The SR transfer functions exhibit relatively similar shapes for the three events. The lowest frequency peak (indicating the first-mode site frequency) is consistently lower in the FN direction relative to the FP direction, which may be due to complexities in the geologic structure. In the FN direction, the fundamental mode frequency ranges from about 0.75 Hz for the main shock to 0.8-1.0 Hz for the aftershocks. In the FP direction, this frequency is approximately 1.0 Hz and there is less change between events. The H/V spectral ratios are also relatively consistent between events and suggest similar site periods as the SR transfer functions. The general similarity of the SR transfer functions and H/V spectral ratios from event-to-event indicates relatively consistent site response, aside from the effects of nonlinearity on the site period in the FN direction.

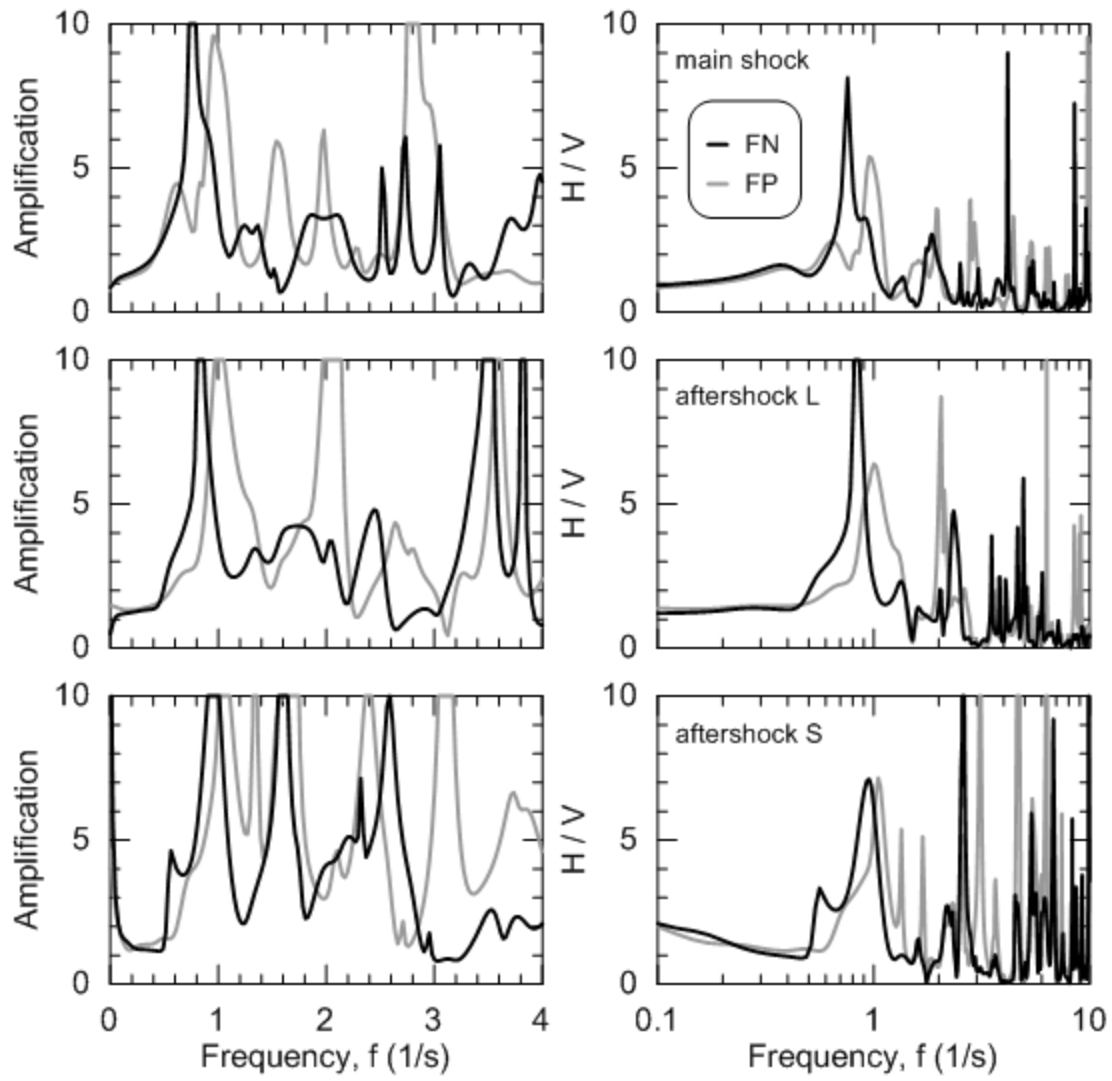


**Figure 4.3** Surface-to-rock (2.4 m / 99.4 m) transfer functions and surface (2.4 m) H/V spectral ratios for main shock and aftershock recordings

## 5. Ground Response Analysis

Ground response analyses are used to predict one-dimensional shear wave propagation through the soil column at the SHA site. These analyses are performed using an equivalent linear (EQL) method in which the wave equation is solved in the frequency domain (e.g., Kramer, 1996) and a nonlinear (NL) method in which the soil column is represented as a multiple degree of freedom system whose response to a base input motion is solved in the time domain using numerical integration. For SHA, the input motion is taken as the corrected ground motion recording within bedrock at 99.4 m depth. As recommended by Kwok et al. (2007), the recorded motions are used as recorded (“within” condition) with a rigid base assumed below 99.4 m. Subsequent sections describe the soil properties used for these analyses (small strain modulus and nonlinear modulus and damping relations). Both one dimensional EQL and NL ground response analysis are performed in DeepSoil 4.0 (Hashash et al., 2011). The desired outcomes of the analyses are (1) predicted ground motions through the soil column for comparison to recordings and (2) profiles of predicted shear strains for use in seismic compression analysis.

### 5.1 DYNAMIC SOIL PROPERTIES FOR ANALYSIS

The initial shear wave velocity profile used for analysis is smoothed relative to the interval velocities from suspension logging as shown in Figure 1.3. At a depth of about 50 m, just below the water table, there is a slight dip in the velocity profile that impacts the analysis results. Surrounding materials have shear wave velocities above 300 m/s, whereas at 50 m, shear wave velocities are about 270 m/s. Mass densities are taken from measured moist unit weights, which were approximately  $16 \text{ kN/m}^3$  to a depth of 4 m and  $17.75 \text{ kN/m}^3$  from 4 to 45 m. A saturated unit weight of  $20.8 \text{ kN/m}^3$  was used from 45 to 70 m. Maximum shear modulus is computed from shear wave velocity and mass density as:

$$G_{\max} = V_s^2 \rho \quad (5.1)$$

The NL constitutive models in DeepSoil utilize a hyperbolic backbone curve described by:

$$\tau = \frac{G_{\max} \gamma}{1 + \beta \left( \frac{\gamma}{\gamma_r} \right)^\alpha} \quad (5.2a)$$

where  $\gamma$  is shear strain,  $\gamma_r$  is pseudo-reference strain, and  $\beta$  and  $\alpha$  are fitting coefficients generally taken as  $\beta = 1.0$  and  $\alpha \sim 0.92$  (Darendeli, 2001; Zhang et al., 2005). The representation of the backbone curve as shown in Eq. (5.2a) is equivalent to taking the modulus reduction curve as:

$$\frac{G}{G_{\max}} = \frac{1}{1 + \beta \left( \frac{\gamma}{\gamma_r} \right)^\alpha} \quad (5.2b)$$

We adopt this hyperbolic model for the backbone curve with  $\beta = 1.0$ . Values for parameter  $\alpha$  are adjusted to fit the curvature of the laboratory modulus reduction curves, as described further below. With this framework, the only required parameters for a given depth in the soil column are  $G_{\max}$  and pseudo-reference strain  $\gamma_r$ . Parameter  $\gamma_r$  can be evaluated from cyclic test data (or empirical models calibrated from test data), which describe the backbone curve at small strains ( $\gamma < \sim 0.5-1.0\%$ ). However, the hyperbolic model breaks down at large strains, where it typically produces stress estimates biased relative to the shear strength. In this section, we make first-order estimates of  $\gamma_r$  using available test data and models, which can be used for preliminary ground response analyses. Problematic depth intervals for which large strains develop are then identified in a subsequent section.

The RCTS test data described above provides measurements of  $\gamma_r$  at the sample depths of 4, 8, 14, and 20 m, with the results in Table 3.1. **Error! Reference source not found.** shows the pseudo-reference strains from RCTS tests performed in this study and for the neighboring site compared with predictions from empirical models by Menq (2003) and Darendeli (2001). The Darendeli (2001) model was developed from a large database taking into account both plastic and non-plastic soil materials, while the Menq (2003) model was derived specifically for

granular soil materials. The Menq (2003) model is considered more directly applicable to the granular materials present in the upper 70 m of the SHA site.

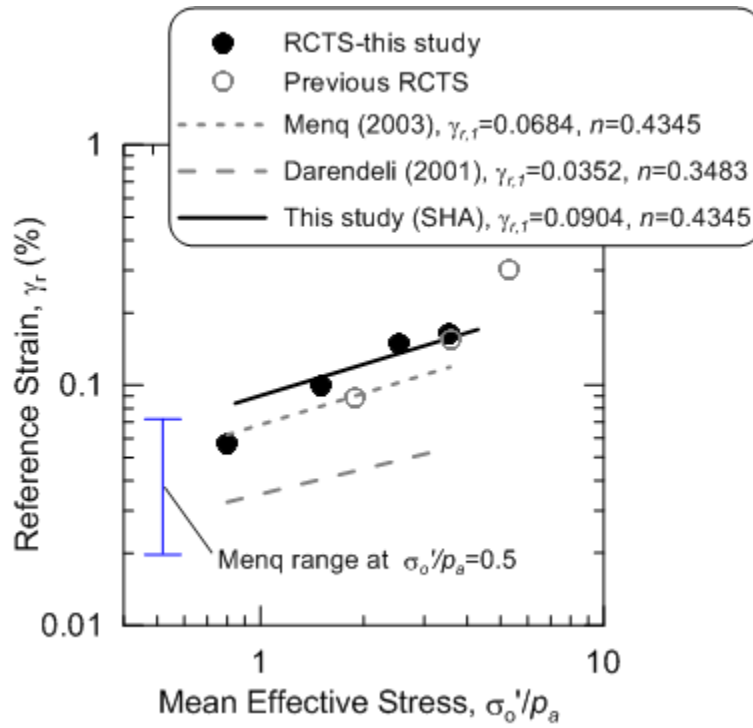


**Figure 5.1 Variation of pseudo reference strain with mean confining pressure from RCTS tests (this study), previous RCTS tests (neighboring site), and model predictions.**

**Error! Reference source not found.** shows that  $\gamma_r$  from the RCTS tests to generally be higher than the Menq (2003) and Darendeli (2001) model predictions. The variability of data around the Menq model has not been formally evaluated, but an approximate range of data at an overburden pressure of 0.5 atm is shown in **Error! Reference source not found.** (F-Y Menq, *personal communication*, 2010). Based on this preliminary result, it appears that test results from the SHA site lie near the upper range of the data considered by Menq (2003). One possible reason for the difference is that the Menq (2003) testing involved dry sands without matric suction, whereas our RCTS tests are partially saturated; the resulting matric suction may increase the effective confinement relative to what is reported based on the isotropic cell pressure in the device. A power fit to the tube sample pseudo-reference strains was derived according to:

$$\gamma_r = \gamma_{r,1} \left( \frac{\sigma'_0}{p_a} \right)^n \quad (5.3)$$

where  $\sigma'_0$  = mean effective confining pressure (same as cell pressure in RCTS tests),  $p_a$  = atmospheric pressure (101.3 kPa),  $n$  is taken from Menq (2003) as 0.4345, and  $\gamma_{r,1}$  is a regression coefficient [0.0904±0.0565 for present work (range indicates 95% confidence interval); 0.0684 for sands, Menq, 2003; 0.0352 for sands, Darendeli, 2001]. The resultant fits are shown in **Error! Reference source not found..**

Eq. (5.4) was used to estimate pseudo-reference strains through most of the sand column above the water table, as shown in **Error! Reference source not found..** Below the ground water table, where test data is not available and matric suction is zero, we anticipate that the Menq (2003) model is more accurate than the projection from Eq. (5.4). Accordingly, we transition the  $\gamma_r$  used for analysis from the projected value at the deepest sample (20 m) to the Menq estimate at the base of the sand column (70 m). To estimate the  $\alpha$  parameter in Eq. (5.2), pseudo-reference strains from **Error! Reference source not found.** at depths of 4.5, 8.5, 14.5, and 20.5 m were entered into Eq. (5.2b), and  $\alpha$  was adjusted so that the predicted modulus reduction curves match the curvature from laboratory tests. The resulting  $\alpha$  values were found to vary with overburden pressure as:

$$\alpha = \alpha_1 + \alpha_2 \log \left( \frac{\sigma'_0}{p_a} \right) \quad (5.4)$$

where  $\alpha_1 = 0.82 \pm 0.10$  and  $\alpha_2 = 0.34 \pm 0.27$ . Our model for  $\alpha$  scales more strongly with  $\sigma'_0$  than the  $\alpha$  equation provided by Menq (2003) ( $\alpha_1 = 0.86$  and  $\alpha_2 = 0.1$ ), which is reported to be poorly constrained (Menq, 2010, *pers. communication*). While our model for  $\alpha$  captures the trends with depth in modulus reduction behavior,  $\alpha$  also affects damping, so we alternatively could have used an  $\alpha$  model that captures damping. The model provided by Eq. (5.4) and our coefficients is generally well-behaved for damping at strains < 0.3%, but is judged to be unrealistic for strains > 1.0% because damping at large strain is increasing with depth. Menq's  $\alpha$  model provides a more realistic trend to the damping curves (decreases with depth over wider strain range), but at the expense of modulus reduction misfit. We chose to minimize modulus reduction misfit through

the use of Eq. (5.4) with our  $\alpha$  coefficients, which is checked subsequently to see if damping trends are problematic for the strain range of interest.

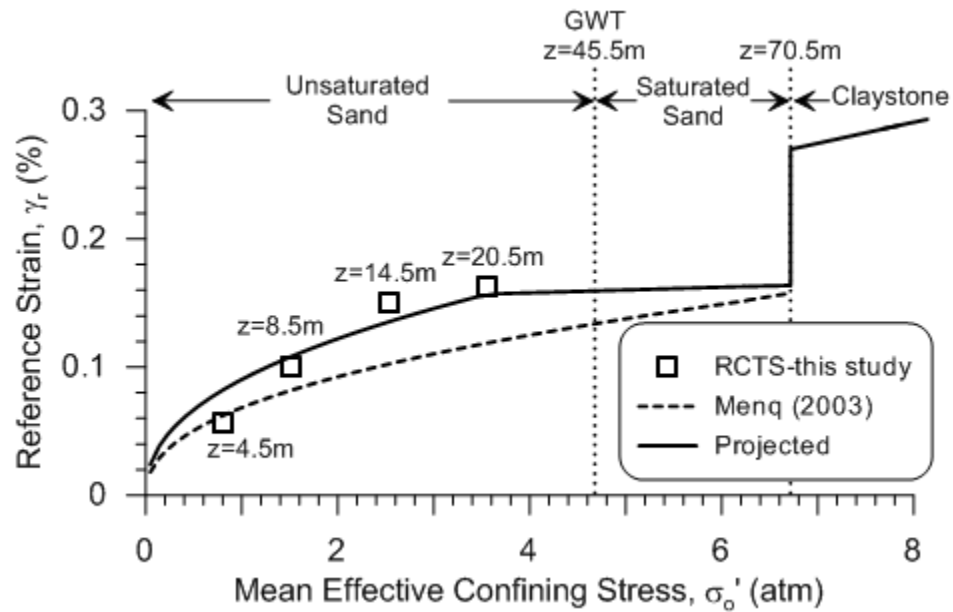


**Figure 5.2 Values of pseudo reference strain used for analysis as function of with confining pressure and depth through the soil column.**

Figure 5.3a compares the aforementioned model to RCTS test data for the sample at 20 m. Also included are the modulus reduction curves from the Darendeli (2001) and Menq (2003) models.



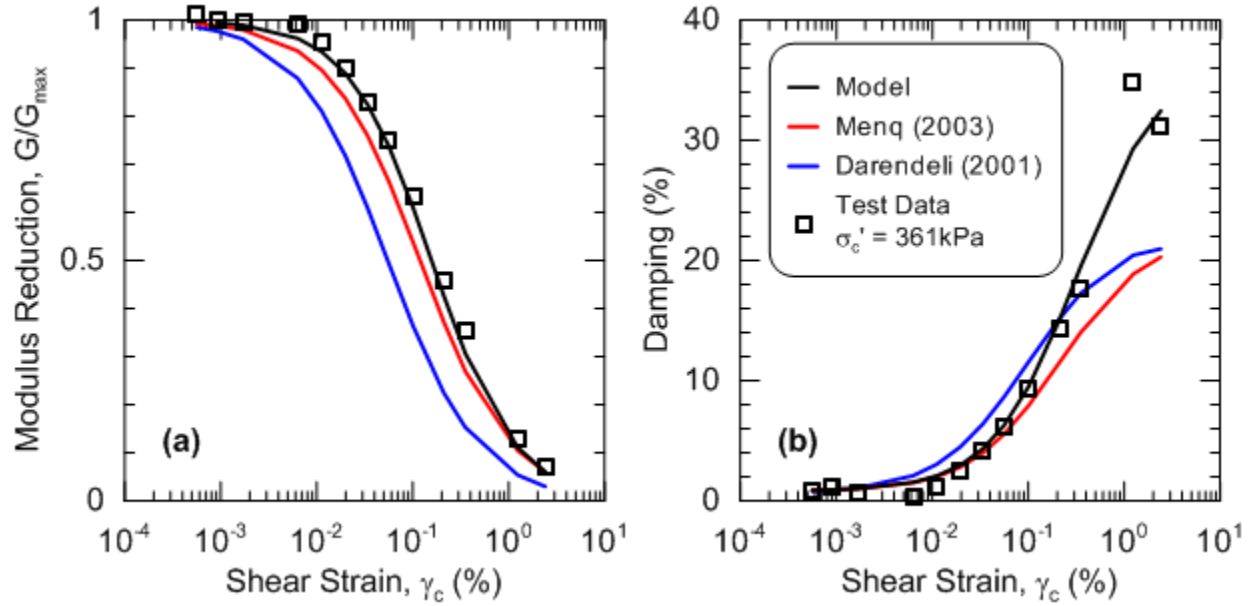


**Figure 5.3 Comparison of the Darendeli (2001) and Menq (2003) (a) modulus reduction and (b) damping curve models to sample test data from 20 m deep. Resultant modulus reduction and damping curves are labeled as “Model”.**

Figure 5.3b shows that RCTS damping data for the 20 m depth sample exceeds Darendeli (2001) and Menq (2003) model predictions at large strains. As shown in Figure 5.4, the damping models are good for  $D_{min}$ , so the misfit is associated with the component of the material damping model above the minimum value (i.e.,  $D - D_{min}$ ). In the Darendeli (2001) and Menq (2003) models, the model for  $D - D_{min}$  depends on the shape of the modulus reduction curve (as required by Masing's rules). The Darendeli (2001) and Menq (2003) model predictions in Figure 5.3b use their respective modulus reduction curves. For application at the SHA site, we utilize the  $D - D_{min}$  component of the Menq's (2003) model with two modifications (1) use the modulus reduction curves from this study in the  $D - D_{min}$  equations and (2) increase the  $D$  above  $D_{min}$  by 40% to achieve a reasonable match to the data at 20m (as shown in Figure 5.3b) and other depths as well.

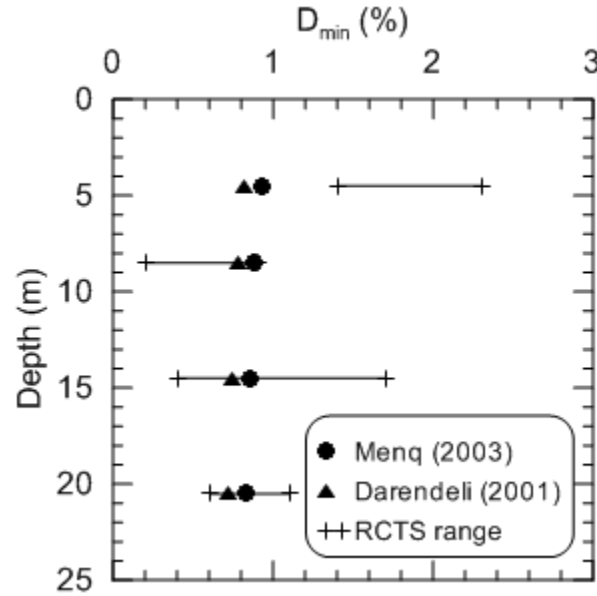


**Figure 5.4 Comparison of Menq (2003) minimum damping and the range of damping values at shear strains less than 0.05% from RCTS testing.**

To generate modulus reduction and damping curves for the relatively plastic soil and rock materials, two modifications were applied to the Menq (2003) model. The term that considers plasticity was taken from the Darendeli (2001) pseudo-reference strain and minimum damping models and added into the aforementioned granular model. Additionally, parameter  $\alpha$  was set to 0.92 as in the Darendeli (2001) model. These modifications were used to generate pseudo-reference strains and minimum damping for modulus reduction and damping curves for the relatively plastic materials below 70 m depth. The resulting pseudo-reference strains for plastic materials below 70 m depth are shown in **Error! Reference source not found..**

## 5.2 GROUND RESPONSE ANALYSIS USING AFTERSHOCK DATA

This section describes the results of initial ground response analyses utilizing the smoothed version of the suspension logging data as shown in Figure 1.3 and modulus reduction/damping relations derived from RCTS laboratory testing, as described in Section 5.1. It will be shown that problems were encountered in these analyses and final runs were performed using strength adjustments to the modulus reduction curves and increases to small strain damping  $D_{min}$ . Those adjustments and their effect on the results are described in Sections 5.4.1-5.4.3.

Both EQL and NL ground response analysis in DeepSoil 4.0 requires sub-layering that addresses: (1) stratigraphic boundaries and changes in the  $V_s$  profile; (2) depths of accelerometers, such that output depths are comparable; and (3) minimum layer thicknesses that allow waves with maximum frequencies between 25-50 Hz to propagate without artificial damping [see Kwok et al. (2007) and Hashash et al. (2011) for details]. Each sub-layer of the SHA profile was assigned modulus reduction and damping curves, taken from the pseudo reference strain and damping formulations described above. Following the recommendations of Kwok et al. (2007) for input motion selection for vertical arrays, the FN and FP ground motions from the accelerometer at 99.4 m were taken as input with a rigid base. For EQL analysis, the effective shear strains for soil property iteration were taken as 56, 47, and 34% of the peak strain for the main shock, aftershock L, and aftershock S respectively, which are consistent with the recommendations of Idriss and Sun (1992).

We begin our analysis using the aftershock data to gain insight into the degree to which 1D analysis can capture the site response without the complications of highly nonlinear soil behavior. As noted previously in Table 4.1, the two aftershocks are labeled L and S. Figure 5.5-5.7 present accelerograms and response spectra (data and simulation results), strain profiles, and maximum horizontal acceleration (MHA) profiles, respectively for aftershock L. Figure 5.8-5.10 present similar results for Aftershock S. Figure 5.11 shows predicted and observed SR transfer functions for the aftershocks. We note that the predicted transfer function provides a reasonable match to the shape and resonant frequencies of the observed transfer functions, although the data is clearly too limited to establish statistically significant empirical trends for small-strain site response. Nonetheless, following the logic of Baise et al. (2011) as described in Section 2.1, these results are encouraging regarding the suitability of SH1D analysis for capturing site response at the SHA site.

As shown in Figure 5.6 and 5.9, strain levels for the aftershocks, while relatively small, are large enough that some modulus reduction effects are expected. Model-data comparisons are favorable at 50.8 m depth but show some over-prediction of motions at 2.4 m. The overprediction of shallow motions suggests that damping ratios are underestimated from the laboratory tests, which is generally consistent with previous findings by Tsai and Hashash (2009) and Elgamal et al. (2001), as described in Section 2.1. Accordingly, ground response analyses were repeated with small strain damping levels in soil increased to  $D_{min} = 2\%$  and  $5\%$  (generally

from approximately 1% in the original models). This increase in  $D_{min}$  causes the entire damping-strain curve to increase (the  $D$ - $D_{min}$  component is not affected) upwards by about 1% and 4% for  $D_{min} = 2\%$  and  $5\%$  respectively. As shown in Figure 5.12 and 5.13, the resulting spectra better matched the recorded data, especially in the FN direction and for the shallower accelerometers. The results do not strongly support either the 2% or 5% small stain damping levels as the preferred choice.

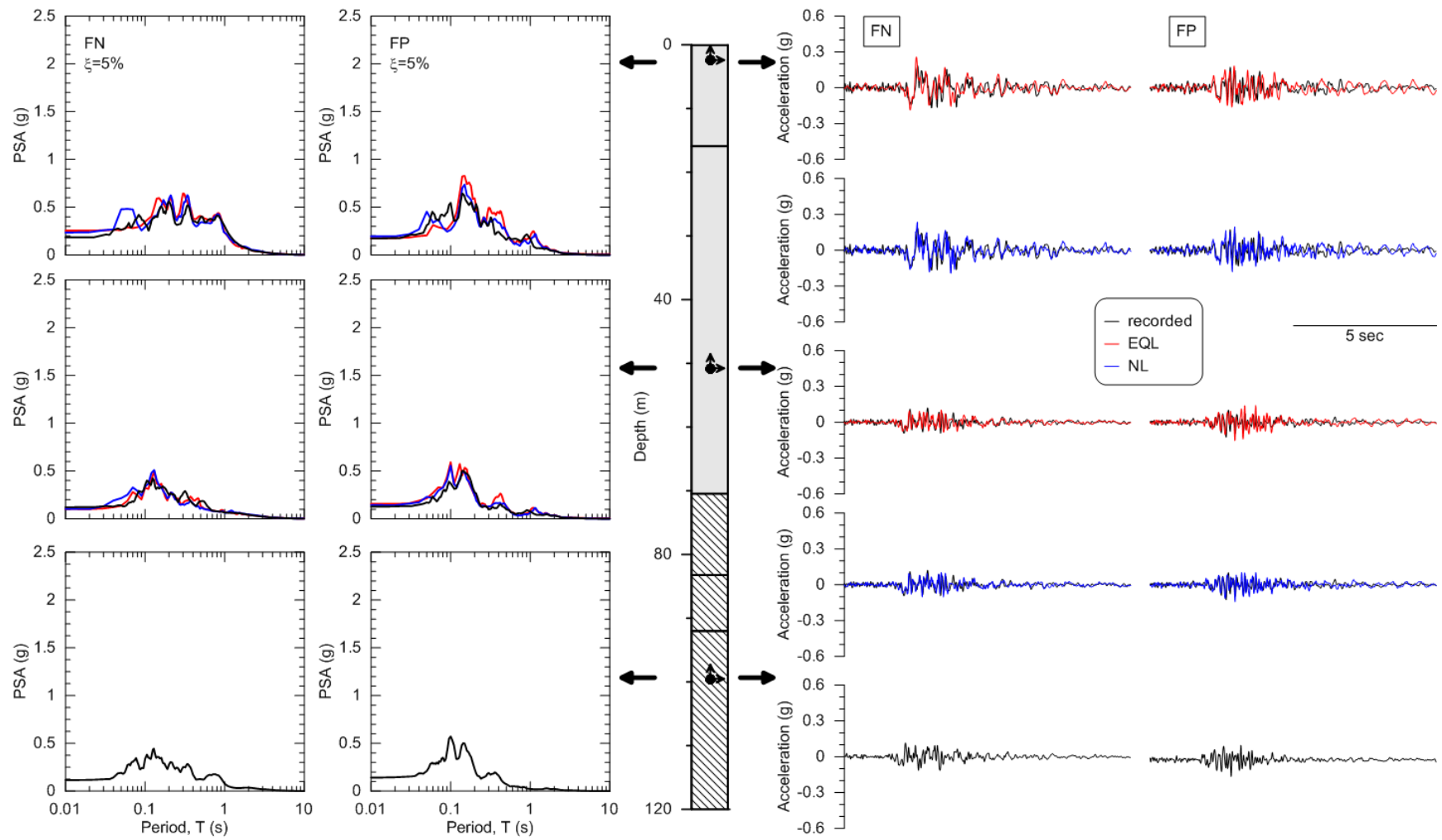


**Figure 5.5 Results of EQL and NL ground response analyses for aftershock L.**

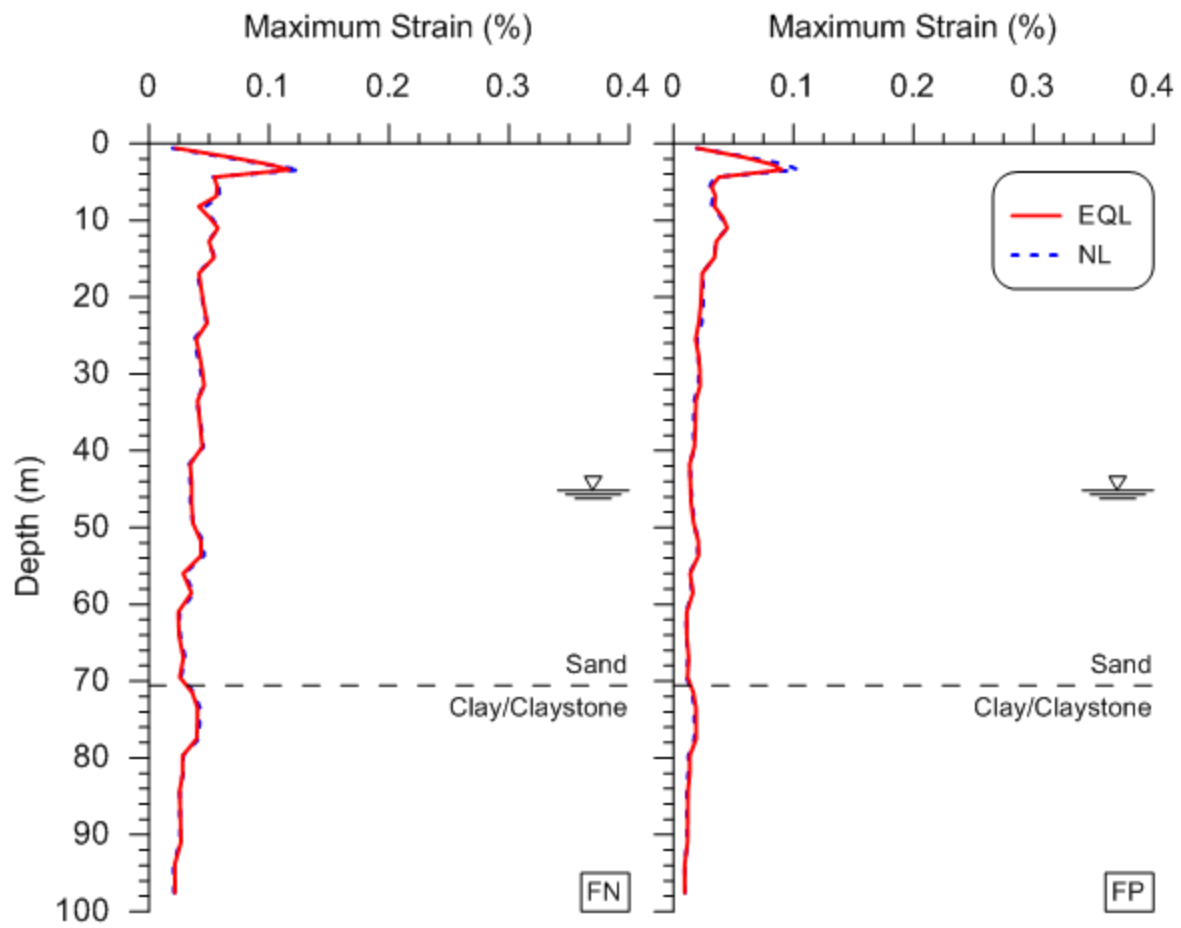


Figure 5.6 Peak strain profiles from EQL and NL analyses for aftershock L.

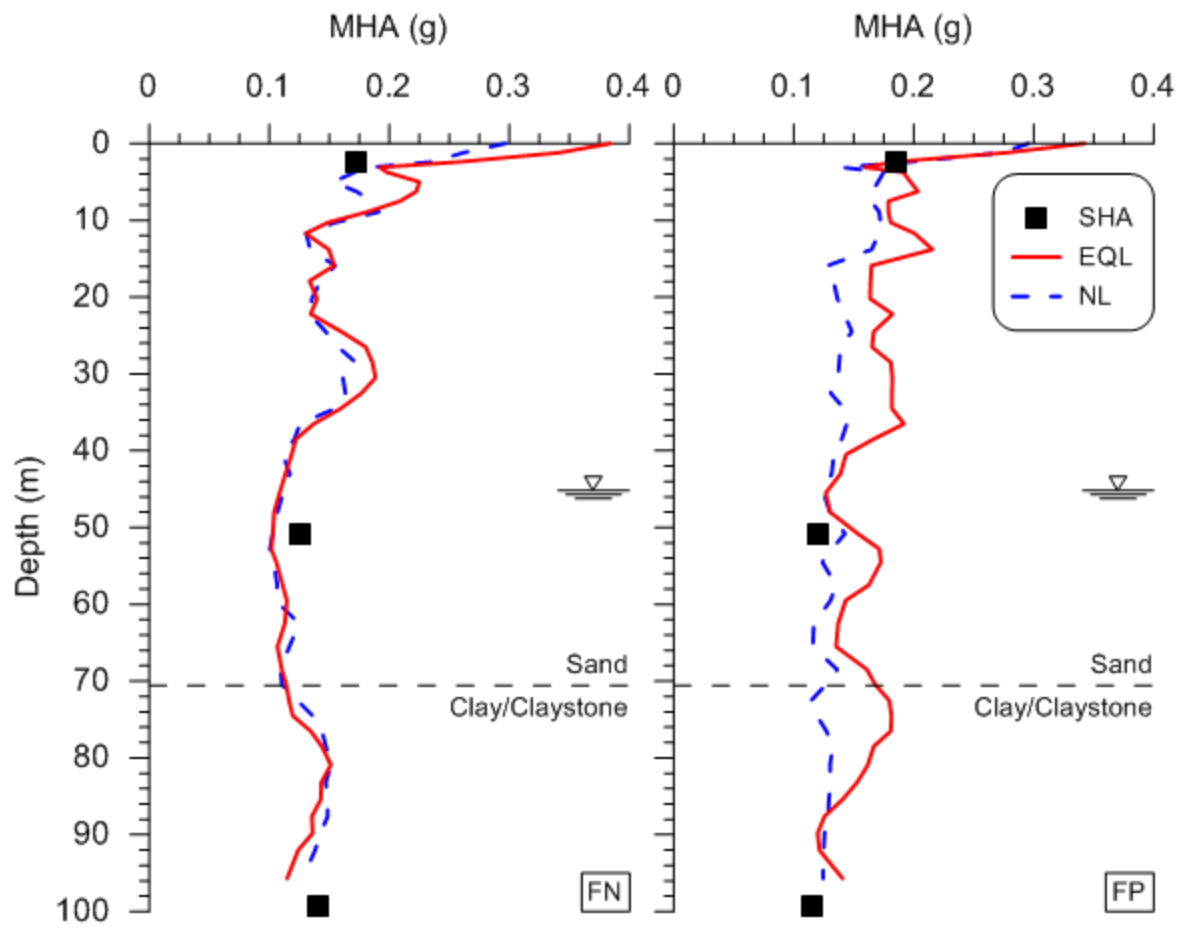
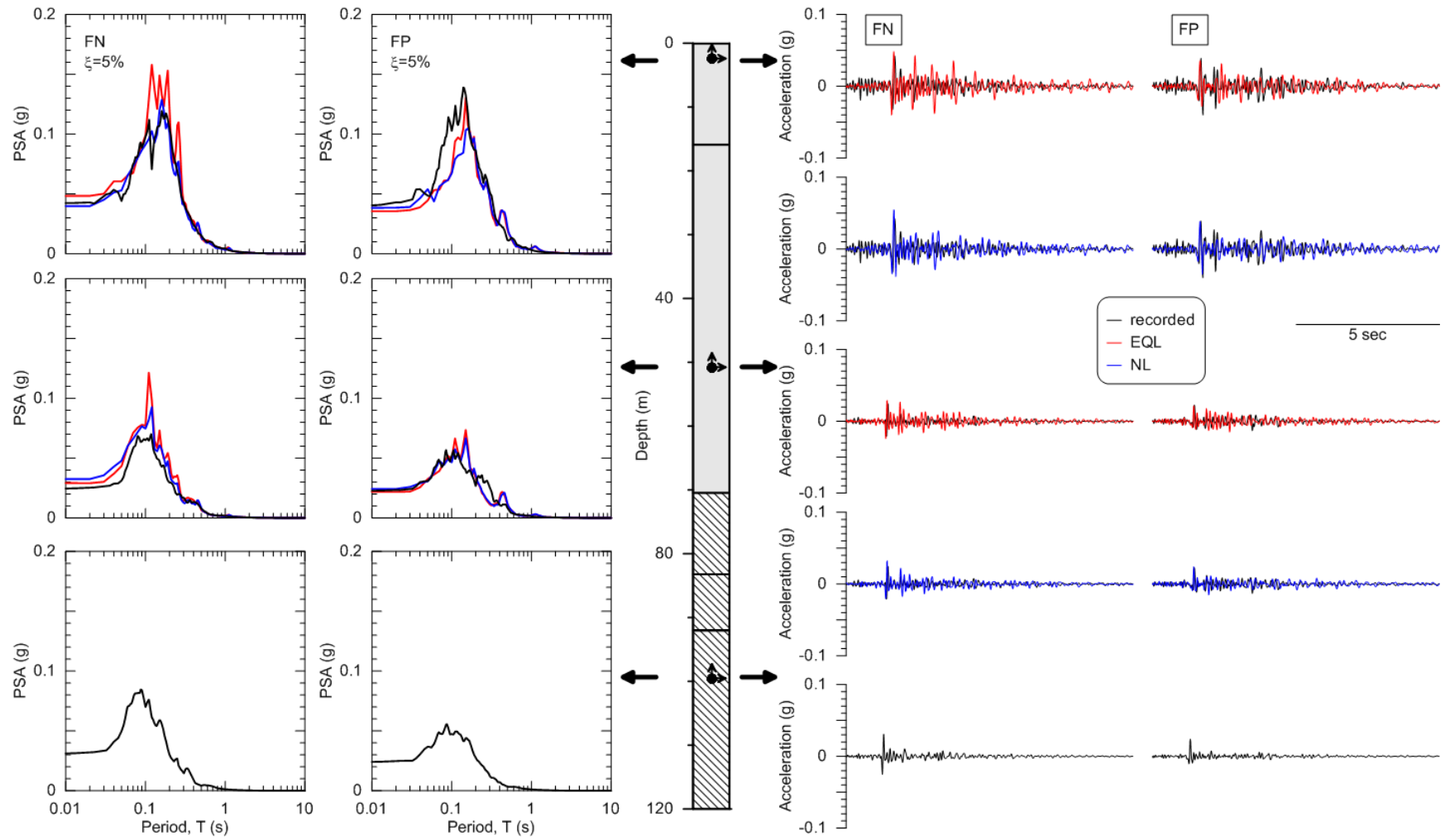


Figure 5.7 Peak accelerations from EQL and NL analyses for aftershock L.



**Figure 5.8 Results of EQL and NL ground response analyses for aftershock S.**



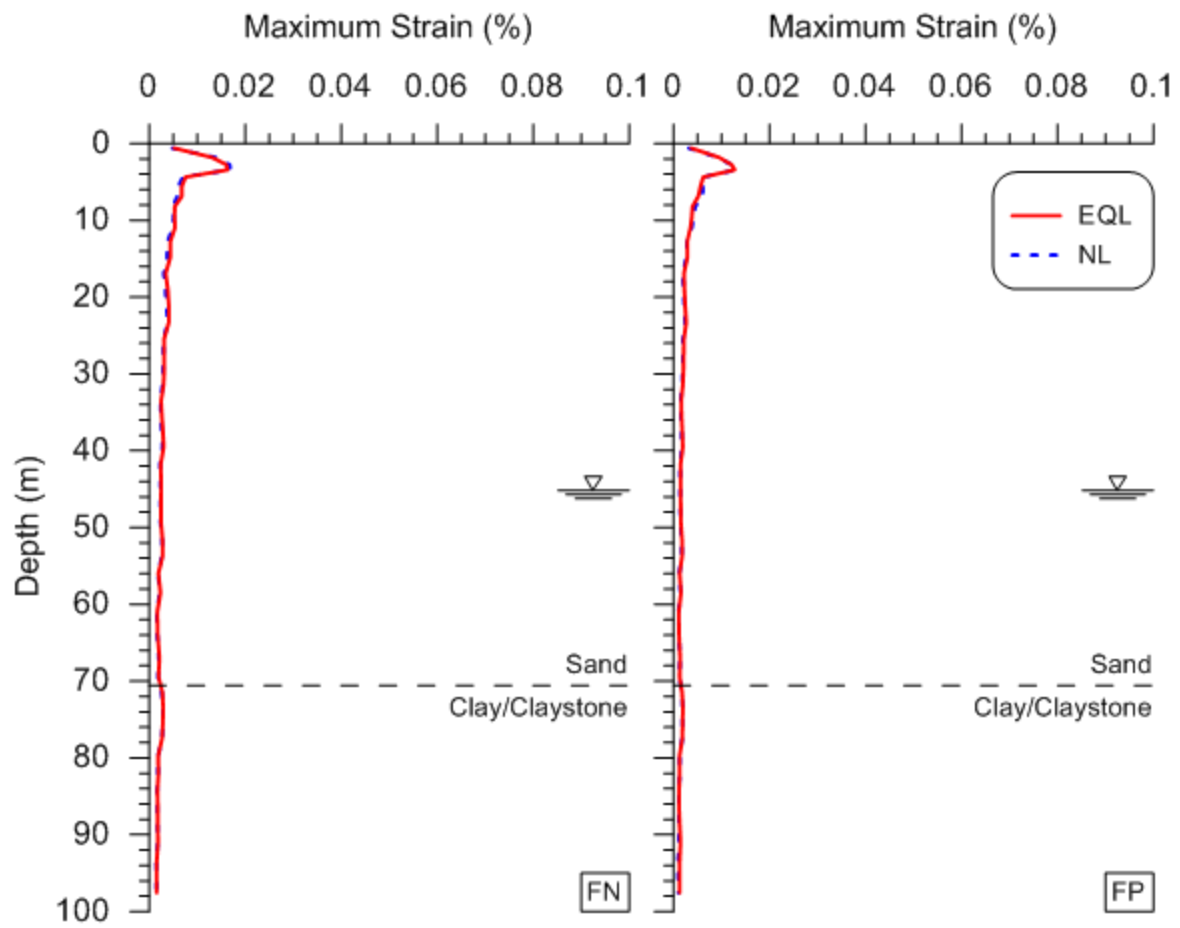


Figure 5.9 Peak strain profiles from EQL and NL analyses for aftershock S.

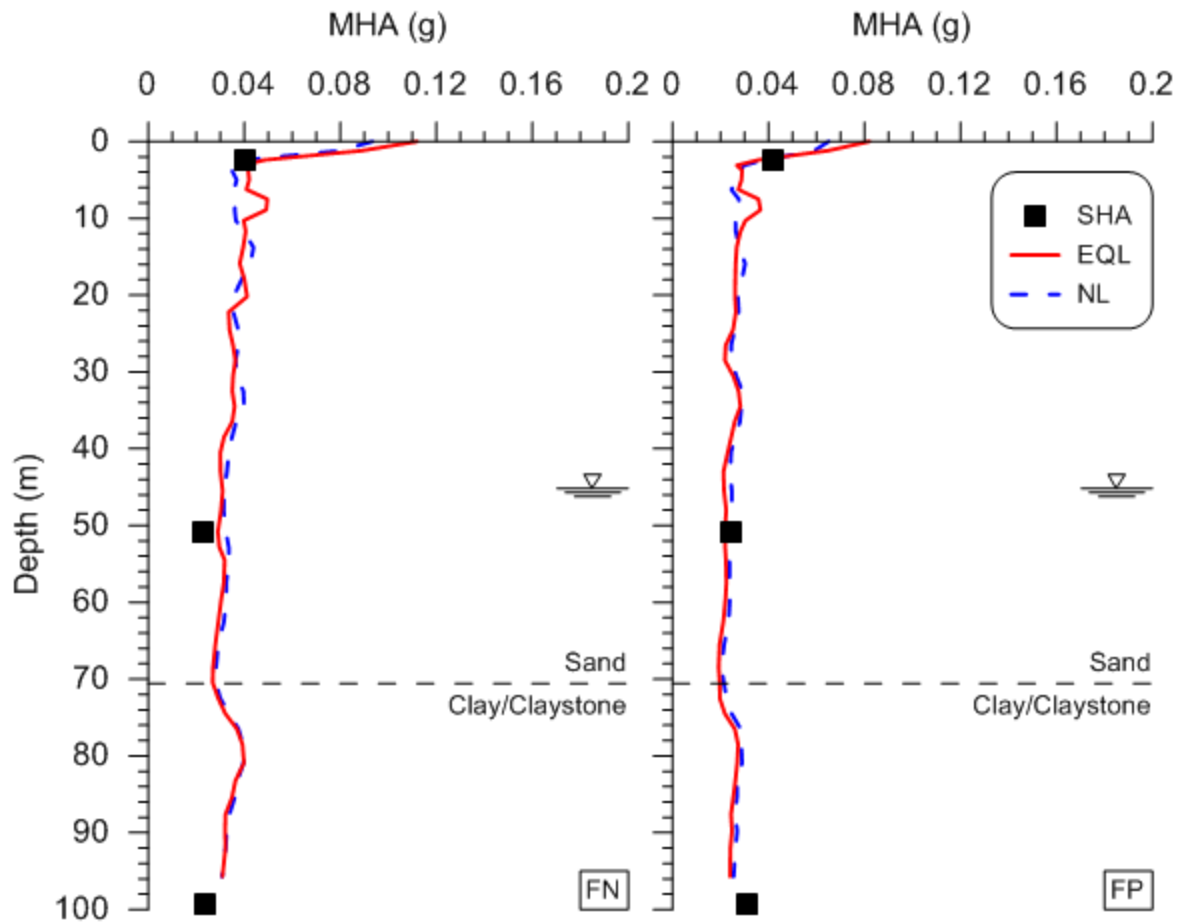


Figure 5.10 Peak accelerations from EQL and NL analyses for aftershock S.

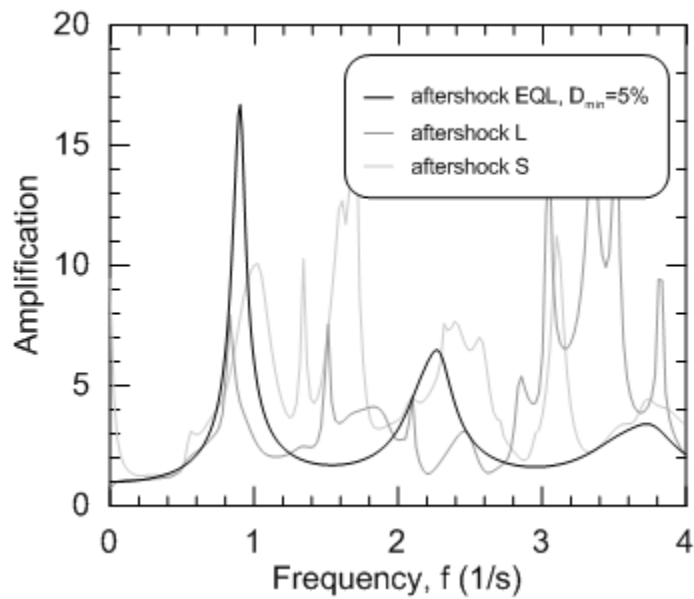
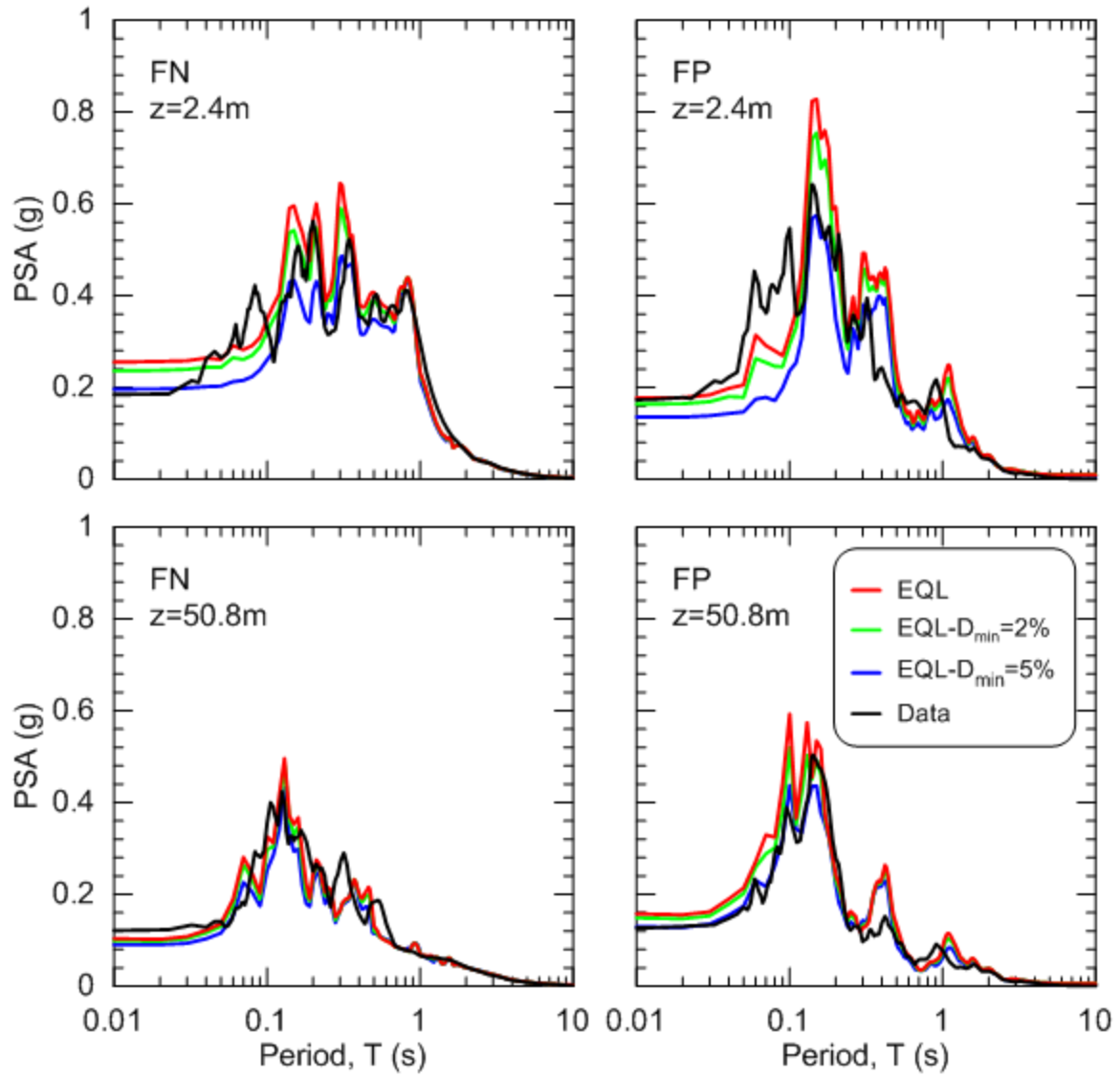
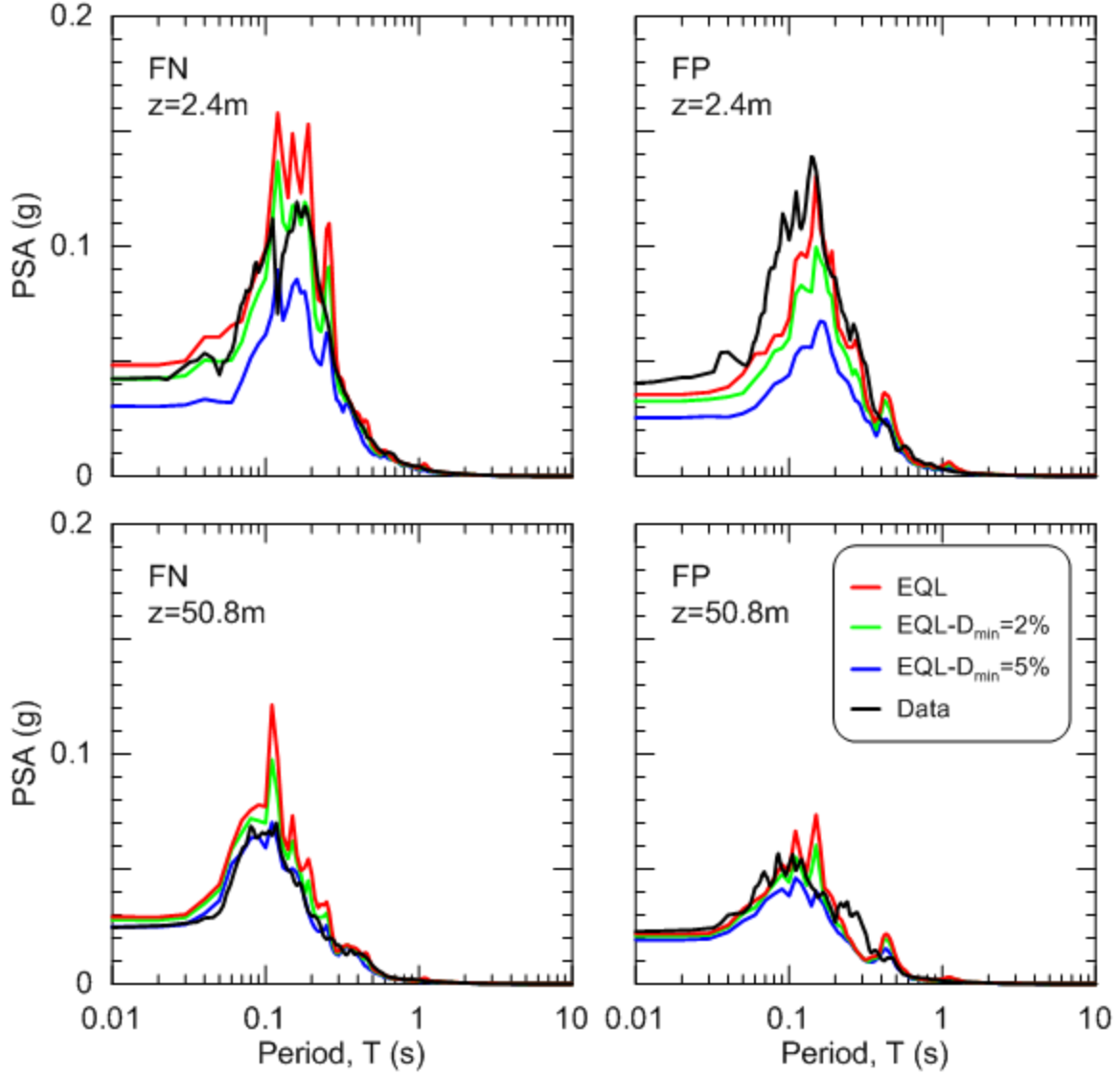


Figure 5.11 Transfer function and coherence for the main shock and two aftershocks.



**Figure 5.12 Response spectra at 5% damping for aftershock L and EQL analysis results for varying levels of small strain damping.**



**Figure 5.13** Response spectra at 5% damping for aftershock S and EQL analysis results for varying levels of small strain damping.

### 5.3 INITIAL GROUND RESPONSE ANALYSIS USING MAIN SHOCK RECORDINGS

Main shock ground response analyses were performed using the soil properties described in Section 5.1 with the exception of increased small strain material damping to  $D_{min} = 2\%$ , which corresponds to an additive increase to the damping curves of  $\Delta D_{min} \sim 1\%$ . This adjustment approximately doubles the small strain damping from the lab-based models, and was motivated by the aftershock analysis described in Section 5.2.

Figure 5.14 compares main shock results of the EQL and NL analyses with the SHA recordings at 2.4 and 50.8 m depth. The waveform comparisons indicate a relatively good fit during the 15-25 sec time interval plotted, which is the principal shear wave arrival window. Based on the waveforms and pseudo-acceleration response spectra (left side of figure), low frequency features of the motions are well predicted at both depths (50.8 m and 2.4 m) but high frequencies are slightly underestimated at 50.8 m and significantly overestimated at 2.4 m. The 2.4 m response spectra illustrate saturation of the EQL results to peak acceleration (as evidenced by flat short period spectral ordinates) for  $T < \sim 0.1$  sec. This saturation effect is evidence of poor performance of the EQL model at large strain, and is not present in the NL results or the data.

Insight into the causes of these trends is provided in Figure 5.15, which shows peak strain profiles from EQL and NL analysis. Computed peak strains in the sandy materials overlying rock are generally around 0.3-0.6%, although there is a spike in strains at about 50 m that exceeds the usable limit of the backbone curves (i.e., the upper bound strains from the RCTS tests). In Figure 5.16, we plot the backbone curve at 50 m depth obtained from the hyperbolic model along with the anticipated drained shear strength. The shear strength in Figure 5.16 is based on  $\tau_{ff} = \sigma_v' \tan \phi'$ , where  $\sigma_v'$  is the vertical effective stress and  $\phi'$  is the average friction angle from Table 3.1. Clearly the model is significantly underestimating the soil shear capacity in this depth range, which causes unrealistic strain localization. This localization is caused by the aforementioned dip in the  $V_s$  profile, as shown in Figure 1.3.

We also investigated the use of alternative smoothed velocity profiles in which there is no velocity dip at 50 m. Results from these analyses show a reduction in peak shear strains at 50 m, but significant increases in peak shear strains at other depths where the smoothed velocity profile has abrupt reductions. Hence, our conclusion is that the strain localization problem is for all practical purposes unavoidable with the backbone curves formulated in Section 5.1. In the next section we take additional steps to remove the strain localization effect and then re-examine the fit of the simulation results to data.

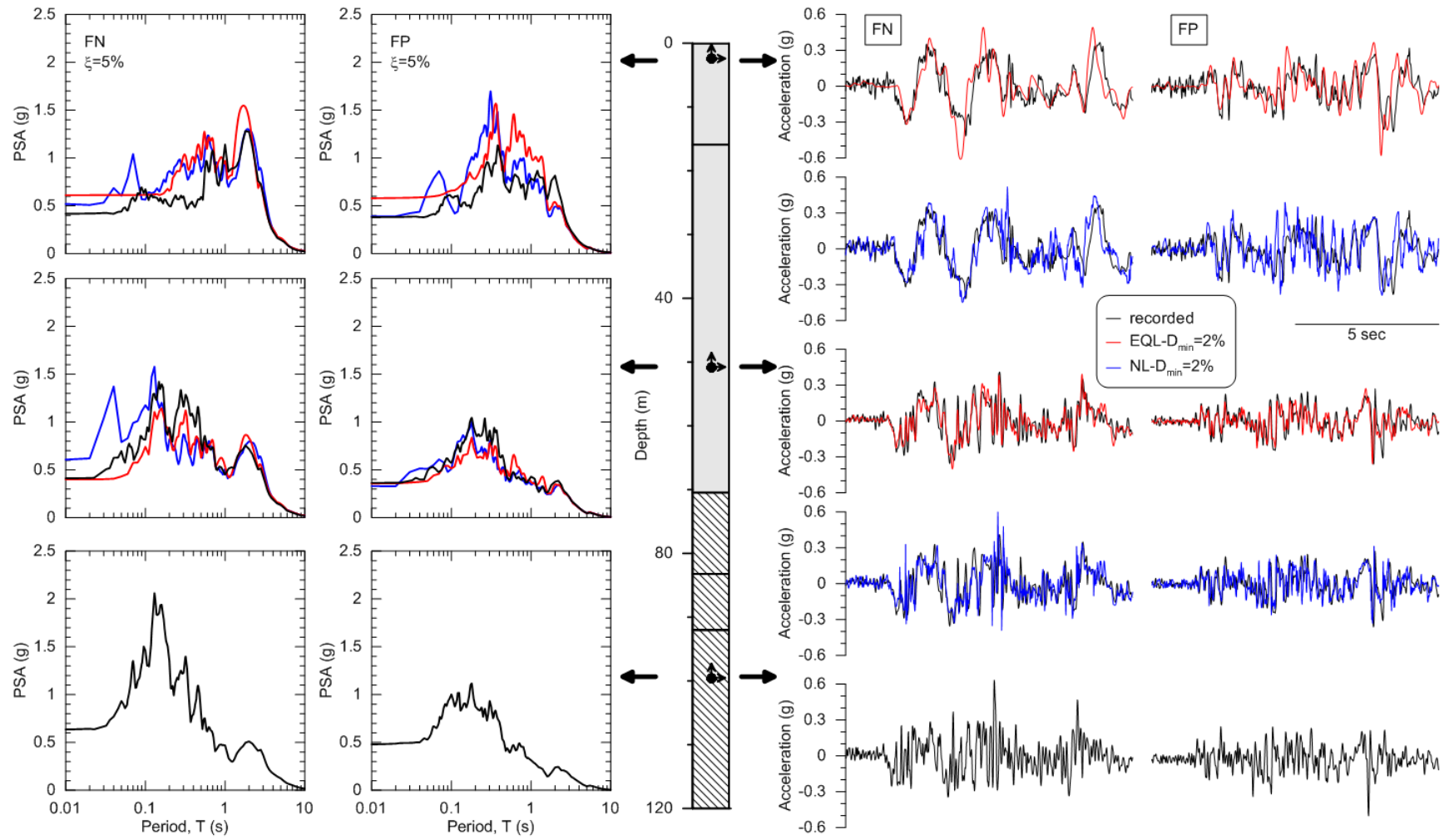


**Figure 5.14 Results of EQL and NL ground response analyses using increased damping ( $D_{min}=2\%$ ).**

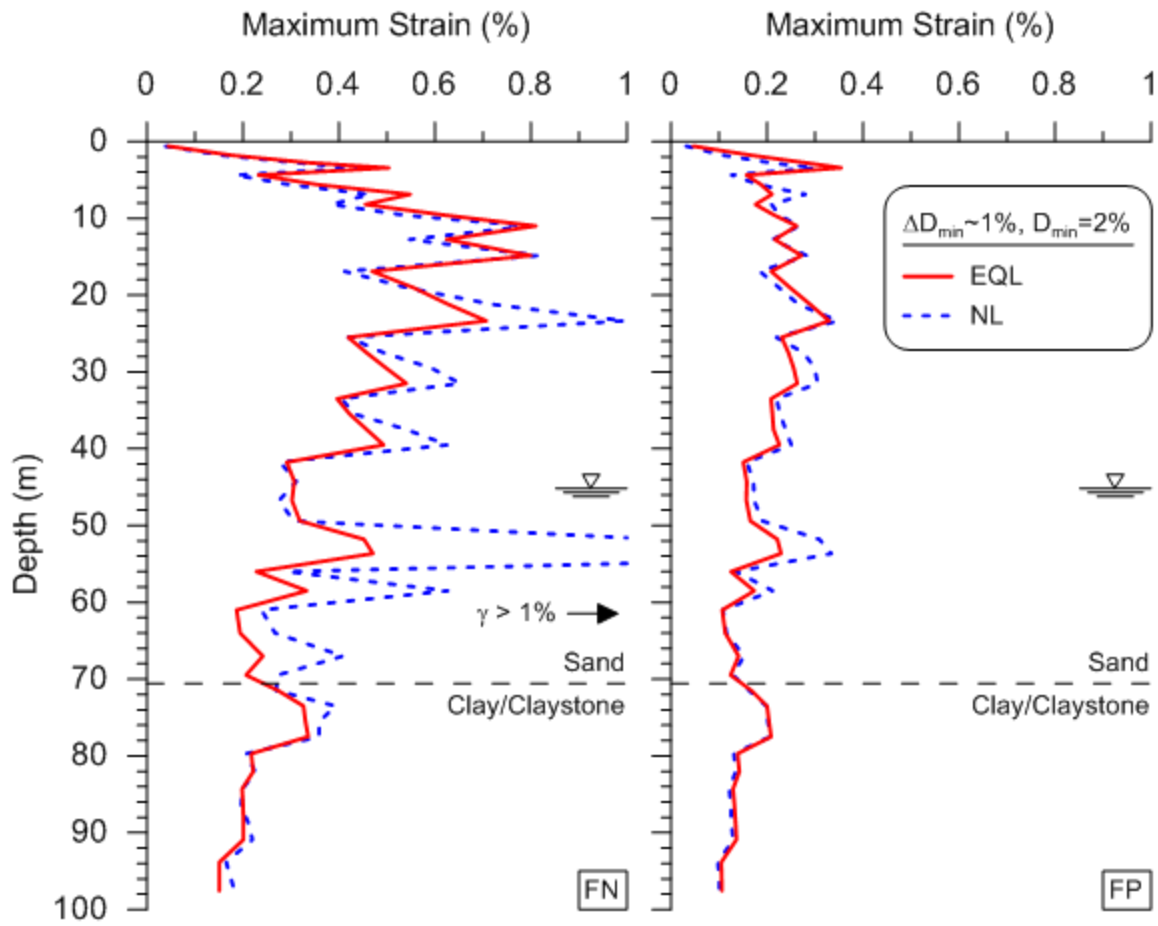


Figure 5.15 Peak strain profiles from EQL and NL analyses with increased damping ( $D_{\min}=2\%$ ).

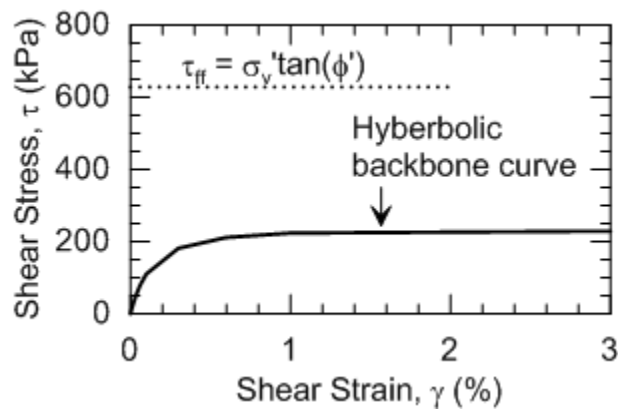


Figure 5.16 Comparison of backbone curve from fault normal nonlinear site response analysis at 50.8 m depth and estimated drained shear strength.

## 5.4 REVISED GROUND RESPONSE ANALYSIS CONSIDERING STRENGTH ADJUSTED BACKBONE CURVES AND INCREASED DAMPING

The shear localization that occurs at 50 m depth is evident from large maximum strains that are beyond the limits of the soil backbone curves developed from laboratory testing. This localization is considered unrealistic because the maximum shear stresses mobilized in the analyses are much lower than the shear strength as illustrated in Figure 5.16. To more properly reflect the soil strength, we propose a procedure to adjust the soil backbone curve to transition towards a specified shear strength at large strains while preserving the “small strain” behavior from modulus reduction curves. In this section, we describe this procedure, its implementation in DeepSoil, and the results of the analysis. The sensitivity of analysis results to small strain damping is also investigated.

### 5.4.1 Modification of backbone curve to capture shear strength

Figure 5.17 schematically illustrates the proposed approach for incorporating shear strength into the backbone curve. The procedure utilizes the traditional hyperbolic backbone curve described by Eq. (5.2) at shear strains  $\gamma < \gamma_l$ , where  $\gamma_l$  is a user-specified transitional shear strain. We refer to this as the *first hyperbola*. For  $\gamma > \gamma_l$  a *second* hyperbola is used having an initial modulus that is the tangent modulus of the first hyperbola at  $\gamma_l$  (denoted  $G_{\gamma_l}$ ), which ensures continuity of slope between the two hyperbolas. The second hyperbola asymptotically approaches the shear strength ( $\tau_{ff}$ ) at large strain. The equation of the second hyperbola can be written as:

$$\sigma - \tau_1 = \frac{G_{\gamma_l} \gamma'}{1 + \frac{\gamma'}{\gamma'_{ref}}} \quad (5.5)$$

where  $\gamma' = \gamma - \gamma_l$  and  $\gamma'_{ref} = \frac{\sigma_{ff} - \tau_1}{G_{\gamma_l}}$ . Eq. (5.5) matches Eq. (5.2a) except that  $\beta = \alpha = 1$ , the ordinates are expressed relative to a shifted set of axes with an origin at  $(\gamma_l, \tau_l)$ , and pseudo reference strain has been replaced by an adjustment of the classical reference strain of Hardin and Drnevich (1972) [ $\gamma'_{ref}$ ]. Tangent shear modulus  $G_{\gamma_l}$  is obtained as a derivative of Eq. (5.2a) evaluated at  $\gamma_l$  as:



$$\frac{G_{\gamma_1}}{G_{\max}} = \frac{1 + \left( \frac{\gamma_1}{\gamma_r} \right)^\alpha}{\left( 1 + \left( \frac{\gamma_1}{\gamma_r} \right)^\alpha \right)^2} \quad (5.6)$$

For  $\gamma > \gamma_1$  the secant modulus corresponding to points on the second backbone curve at  $(\gamma', \tau')$  can be evaluated as the sum of  $\tau_1$  (from Eq. 5.2) and  $\tau - \tau_1$  (from Eq. 5.5) normalized by the sum of  $\gamma_1$  and  $\gamma'$ . After manipulation to an equivalent modulus reduction relation we have:

$$\frac{G}{G_{\max}} = \frac{\frac{\gamma_1}{1 + \left( \frac{\gamma_1}{\gamma_r} \right)^\alpha} + \frac{G_{\gamma_1}/G_{\max} \gamma'}{1 + \left( \frac{\gamma'}{\gamma_{ref}} \right)^\alpha}}{\gamma} \quad \text{for } (\gamma > \gamma_1) \quad (5.7)$$

Strain  $\gamma_1$  must be selected such that  $\tau_1$  is less than  $\tau_{ff}$ .

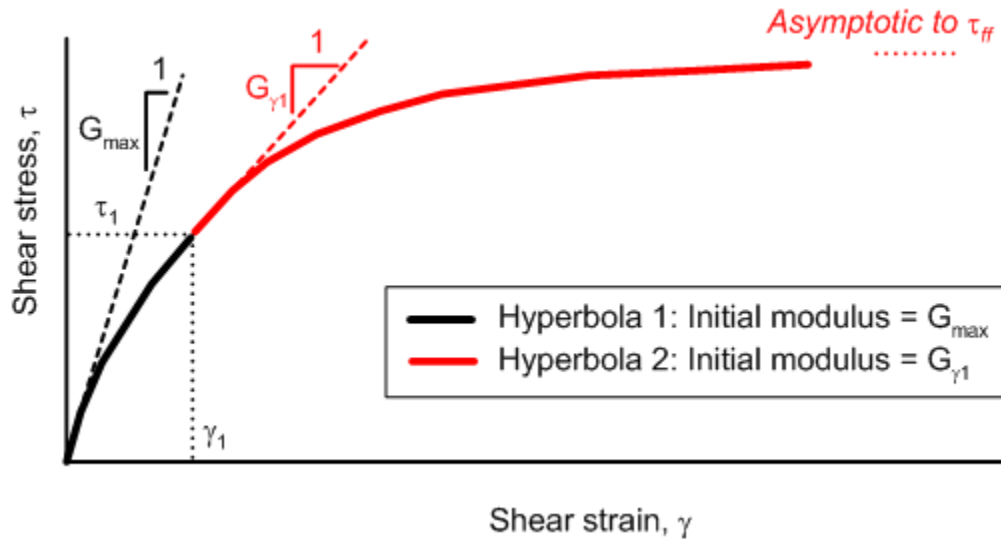


**Figure 5.17 Diagram for constructing shear strength adjusted modulus reduction curves.**

DeepSoil cannot accept the backbone curve functional form given above because it cannot be represented by a single hyperbola over the full range of strains. We use the fitting option in DeepSoil in which a target curve is specified as given above, and the best fit hyperbola is internally generated within the program.

### 5.4.2 Effects of modified backbone curves on analysis results

These new backbone curves were input into DeepSoil and the resultant fitted curves with no  $D_{min}$  adjustments are shown in Figure 5.18. Figure 5.18a, c, and e compare the initial model and strength adjusted modulus reduction curves at depths of 2.4, 8.2, and 50.8 m respectively, while Figure 5.18b, d, and f, compare the damping curves at depths of 2.4, 8.2, and 50.8 m respectively. The initial model tends to overestimate strength in shallow layers while underestimating strength in deeper layers. As described in Section 5.1, the damping curves have an unrealistic increase of large strain damping (e.g., at  $\gamma=1\%$ ) with depth due to the selected relation for  $\alpha$  (see Eq. 5.4), although this trend is not present at smaller damping levels ( $\gamma < \sim 0.3\%$ ).

We performed ground response analyses using main shock motions, strength adjusted backbone curves, and damping curves in soil modified to  $D_{min} = 2\%$  based on the aftershock calibration. Results of these simulations are shown in Figure 5.19-5.21. Figure 5.20 shows that the strain localization problem has been removed with the strength adjustment to the backbone curves. Figure 5.19 shows both strength adjusted EQL and NL analyses to over-predict response spectral ordinates across the majority of periods from PGA to 2 sec at shallow depths. At 50 m the predicted and recorded response spectral shapes match well although there are some misfits in amplitude; particularly noteworthy is the FN peak near 0.1 sec that is captured well with the strength adjusted curves but is lost in prior analysis due to strain localization. Comparison of the FP predictions in Figure 5.19 and 5.14 indicates that the strength adjustments are less important for this direction due to the lower strain levels. Examining the waveforms, we see in Figure 5.19 that NL analyses better represent the high frequency energy content in the initial portions of the strong shaking interval relative to EQL analysis.

Figure 5.21 compares the peak accelerations within the soil column from the EQL and NL analyses and from recordings. Results are shown for analyses before and after strength adjustment to the backbone curves. In the FN direction, peak accelerations from NL analysis are over-predicted at both depths (consistent with the findings from response spectra) and the strength adjustment to the backbone curves significantly increases the overprediction. This behavior is not evident in the FP direction where strains were lower. Peak accelerations from EQL analyses are closer to observed values for the FN direction.

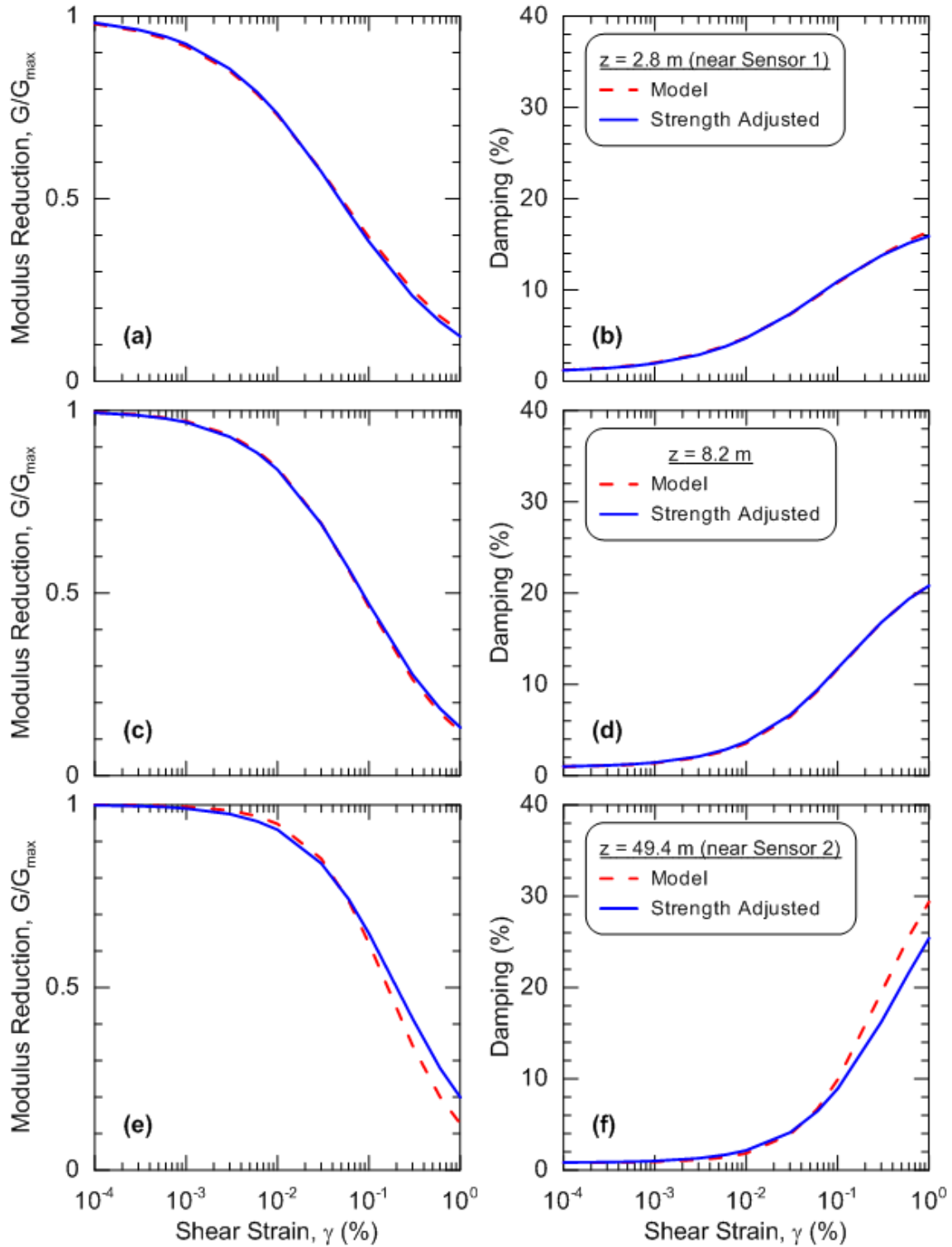


**Figure 5.18** Comparison of the original and strength adjusted (a) modulus reduction and (b) damping models for the layer of soil containing the first sensor, (c) modulus reduction and (d) damping models for a layer at 8.2 m depth, and (e) modulus reduction and (f) damping models for the layer of soil containing the second sensor.

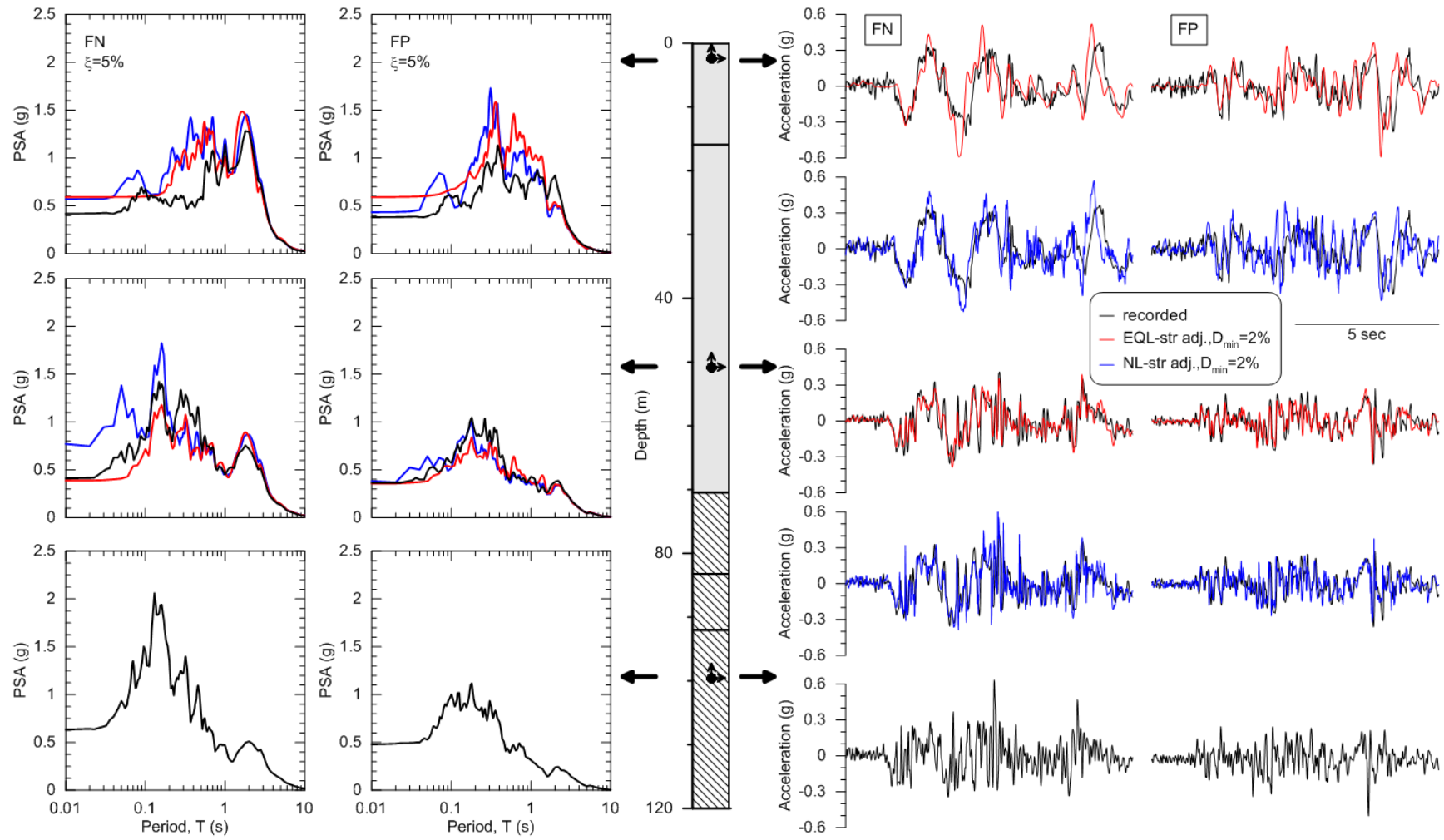


**Figure 5.19 Results of strength adjusted EQL and NL ground response analyses.**

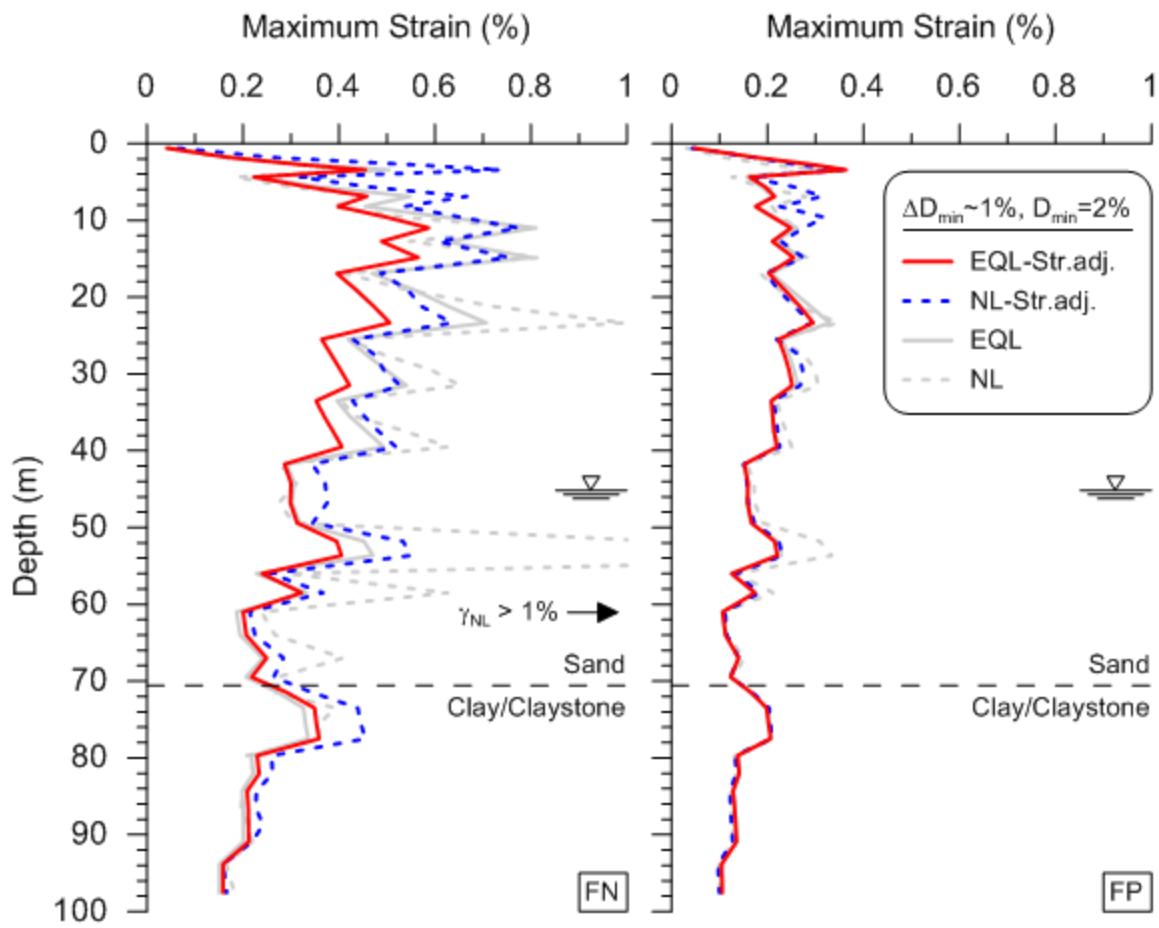
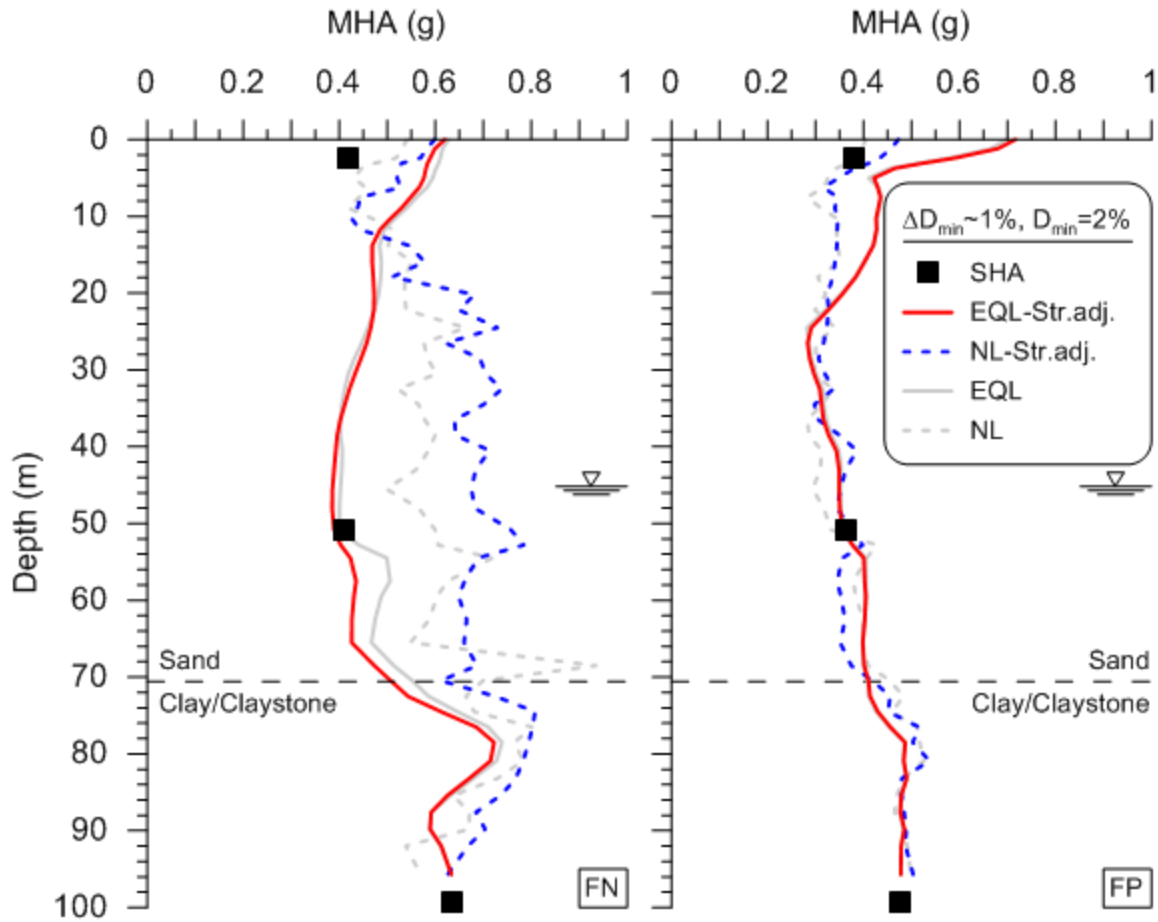


Figure 5.20 Peak strain profiles from strength adjusted EQL and NL analyses.



**Figure 5.21 Peak accelerations from strength adjusted EQL and NL analyses.**

### 5.4.3 Damping adjustment

The discrepancies in response spectra and peak acceleration profiles further support the need to increase damping as described in Section 5.2. We evaluated the sensitivity of the Deepsoil results to small strain damping in soil by increasing  $D_{min}$  from 2% to 5% and 10%, which correspond to  $\Delta D_{min} \sim 4\%$  and  $9\%$  respectively. The effects of these changes in damping on response spectral ordinates are shown in **Error! Reference source not found.**. As expected, general spectral shapes before and after these adjustments are comparable, although high frequency ordinates are reduced. Our interpretation of the results in **Error! Reference source not found.** is that a minimum damping of  $D_{min} = 5\%$  performs reasonably well for both directions and at both depths. This level of damping is within the range that was considered applicable from analysis of the aftershock data. Adjusting  $D_{min}$  to 10% overdamps the response, particularly for the FP direction and is also evident in the maximum horizontal acceleration profile, shown in Figure 5.23.

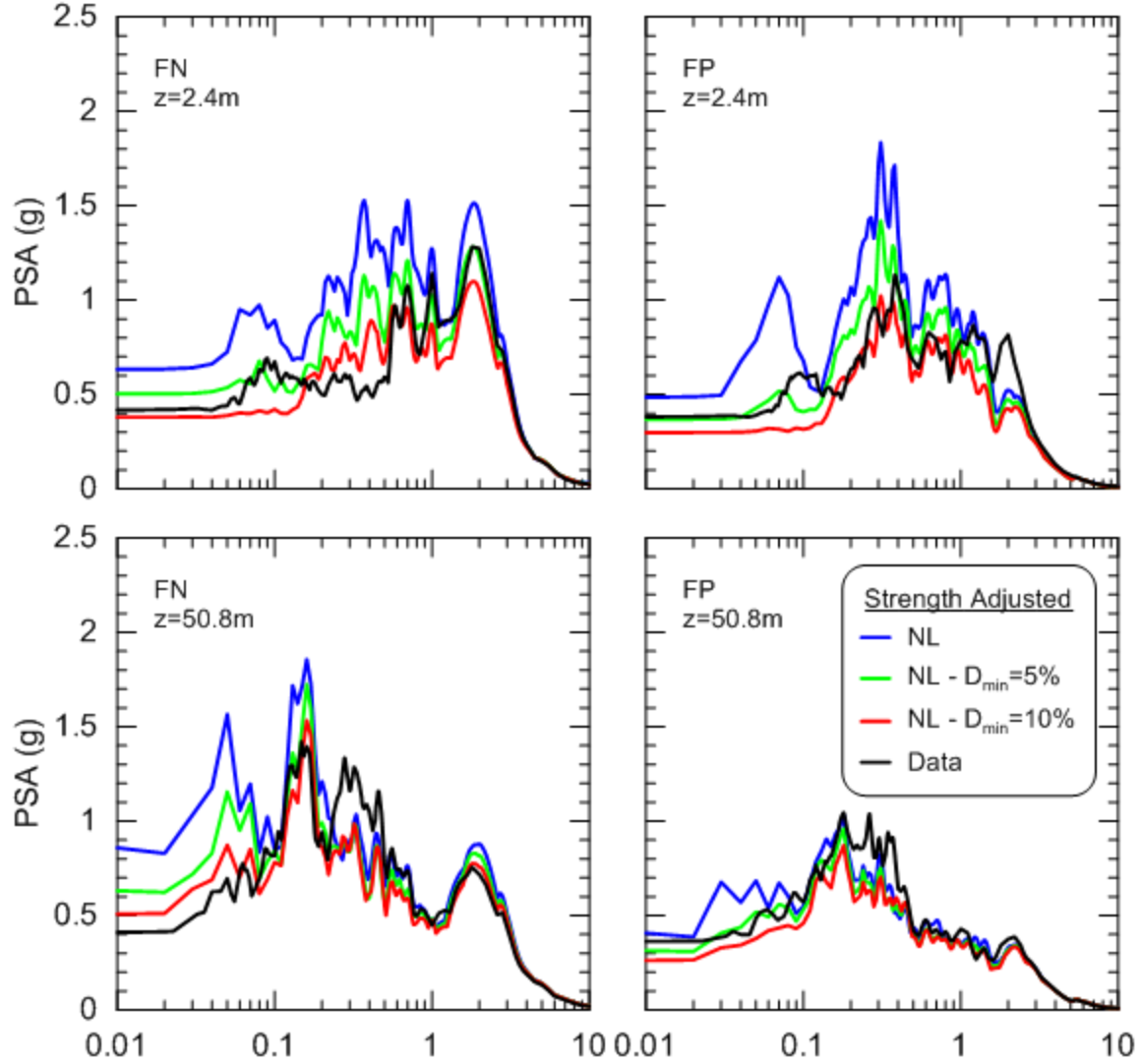


**Figure 5.22 Response spectra at 5% damping for main shock and NL analysis results using strength adjusted backbone curves and varying levels of small strain damping**

Figure 5.24 show MHA profiles, response spectra and wave forms, and strain profiles from strength adjusted ground response analyses with  $D_{min}$  in soil set to 5%. We do not show EQL in this figure because the EQL MHA are shown in Figure 5.21 and are not sensitive to  $D_{min}$ . The simulation-data comparisons of waveforms, response spectra, and MHA profiles are more favorable for this set of simulations than those presented previously. The strain profile in Figure 5.25 is not significantly affected by the damping change (i.e., it is similar to that in Figure 5.20). Those strain levels are generally low enough that the unrealistic increase of large-strain damping with depth (which results from the  $\alpha$  model in Eq. 5.4) is unlikely to affect the results. EQL

analyses estimate lower peak strains than NL analyses. As before, the differences between NL and EQL analyses are most evident from low-period saturation of EQL spectra and the loss of high frequency ground motion components in the EQL waveforms.

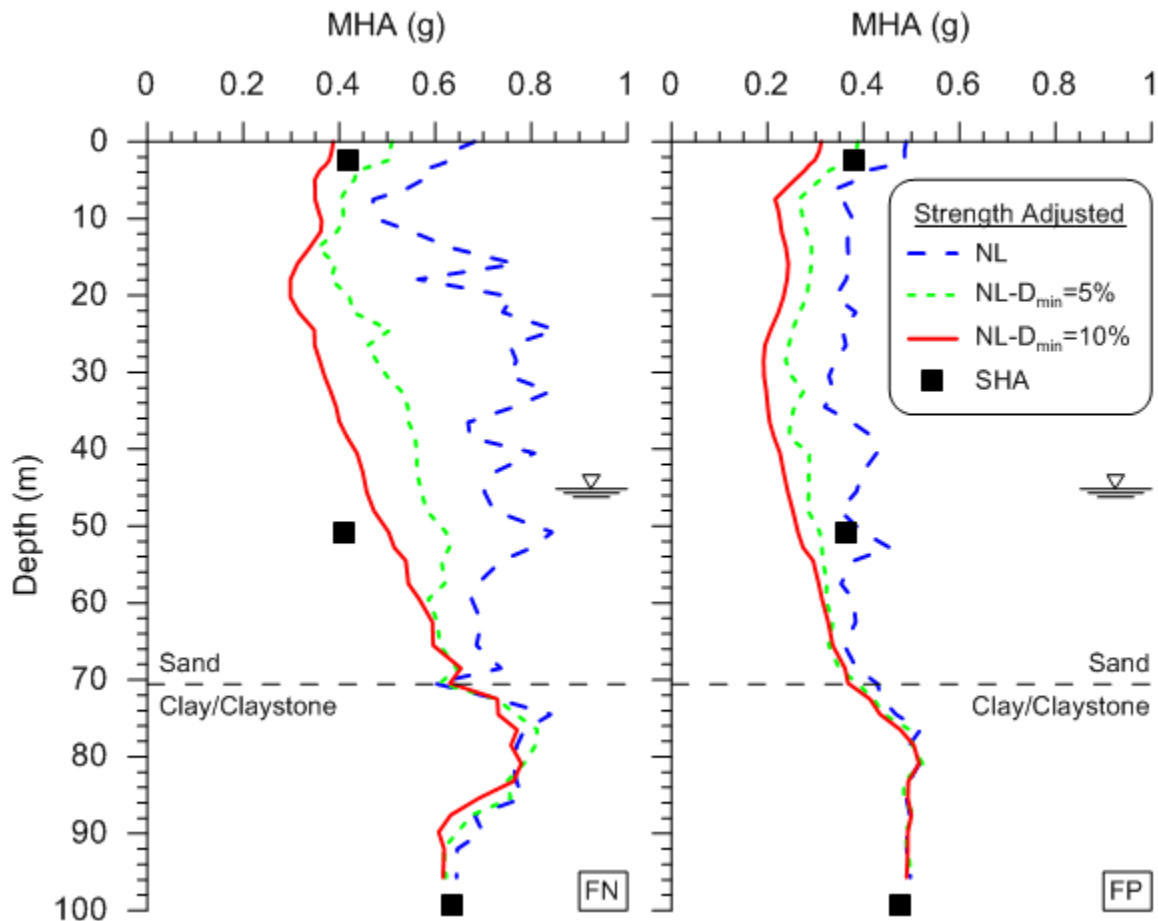


**Figure 5.23 Peak accelerations from increased damping on strength adjusted NL analyses.**



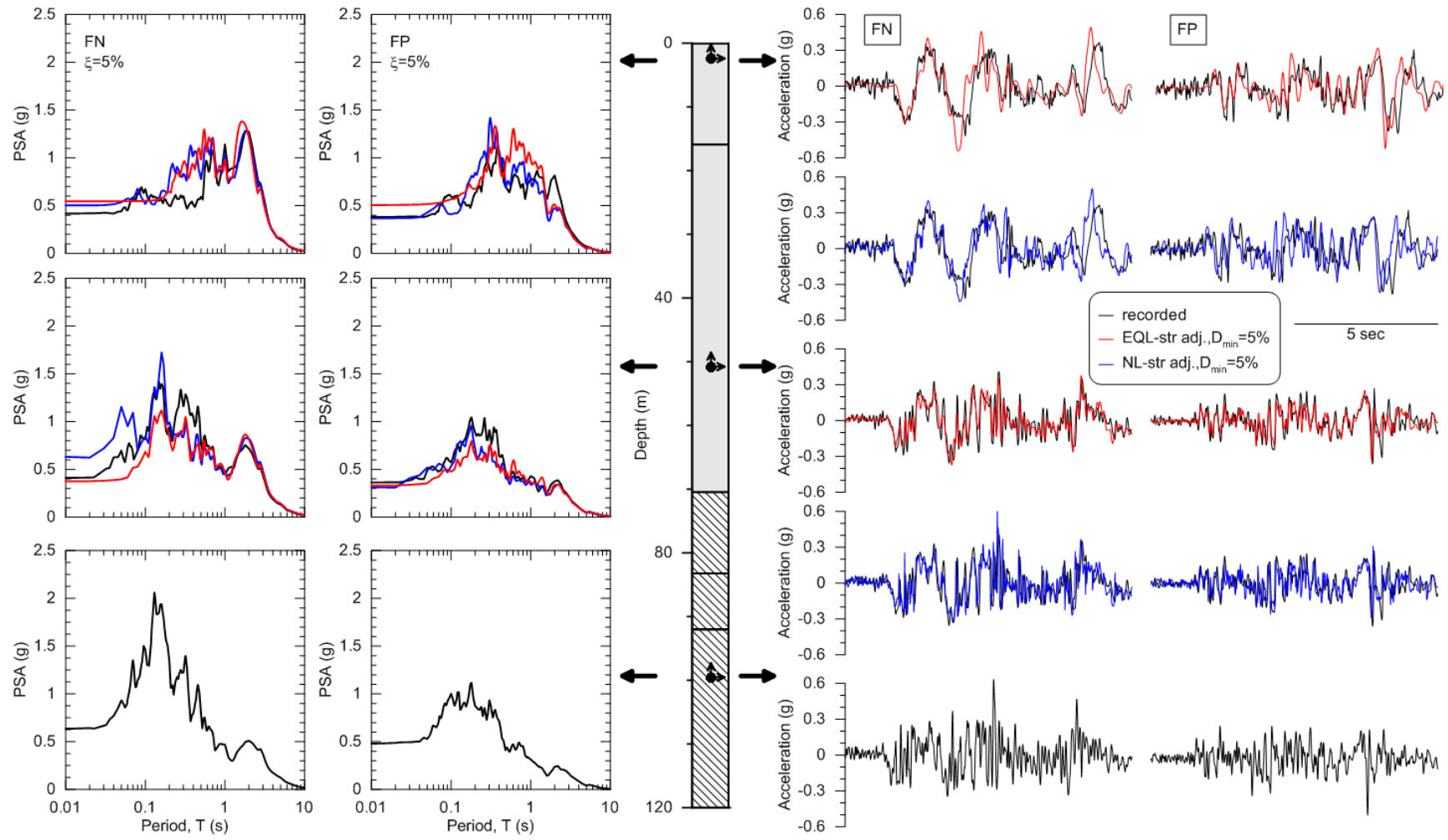


**Figure 5.24 Results of strength adjusted EQL and NL ground response analyses with increased damping.**

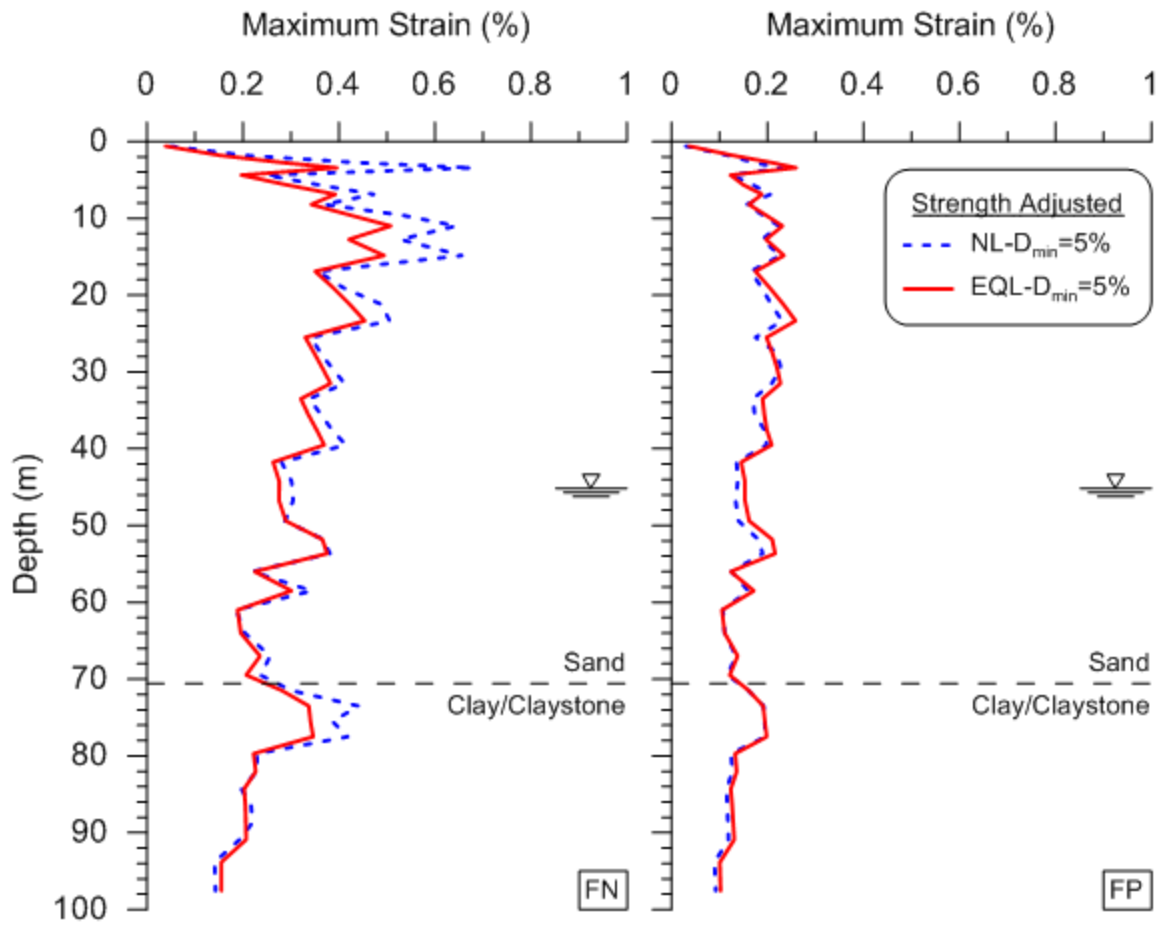


**Figure 5.25 Peak strain profiles from strength adjusted EQL and NL analyses with increased damping.**

## 6. Ground Failure Analysis

Significant damage to utility pipelines and non-reactor structures occurred at the KKNPP that was attributed to settlement from seismic compression (Sakai et al., 2009; Tokimatsu, 2008). The area in the immediate vicinity of the SHA experienced approximately  $15 \pm 5$  cm of settlement based on multiple sets of observations as described in Chapter 1. There was no obvious evidence of liquefaction manifest at the ground surface.

### 6.1 POTENTIAL FOR LIQUEFACTION AT DEPTH

In this section, we evaluate the potential for liquefaction of the soils below the water table, specifically at 50 m depth where a relatively low blow count was recorded  $[(N_1)_{60} \approx 20]$  and relatively sizable strains are expected on the basis of ground response analysis (peak strains of 0.3-0.4%, Figure 5.25). Seismic demand is computed as a magnitude- and overburden-adjusted Cycle Stress Ratio,  $CSR$ , computed as (modified from Seed and Idriss, 1971):

$$CSR_{M=7.5, \sigma'_v=1atm} = 0.65 \left( \frac{\tau_{max}}{\sigma'_v} \right) \frac{1}{MSF} \frac{1}{K_\sigma} \quad (6.1)$$

where  $\tau_{max}$  is the peak shear stress from ground response analysis,  $\sigma'_v$  is the vertical effective stress,  $MSF$  is the magnitude scaling factor = 1.3, and  $K_\sigma$  is the overburden correction factor, which depends on relative density, and ranges from 0.82 for  $D_R = 40\%$  to 0.72 for  $D_R = 65\%$  (Idriss and Boulanger, 2008). Based on Eq. 6.1, we find  $CSR$  to range from 0.16 to 0.18 considering the range of relative densities and stresses computed from the strength and damping adjusted NL analyses. These values of  $CSR$  plot below the liquefaction triggering curves (cyclic resistance ratio  $CRR = 0.20$  for  $(N_1)_{60cs} = 20$ ), suggesting that liquefaction was unlikely to have occurred at depth at the SHA site. For EQL analysis, the peak shear stresses are somewhat higher (this is expected given the constant shear modulus assumption in the EQL method) and provide a

CSR range of 0.19 to 0.21. The EQL analyses are considered less credible given the large-strain response of the soil in this depth interval.

## 6.2 SEISMIC COMPRESSION

In the remainder of this chapter, we compute ground settlement from seismic compression for comparison to the observations. Seismic compression analysis requires evaluation of seismic demand in the form of effective strain profiles and equivalent numbers of strain cycles combined with a volumetric strain material model (e.g. Figure 3.3).

Site specific analyses utilize shear strain demands computed from ground response analyses and a site-specific VSMM. The effective shear strain at depth  $z$  is taken as 65% of the maximum strain from NL site response analysis (i.e. in Figure 5.25),

$$\gamma_{eff}(z) = 0.65 \times \gamma_{max}(z) \quad (6.2)$$

The equivalent number of cycles of the ground motions at shear strain level  $\gamma_{eff}$  can be evaluated using procedures described in Liu et al. (2001). As described in Liu et al. (2001) and Stewart et al. (2002), the relative weighting of peaks with different amplitudes is evaluated based on laboratory-derived relationships between cyclic shear strain amplitude ( $\gamma_c$ ) and the number of cycles to induce a particular level of performance (i.e., particular levels of vertical strain in the case of seismic compression problems). Those relationships tend to be linear in log-log space, as shown in Figure 6.1 for the KKNPP soil material. The weight factors assigned to peaks with different amplitudes is related to the slope of the linear relationship. As shown in Figure 6.1, this slope was taken as -0.4 from laboratory testing of the KKNPP soil material. Using these procedures, the equivalent number of cycles was computed from calculated strain histories derived from EQL analysis, with the results shown in **Error! Reference source not found.** NL analyses could not be used due to permanent offsets in the strain histories.

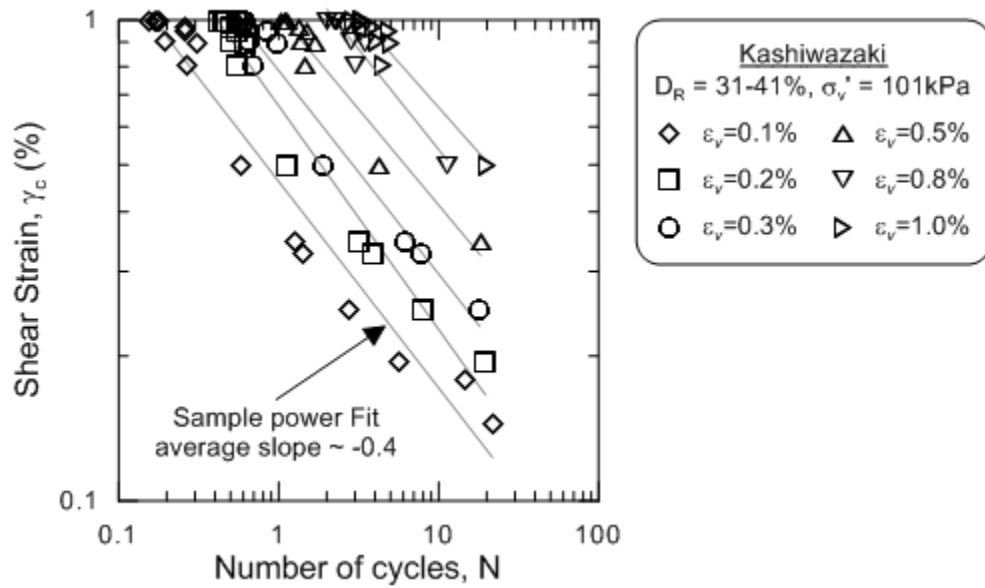


Figure 6.1 Relationship between shear strain amplitude,  $\gamma_c$ , and number of cycles,  $N$ , to cause selected amounts of vertical strain,  $\varepsilon_v$ .

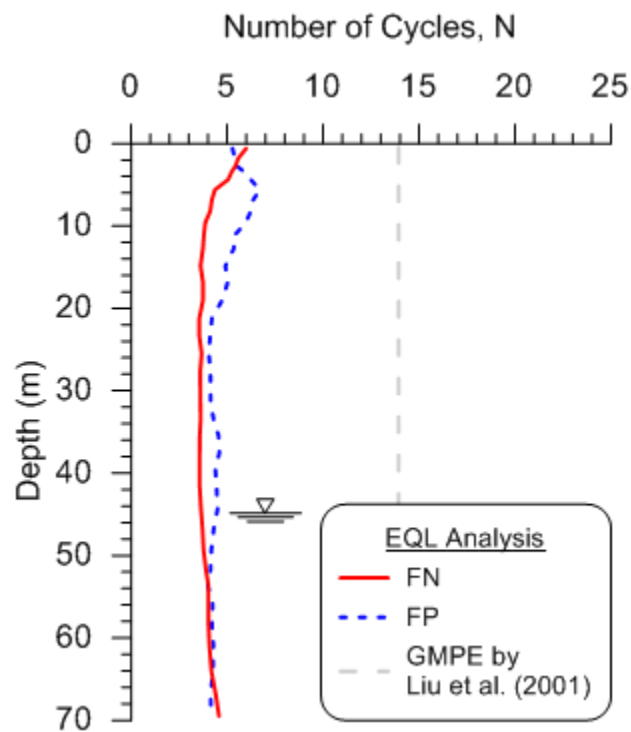


Figure 6.2 Number of cycles from strength adjusted EQL analysis.

Vertical strains for each component of ground motion at depth  $z$  are calculated as:

$$\varepsilon_v(z) = a \times K_{\sigma,\varepsilon}(z) \left[ \gamma_{eff}(z) - \gamma_{iv} \right]^b \times C_N \quad (6.3)$$

where  $\gamma_{eff}(z)$  is taken from the ground response analysis results (shown in left plot of Figure 6.3), parameters  $a$  and  $b$  are as given in Figure 3.3 [regressed from simple shear test data; results similar to the Duku et al. (2008) relation for this material]. Overburden correction term  $K_{\sigma,\varepsilon}(z)$  is taken as a function of vertical stress from the model of Duku et al. (2008), which has been verified from material-specific testing as shown in Figure 3.3e. Parameter  $C_N$  is taken from Eq. (3.6) with  $R=0.31$  and  $N$  taken from **Error! Reference source not found.**. These analyses are repeated for both the FN and FP directions, with the resulting settlements being 9 and 3 cm, respectively for  $D_R = 40\%$  and 6 and 2 cm, respectively for  $D_R = 65\%$ . Figure 6.3 shows the distribution of vertical strain along the soil profile and indicates a majority of the deformations occurred in the upper 25 m. Following the findings from 2D testing (Sections 3.2.4 and Figure 3.5), these two settlements are summed, leading to predicted settlements from horizontal ground motions of about 12 and 8 cm for  $D_R = 40\%$  and  $65\%$ , respectively.

As shown by Pyke et al. (1975) and described in Section 2.2, the application of vertical ground motion in combination with horizontal ground motion increases volumetric strains by amounts ranging from approximately 20% to 50% for effective vertical accelerations between 0.15 to 0.3g. The peak vertical accelerations at the KKNPP site (shown in Figure 4.2) are about 0.25g at depth (50 m and below) and 0.6g near the surface. Given that most of the seismic compression occurs in the upper 25 m, a reasonable value for the effective vertical acceleration in the depth range of principal interest is approximately 2/3 of 0.6g or 0.4g. This value of effective vertical acceleration supports a volumetric strain increase of approximately 50%, leading to predicted settlements in the range of 12-18 cm, which are reasonably consistent with the measured range of  $15 \pm 5$  cm at the site.

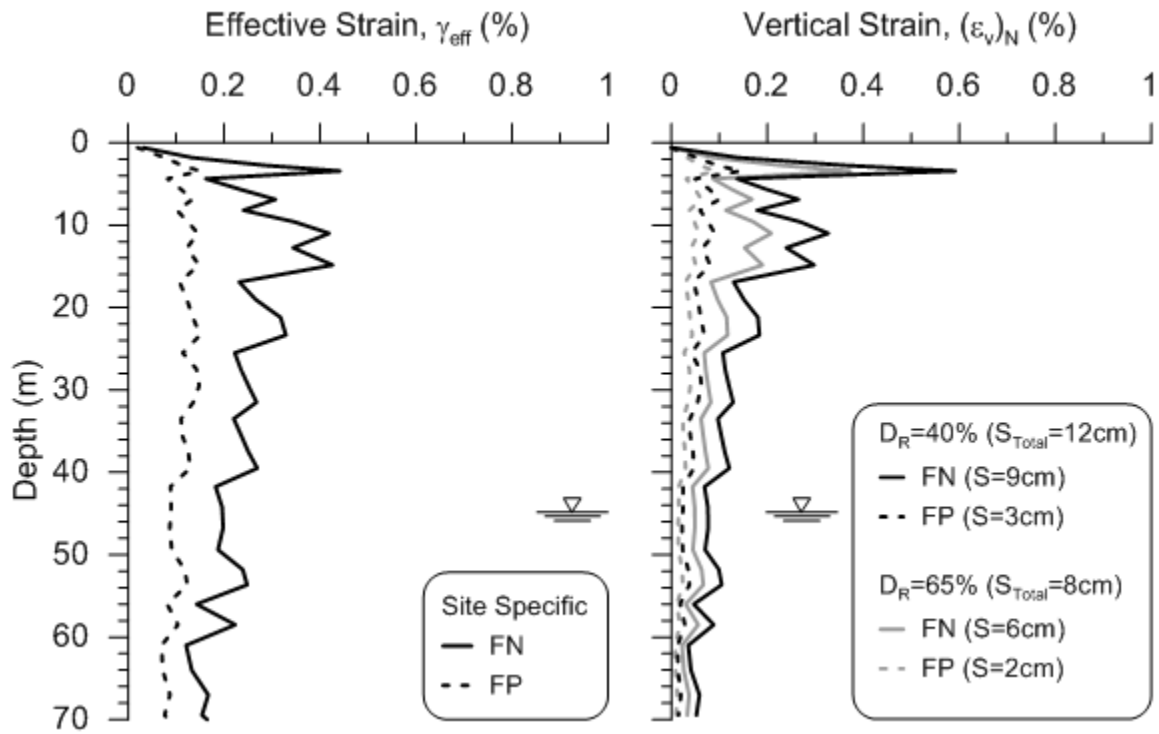


**Figure 6.3 Sample effective strain demand profiles, vertical strain profiles, and resultant settlements from a site specific analysis for  $D_R = 40$  and 65%.**

## 7. Summary and Conclusions

The 2007 Niigata-ken Chuetsu-oki earthquake was recorded at the KKNPP site by a series of surface and downhole instruments. In this study we have focused on the data from the service hall array (SHA) site where geometric mean peak accelerations at the ground surface were 0.44 g and ground settlements of about  $15 \pm 5$  cm were observed. The SHA site offers a unique opportunity to validate ground response analysis codes and seismic compression analysis procedures for strong levels of shaking similar to those that would often be applied in seismic design.

A site investigation at the SHA was conducted to obtain soil samples, SPT blowcounts with energy measurements, and a velocity profile. The site profile was found to consist of about 70 m of Quaternary sands overlying Pleistocene and then Tertiary clayey bedrock materials. Triaxial compression and resonant column/torsional shear (RCTS) tests were conducted on sand specimens to measure shear strength and cyclic modulus reduction and damping curves. Simple shear tests were also conducted on remolded sand specimens to develop a material-specific model relating volume change to amplitude and number of shear strain cycles for the unsaturated soils. This testing was performed for relative densities ( $D_R$ ) of 40% and 65%, which spans the range of estimates from Pitcher tube samples and penetration resistance correlations.

Equivalent linear and nonlinear ground response was modeled with DeepSoil 4.0 using the dynamic soil properties developed from field and laboratory testing and ground motion recordings from 100 m depth as input. We have some confidence that 1D modeling of site response, which is an underlying assumption of DeepSoil, due to relatively consistent surface-to-bedrock transfer functions from recorded data that are reasonably well predicted from 1D analysis of SH waves.

Initial ground response analyses utilizing soil dynamic properties derived from RCTS tests encounter several difficulties including overestimation of high frequency ground response and unrealistic strain localization at a depth of 50 m from main shock ground motions. Increases



in the small strain material damping from laboratory-based values (generally near  $D_{min} = 1\%$ ) to higher levels of  $D_{min} = 2$  and  $5\%$  largely solve the problem of over-prediction of high frequency ground response. Such increases in small strain damping are consistent with previous vertical array studies in which observed soil damping levels exceed those from laboratory testing. A procedure to adjust backbone curves to approach the shear strength at large strains while retaining low-strain behavior from traditional modulus reduction curves was implemented to address the strain localization problem.

When the modified soil properties are implemented in ground response analysis, the strain localization problem is eliminated and strain demands are increased in shallower parts of the profile. At a small strain damping level (in soil layers) of  $D_{min} = 5\%$ , the ground motion predictions from both equivalent linear (EQL) and nonlinear (NL) analyses provide generally good matches to recorded response spectra from aftershock and main shock recordings at 2.4 and 50 m depths. The EQL and NL results are practically identical for the relatively low-strain aftershock site response (peak shear strains in profile of  $\gamma \sim 0.12$  and  $0.02\%$ ). For the relatively strong main shock recordings, the EQL analyses over-damp the ground motions producing a characteristic flat spectral shape at short periods ( $T < \sim 0.1$  sec) that is not present in NL analysis results or in the data. For the same reason (overdamping), the EQL waveforms lack realistic phasing outside of the main shear wave window. Despite these problems, at intermediate and long spectral periods ( $T > \sim 0.1$  sec), the EQL and NL results are similar, with both providing good matches to recorded data.

Ground failure analyses for the site indicate that liquefaction was unlikely to have occurred. Near the ground surface the soils are unsaturated and hence not susceptible. At depths beyond 50 m the soils are saturated but cyclic demands are shown to fall below the anticipated cyclic resistance. Accordingly, ground settlements appear to have resulted from seismic compression of partially saturated soils. Shear strains estimated from the NL ground response analysis were combined with a material-specific volumetric strain material model that predicts vertical strains given shear strain amplitude, number of cycles, and vertical total stress. Settlements were computed using vertical strains evaluated independently for both horizontal directions. Drawing on test results showing that vertical strains from the two horizontal directions can be summed to evaluate the vertical strain from simultaneous 2D strain demands, the two settlement estimates are summed to provide estimates of site-specific ground surface

settlements from horizontal ground shaking ranging from approximately 8 to 12 cm for relative densities of 65% and 40%, respectively. When vertical ground motions are considered, these estimates are increased by 50%, leading to estimated settlements ranging from 12 to 18 cm. These estimates compare reasonably well to the observed settlements of  $15 \pm 5$  cm at the SHA site.

## REFERENCES

- Abou-Matar, H. and Goble G. G. (1997). "SPT dynamic analysis and measurements," *J. Geotech. & Geoenviron. Engrg.*, ASCE 123(10), 921-928.
- Anderson, D. G., and Tang, Y. K. (1989). "Summary of soil characterization program for the lotung large-scale seismic experiment," *NP-6154*, Electric Power Research Institute, Palo Alto, Calif.
- Baise, L.G., Thompson, E.M., Kaklamanos, J., and Dorfmann, L. (2011). "Complex site response: does one dimensional site response work?" *Proc. 4<sup>th</sup> IASPEI/IAEE International Symposium*, Univ. of California, Santa Barbara.
- Boore, D.M. (2005). "On pads and filters: processing strong-motion data," *Bull. Seism. Soc. Am.*, 95(2), 745-750.
- Boore, D.M. and Bommer, J.J. (2005). "Processing of strong-motion accelerograms: needs, options and consequences," *Soil Dyn. Earthquake Engrg.*, 25(2), 93-115.
- Boulanger, R.W. (2003). "High overburden stress effects in liquefaction analysis," *J. Geotech. & Geoenviron. Engrg.*, ASCE 129(12), 1071-1082.
- Bozorgnia, Y. and Campbell, K.W. (2004). "The vertical-to-horizontal response spectral ratio and tentative procedures for developing simplified V/H and vertical design spectra," *J. Earthquake Engrg.*, 8(2), 175-207.
- Cubrinovski, M. and Ishihara, K. (1999). "Empirical correlation between SPT N-value and relative density for sandy soils," *Soils and Foundations*, 39(5), 61-71.
- Cubrinovski, M., Ishihara, K., and Tanizawa, F. (1996). "Numerical simulation of the Kobe port island liquefaction," *Proc. 11th World Conf. on Earthquake Engrg*, Paper No. 330.
- Darendeli, M. (2001). "Development of a new family of normalized modulus reduction and material damping curves," *Ph.D. Dissertation*, Dept. of Civil Eng., Univ. of Texas, Austin.
- Dobry, R. and Ladd, R.S. (1980). Discussion to "Soil liquefaction and cyclic mobility evaluation for level ground during earthquakes," *J. of Geotech. Engrg. Div.*, ASCE, 106(GT6), 720-724.
- Duku, P.M., Stewart, J.P., Whang, D.H., Venugopal, R. (2007). "Digitally controlled simple shear apparatus for dynamic soil testing," *Geotech. Testing Journal*, ASTM, 30 (5), 368-377.
- Duku, P.M., Stewart, J.P., Whang, D.H., and Yee, E. (2008). "Volumetric strains of clean sands subject to cyclic loads," *J. of Geotech. & Geoenviron. Engrg.*, ASCE, 134 (8), 1073-1085.
- Elgamal, A., Lai, T., Yang, Z., and He, L. (2001). "Dynamic soil properties, seismic downhole arrays and applications in practice," *Proc., 4th Int. Conf. on Recent Advances in Geotechnical Earthquake Engineering and Soil Dynamics*, Univ. of Missouri-Rolla, San Diego.
- Hardin, BO and VP Drnevich (1972). "Shear modulus and damping in soils," *J. Soil Mech. & Found. Div.*, ASCE, 98 (7), 667-692.
- Hashash, Y.M.A., Groholski, D.R., Phillips, C.A., Park, D., and Musgrove, M. (2011). "Deepsoil v4.0, user manual and tutorial," 98p.
- Hatanaka, M. and Uchida A. (1996). "Empirical correlation between penetration resistance and internal friction angle of sandy soils," *Soils and Foundation*, 48(4), 1-9.
- Idriss, I.M. and Boulanger, R.W. (2008). Soil liquefaction during earthquakes. *Monograph MNO-12*, Earthquake Engineering Research Institute, Oakland, CA, 261 pp.
- Idriss, I.M. and Sun, J.I. (1992). "Shake91: a computer program for conducting equivalent linear seismic response analyses of horizontally layered soil deposits," *Users Guide*, Univ. of Calif., Davis, 13pp.
- Kayen, R., Brandenberg, S.J., Collins, B.D., Dickenson, S., Ashford, S., Kawamata, Y., Tanaka, Y., Koumoto, H., Abrahamson, N., Cluff, L., Tokimatsu, K. (2009). "Geoengineering and seismological aspects of the niigata-ken chuetsu-oki earthquake of 16 July 2007," *Earthquake Spectra*, 25(4), 777-802.

- Kramer, S.L. (1996). *“Geotechnical earthquake engineering,”* Prentice Hall, New Jersey, 653pp.
- Kwok, A.O., Stewart, J.P., and Hashash, Y.M.A. (2008). “Nonlinear ground response analysis of Turkey Flat shallow stiff soil site to strong ground motion,” *Bull. Seism. Soc. Am.*, 98(1), 331-343.
- Kwok, A.O., Stewart, J.P., Hashash, Y.M.A., Matasovic, N., Pyke, R., Wang, Z., and Yang, Z. (2007). “Use of exact solutions of wave propagation problems to guide implementation of nonlinear seismic ground response analysis procedures,” *J. Geotech. & Geoenviron. Engrg.*, ASCE, 133 (11), 1385-1398.
- Liu, A.H., Stewart, J.P., Abrahamson, N.A., and Moriwaki, Y. (2001). “Equivalent number of uniform stress cycles for soil liquefaction analysis,” *J. Geotech. & Geoenviron. Engrg.*, ASCE, 127(12), 1017-1026.
- Menq, F.Y. (2003). “Dynamic properties of sandy and gravelly soils.” *Ph.D. Dissertation*, Dept. of Civil Eng., Univ. of Texas, Austin.
- Mikami, A., Stewart, J.P., and Kamiyama, M. (2008). “Effects of time series analysis protocols on transfer functions calculated from earthquake accelerograms,” *Soil Dyn. Earthquake Engrg.*, 28 (9), 695-706.
- Miyake, H., Koketsu, K., Hikima, K., Shinohara, M., and Kanazawa, T. (2010). “Source fault of the 2007 Chuetsu-oki, Japan, earthquake,” *Bull. Seism. Soc. Am.*, 100(1), 384-391.
- National Research Council (NRC). (1985). “Committee on Earthquake Engineering, Commission on Engineering and Technical Systems.” *Liquefaction of soils during earthquakes*, National Academy Press, Washington D.C..
- Nigbor, R.L. and Imai, T. (1994). “The suspension ps velocity logging method,” *Geophysical Characterization of Sites*, ISSMFE Special Publication TC 10, XIII ICSMFE, New Delhi, India, Richard Woods, Editor, 57-61.
- Polito, C. P. and Martin, J. R. (2001). “Effects of nonplastic fines on the liquefaction resistance of sands.” *J. Geotech. & Geoenviron. Engrg.*, 127(5), 408-415.
- Pyke, R., Seed, H.B., Chan, C.K. (1975). “Settlement of sands under multidirectional shaking,” *J. Geotech. Engrg.*, ASCE, 101 (4), 379-398.
- Sakai, T., Suehiro, T., Tani, T., and Sato, H. (2009). “Geotechnical performance of the Kashiwazaki-Kariwa nuclear power station caused by the 2007 Niigata ken Chuetsu-oki earthquake” *Earthquake geotechnical case histories for performance-based design*, Taylor & Francis Group, London, Kokusho (ed).
- Seed, H.B. and Idriss, I.M. (1971). “Simplified procedure for evaluating soil liquefaction potential,” *J. Soil Mech. & Found. Div.*, ASCE, 97(9), 1249-1273.
- Seed, H.B., Mori, K., and Chan, C.K. (1977). “Influence of seismic history on liquefaction of sands,” *J. Geotech. Engrg. Div.*, ASCE, 103(GT4), 246-270.
- Shahi, S.K. and Baker, J.W. (2011). “An empirically calibrated framework for including the effects of near-fault directivity in probabilistic seismic hazard analysis,” *Bull. Seism. Soc. Am.*, 101, (2), 742-755.
- Skempton, A.W. (1986). “Standard penetration test procedures and the effects in sands of overburden pressure, relative density, particle size, aging, and overconsolidation,” *Geotechnique*, 36(3), 425-447.
- Stewart, J.P. and Kwok, A.O. (2008). “Nonlinear seismic ground response analysis: code usage protocols and verification against vertical array data,” *Geotechnical Engineering and Soil Dynamics IV*, May 18-22, 2008, Sacramento, CA, *ASCE Geotechnical Special Publication No. 181*, D. Zeng, M.T. Manzari, and D.R. Hiltunen (eds.), 24 pages (electronic file).
- Stewart J.P., Smith P.M., Whang D.H., and Bray J.D. (2004). “Seismic compression of two compacted earth fills shaken by the 1994 Northridge earthquake,” *J. Geotech. & Geoenviron. Engrg.*, ASCE, 130(5), 461-476.
- Stewart, J.P., Smith, P.M., Whang, D.H., and Bray, J.D. (2002). “Documentation and analysis of field case histories of seismic compression during the 1994 Northridge, California, earthquake,” *Rpt. No. PEER-2002/09*, Pacific Earthquake Engineering Research Center, U.C. Berkeley, Calif.
- Stewart, J.P., Kwok, A.O., Hashash, Y.M.A., Matasovic, N., Pyke, R., Wang, Z., and Yang, Z. (2008). “Benchmarking of nonlinear seismic ground response analysis procedures,” *Rpt. No. PEER-2008/04*, Pacific Earthquake Engineering Research Center, U.C. Berkeley, Calif.

- The Tokyo Electric Power Company, Inc. (2007). "The data analysis recorded at the Kashiwazaki Kariwa Nuclear Power Plant during the 2007 Niigata-ken Chuetsu-oki earthquake", [http://www.tepco.co.jp/cc/press/betu07\\_j/images/070730d.pdf](http://www.tepco.co.jp/cc/press/betu07_j/images/070730d.pdf).
- Tokimatsu, K. (2008). "Geotechnical problems in the 2007 Niigata-ken Chuetsu-oki earthquake," *Geotechnical Engineering and Soil Dynamics IV*, May 18-22, 2008, Sacramento, CA, *ASCE Geotechnical Special Publication No. 181*, D. Zeng, M.T. Manzari, and D.R. Hiltunen (eds.), 30 pages (electronic file).
- Tokimatsu, K. and Arai, H. (2008). "Dynamic soil behavior and rock outcrop motion back-calculated from downhole array records at kashiwazaki-kariwa nuclear power plant in the 2007 niigata-ken chuetsu-oki earthquakes," *Proc. 5th Int. Conf. on Urban Earthquake Eng.*, Tokyo, Japan, Mar. 4-5, 2008, 289-294.
- Tokimatsu, K. and Seed, H.B. (1987). "Evaluation of settlements in sand due to earthquake shaking," *J. of Geotech. Engrg.*, ASCE, 113(8), 861-878.
- Tokimatsu, K. and Yoshimi, Y. (1983). "Empirical correlation of soil liquefaction based on SPT N-value and fines content," *Soils and Foundations*, 23(4), 56-74.
- Tokimatsu, K., Ibaraki, Y., and Arai, H. (2009). "Dynamic soil properties back-calculated from strong motions recorded at two downhole arrays during the 2007 Niigata-ken Chuetsu-oki earthquakes," *Proc. 6th Int. Conf. on Urban Earthquake Eng.*, Tokyo, Japan, Mar. 3-4, 2009, 485-489.
- Tokyo Soil Research (2009). "Tokyo electric power Kashiwazaki-Kariwa nuclear power plant service hall geotechnical investigation," *Rpt. by Tokyo Soil Research*, 66pp.
- Tsai, C.C. and Hashash, Y.M.A. (2009). "Learning of dynamic soil behavior from downhole arrays," *J. Geotech. & Geoenviron. Engrg.*, ASCE, 135(6), 745-757.
- Wartman, J., Rodriguez-Marek, A., Repetto, P.C., Keefer, D.K., Rondinel, E. Zegarra-Pellane, J., and Baures, D. (2003). "Ground failure" *Earthquake Spectra*, 19(S1), 35-56.
- Wartman, J., Rodriguez-Marek, A., Macari, E. J., Deaton, S., Ramirez-Reynaga, M., Navarro-Ochoa, C, Callan, S., Keefer, D., Repetto, P., and Ovando-Shelley, E. (2005). "Geotechnical aspects of the January 2003 Tecoman earthquake," *Earthquake Spectra*, Vol. 21(2), 493-538.
- Yee, E., Stewart, J.P., and Schoenberg, F.P. (2011). "Characterization and utilization of noisy displacement signals from simple shear device using linear and kernel regression methods," *Soil Dyn. Earthquake Engrg.*, 31(1), 25-32.
- Zeghal, M., Elgamal, A.-W., Tang, H. T., and Stepp, J. C. (1995). "Lotung downhole array. II: Evaluation of soil nonlinear properties," *J. Geotech. Engrg.*, ASCE, 121 (4), 363-378.
- Zhang, J., Andrus, R.D., and Juang, C.H. (2005). "Normalized shear modulus and material damping ratio relationships," *J. Geotech. & Geoenviron. Engrg.*, ASCE, 131 (4), 453-464.

## **Appendix A: Detailed Boring Log (Electronic Supplement)**

## **Appendix B:   Acceleration, Velocity, and Displacement History for Main Shock**

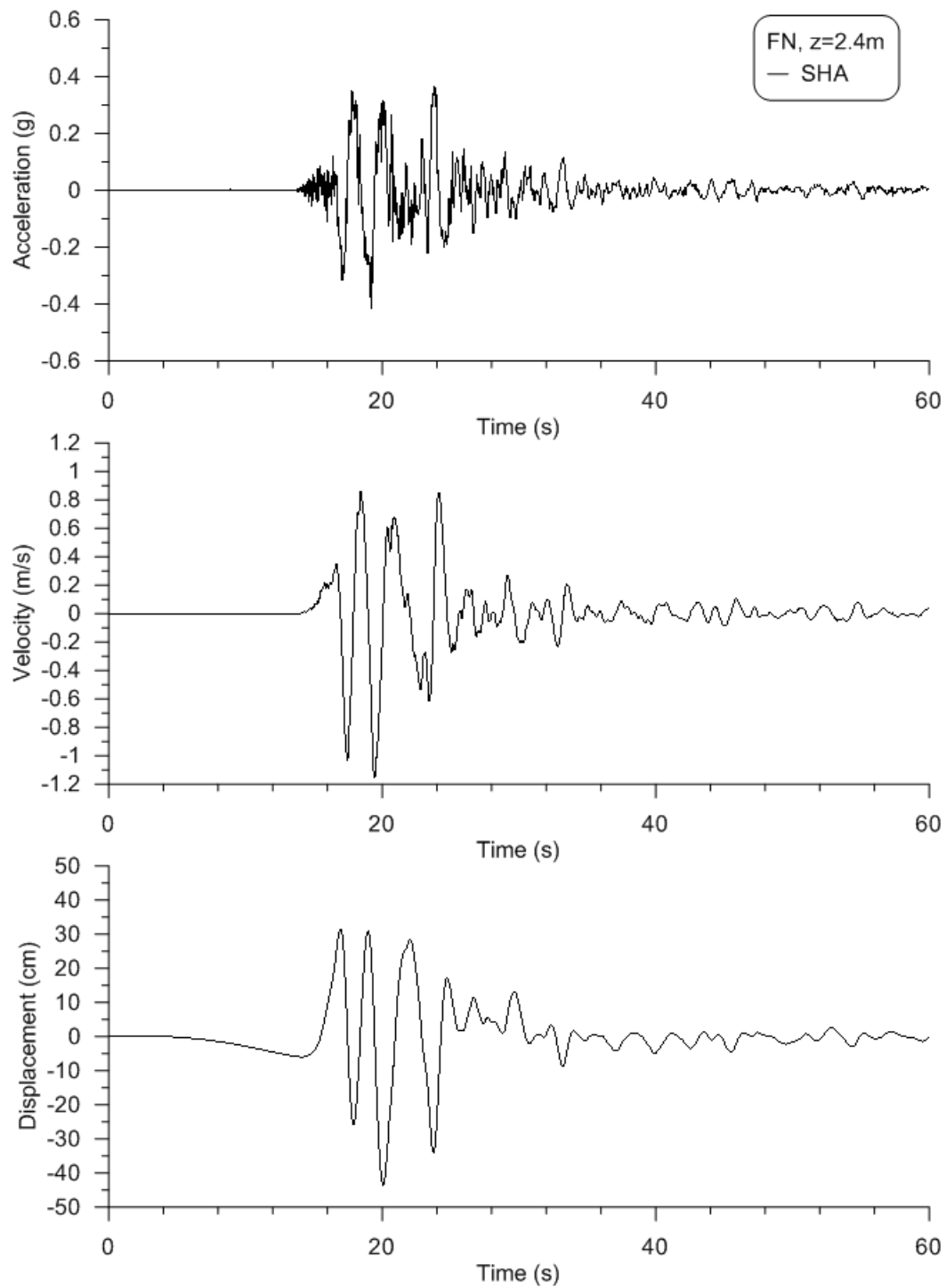


**Figure B1. Corrected acceleration, velocity, and displacement histories for fault normal direction at a depth of 2.4m.**



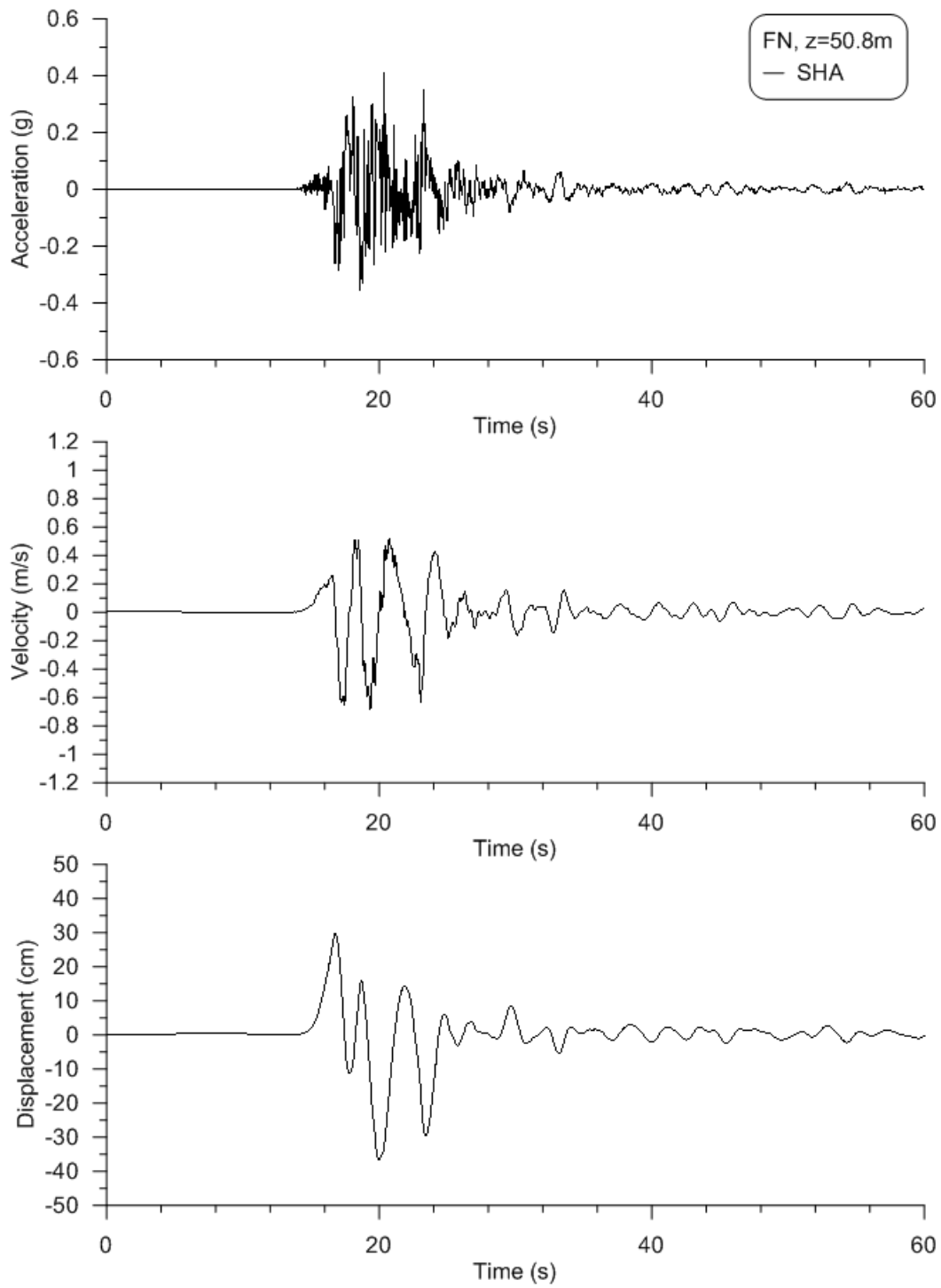


**Figure B2. Corrected acceleration, velocity, and displacement histories for fault normal direction at a depth of 50.8m.**

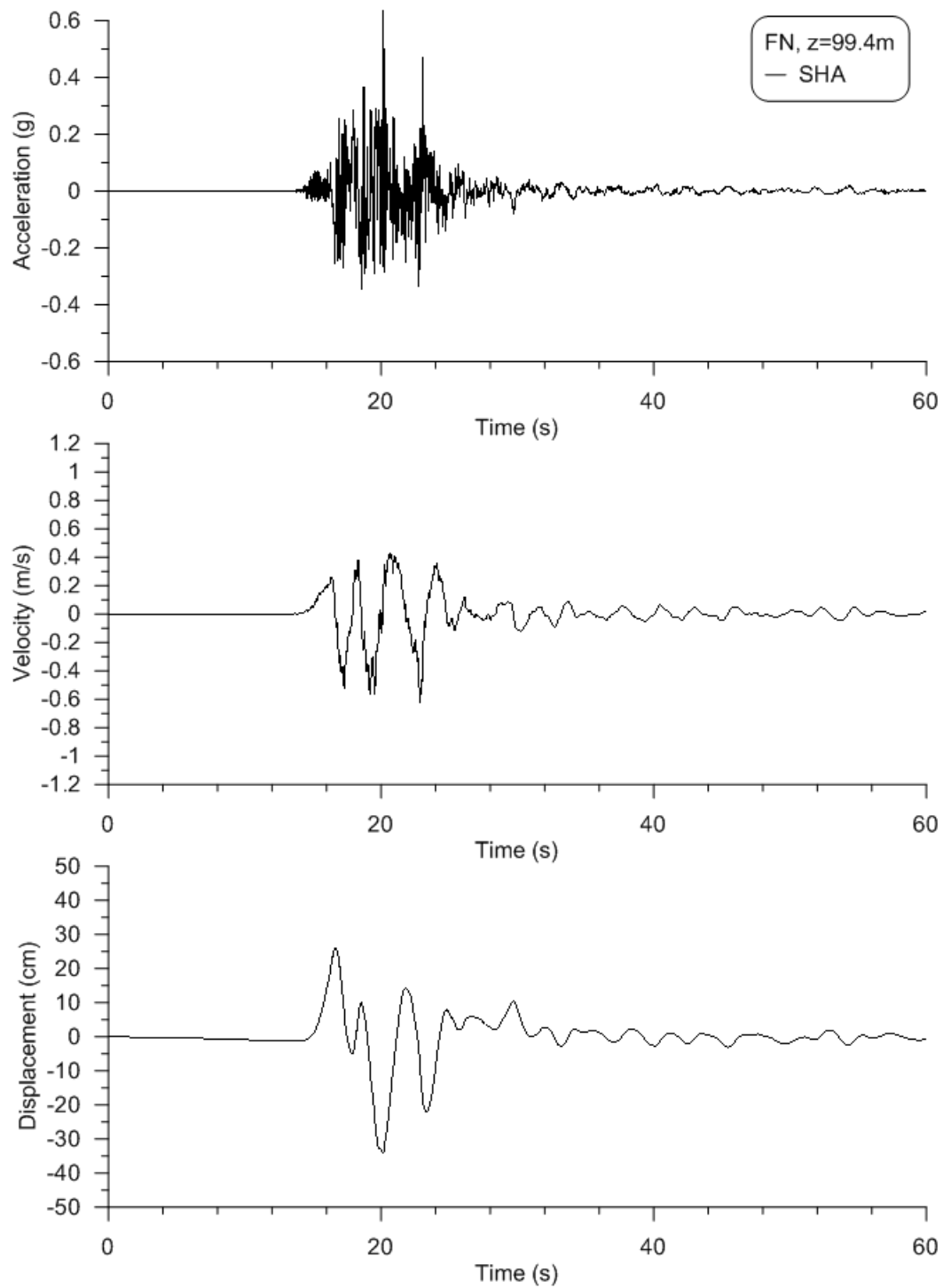


**Figure B3. Corrected acceleration, velocity, and displacement histories for fault normal direction at a depth of 99.4m.**

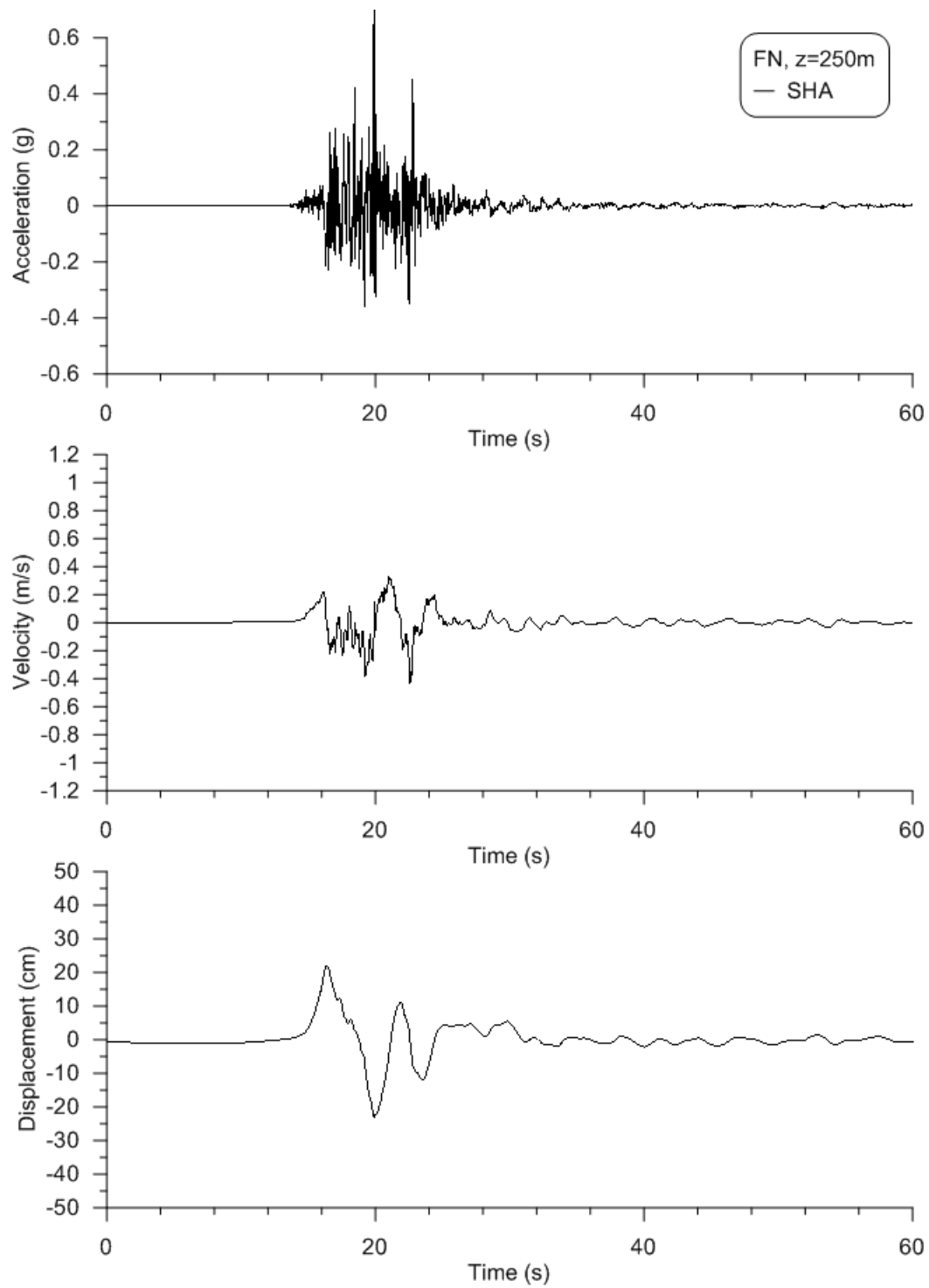


**Figure B4. Corrected acceleration, velocity, and displacement histories for fault normal direction at a depth of 250m.**

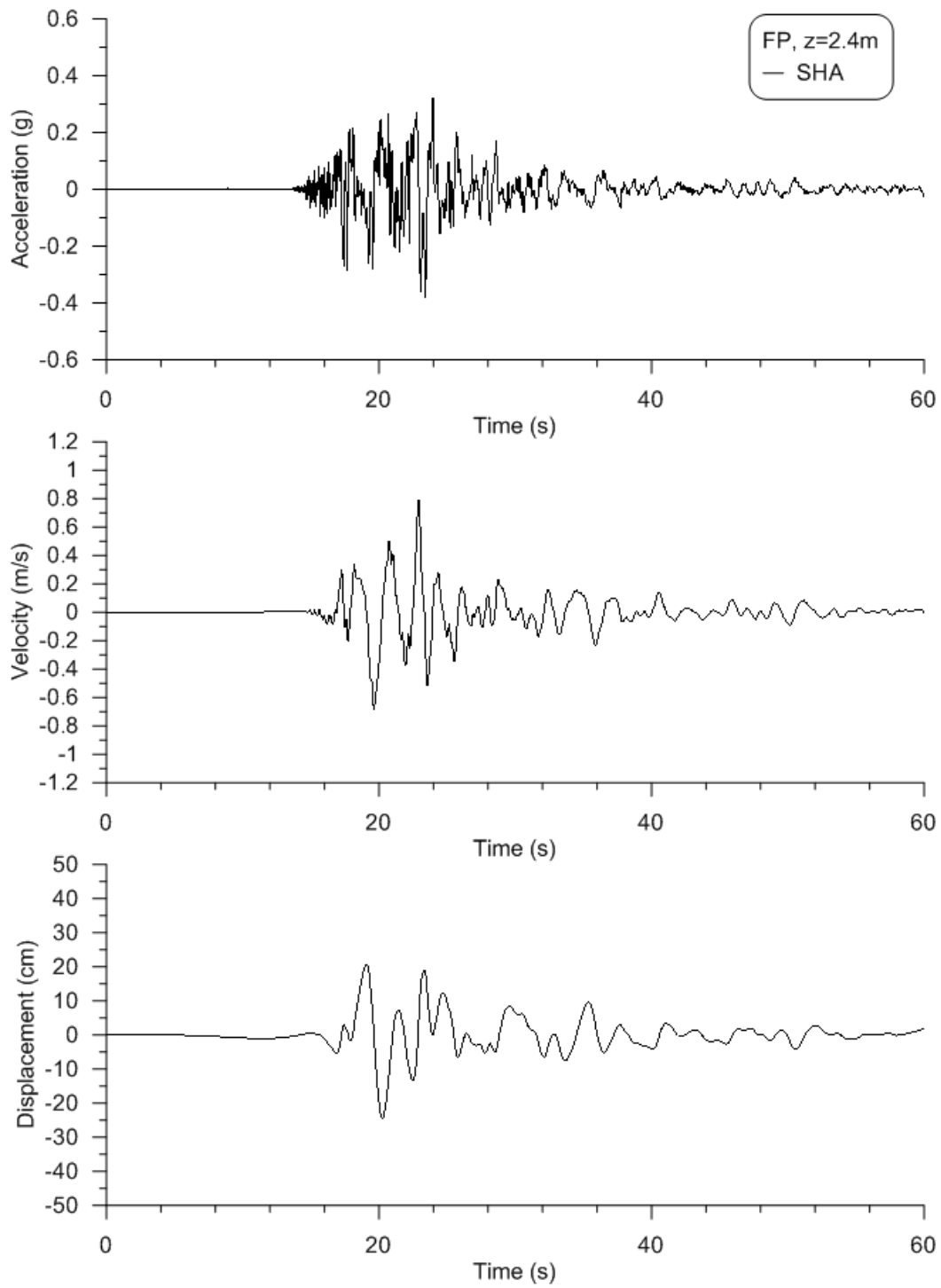


**Figure B5. Corrected acceleration, velocity, and displacement histories for fault parallel direction at a depth of 2.4m.**

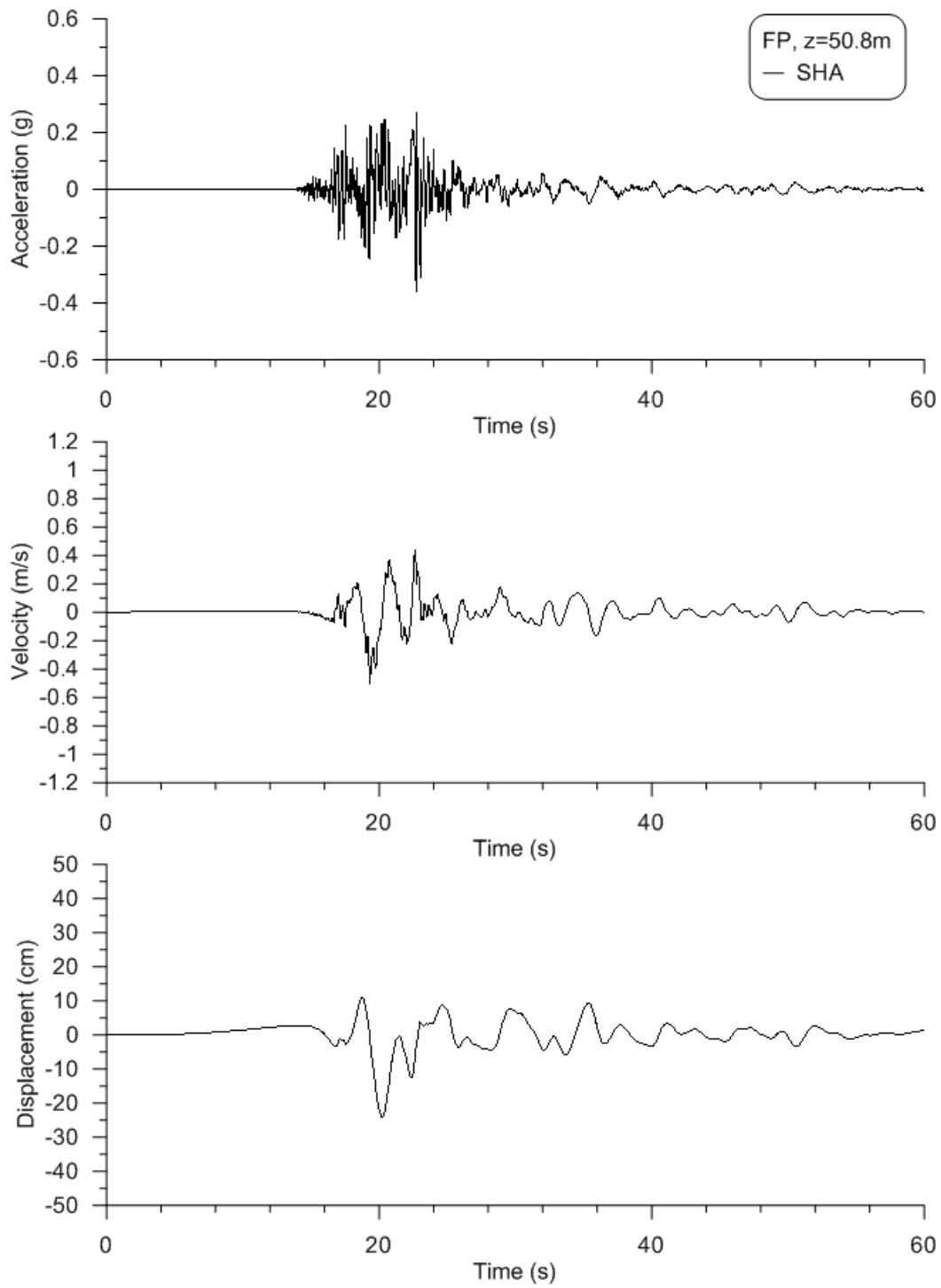


**Figure B6. Corrected acceleration, velocity, and displacement histories for fault parallel direction at a depth of 50.8m.**

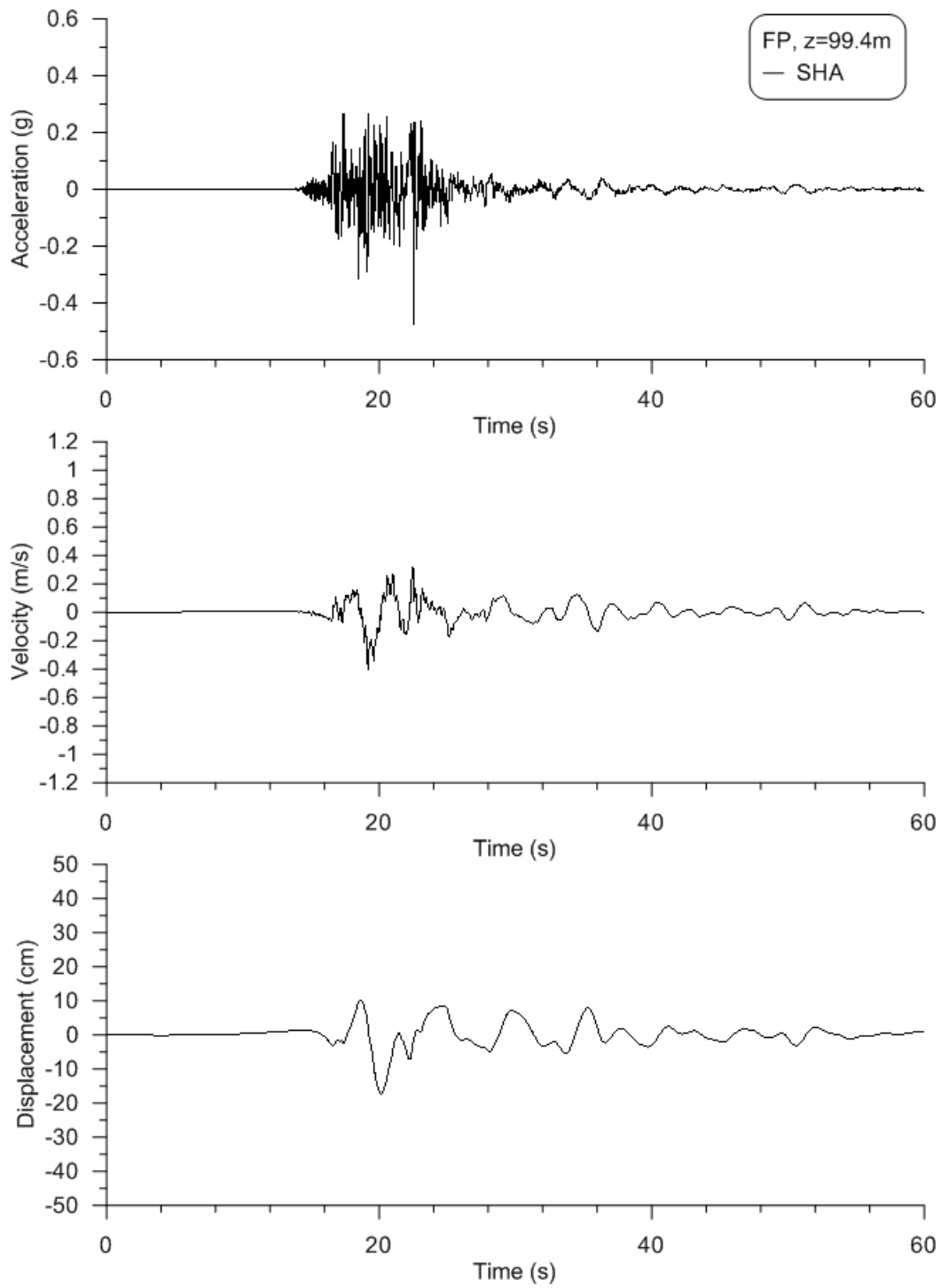


**Figure B7. Corrected acceleration, velocity, and displacement histories for fault parallel direction at a depth of 99.4m.**

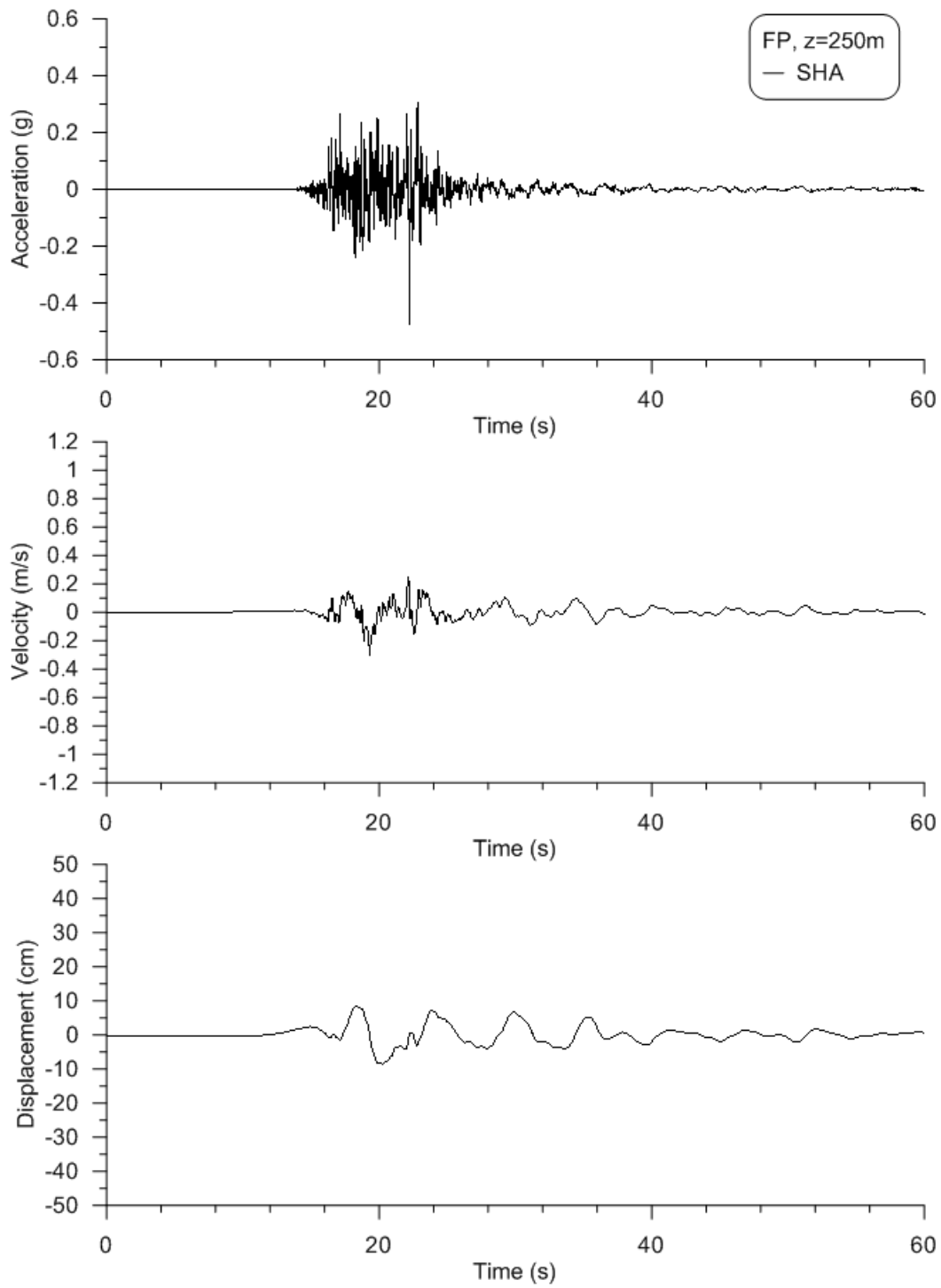


**Figure B8. Corrected acceleration, velocity, and displacement histories for fault parallel direction at a depth of 250m**

## **Appendix C:    Acceleration, Velocity, and Displacement History for Aftershock L**



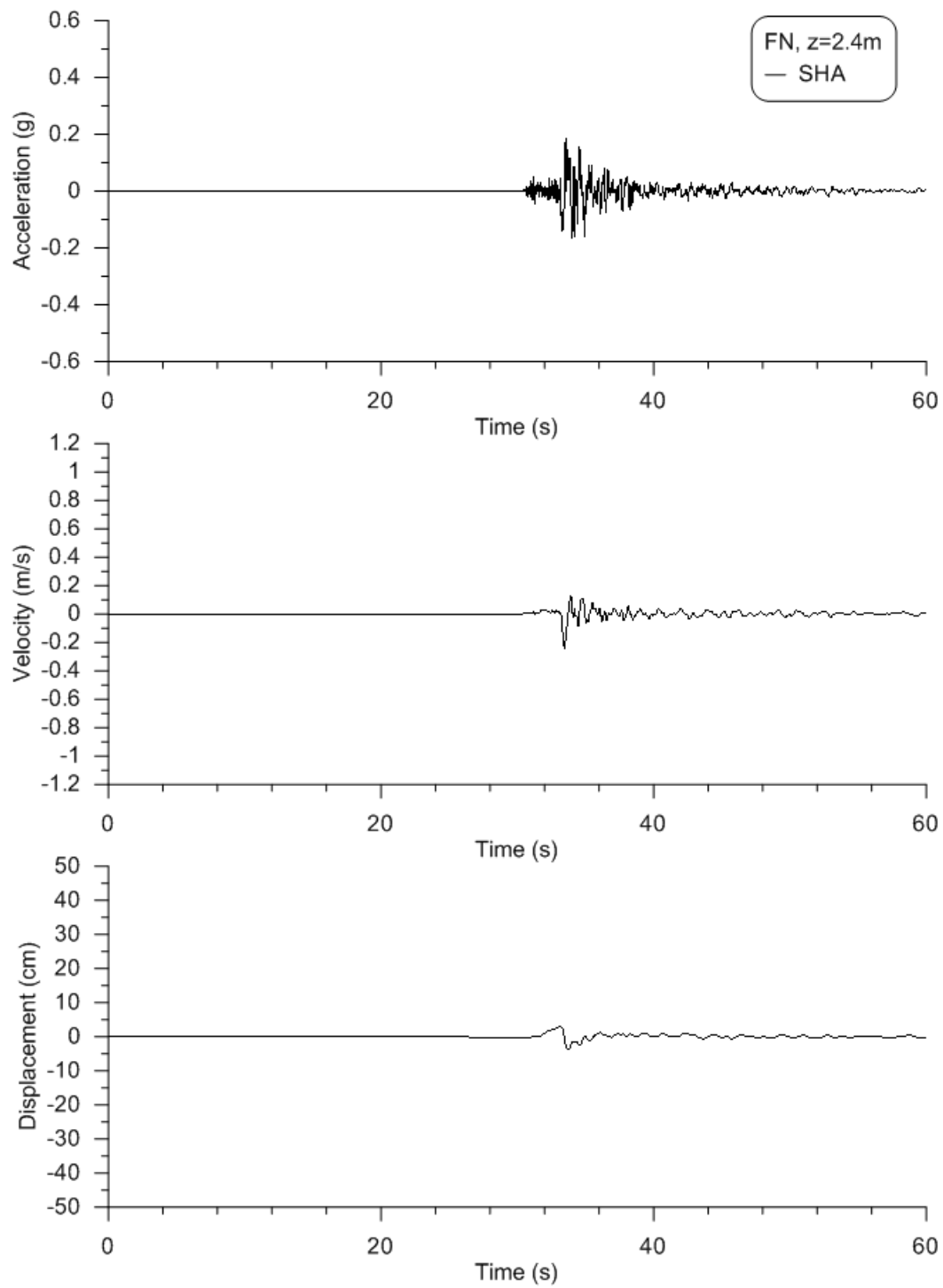


**Figure C!. Corrected acceleration, velocity, and displacement histories for fault normal direction at a depth of 2.4m.**

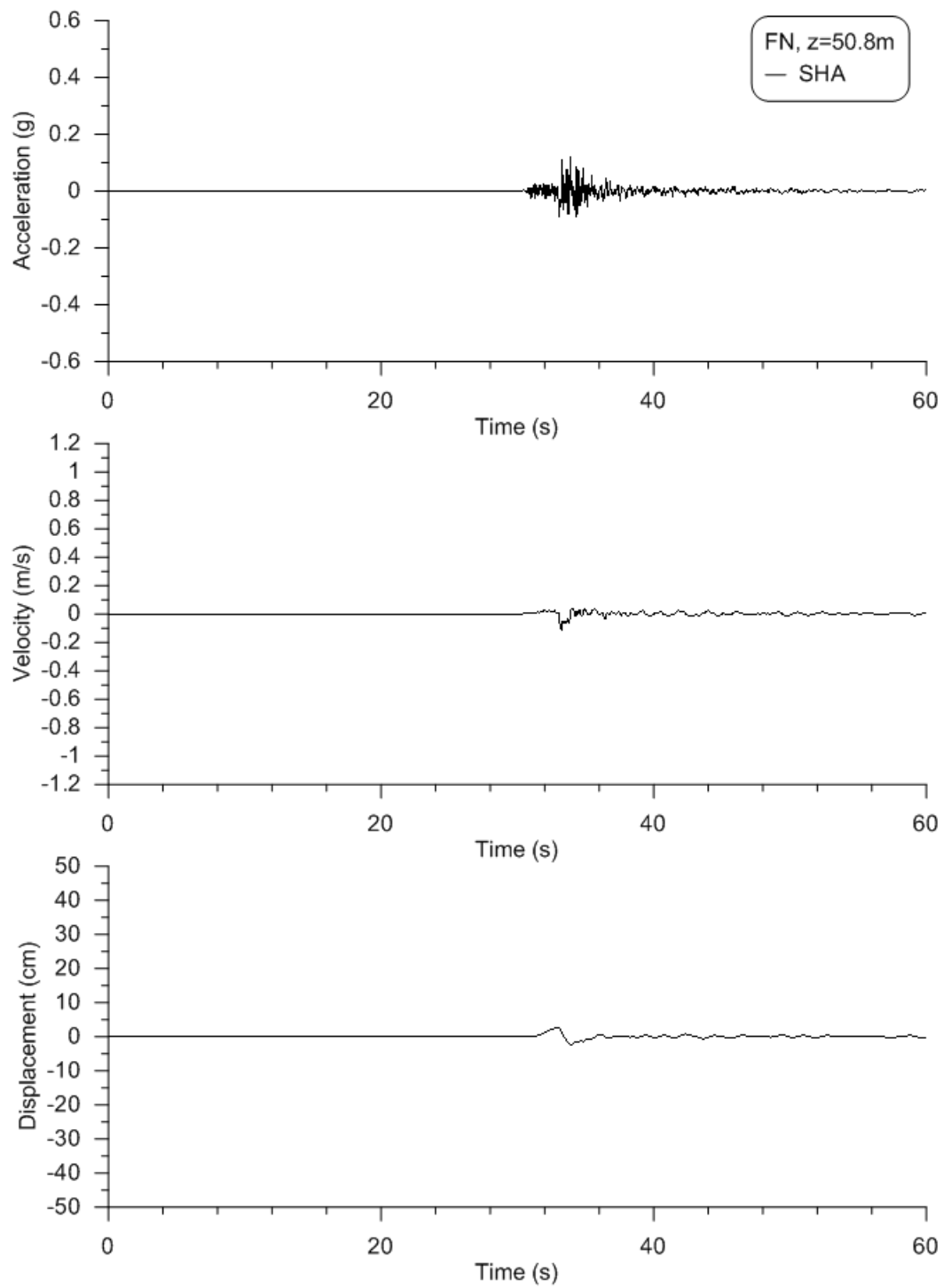


**Figure C2. Corrected acceleration, velocity, and displacement histories for fault normal direction at a depth of 50.8m.**

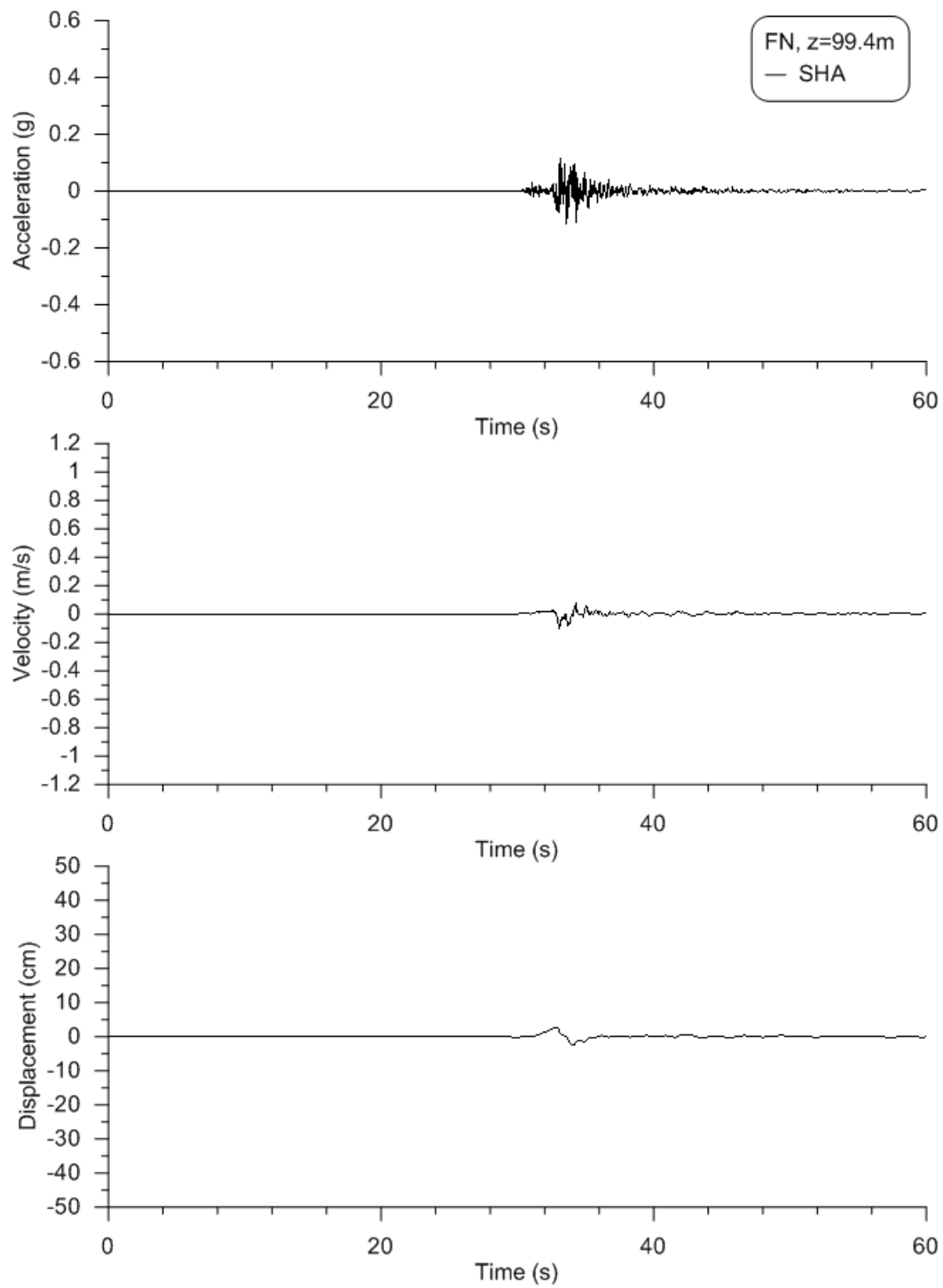


**Figure C3. Corrected acceleration, velocity, and displacement histories for fault normal direction at a depth of 99.4m.**

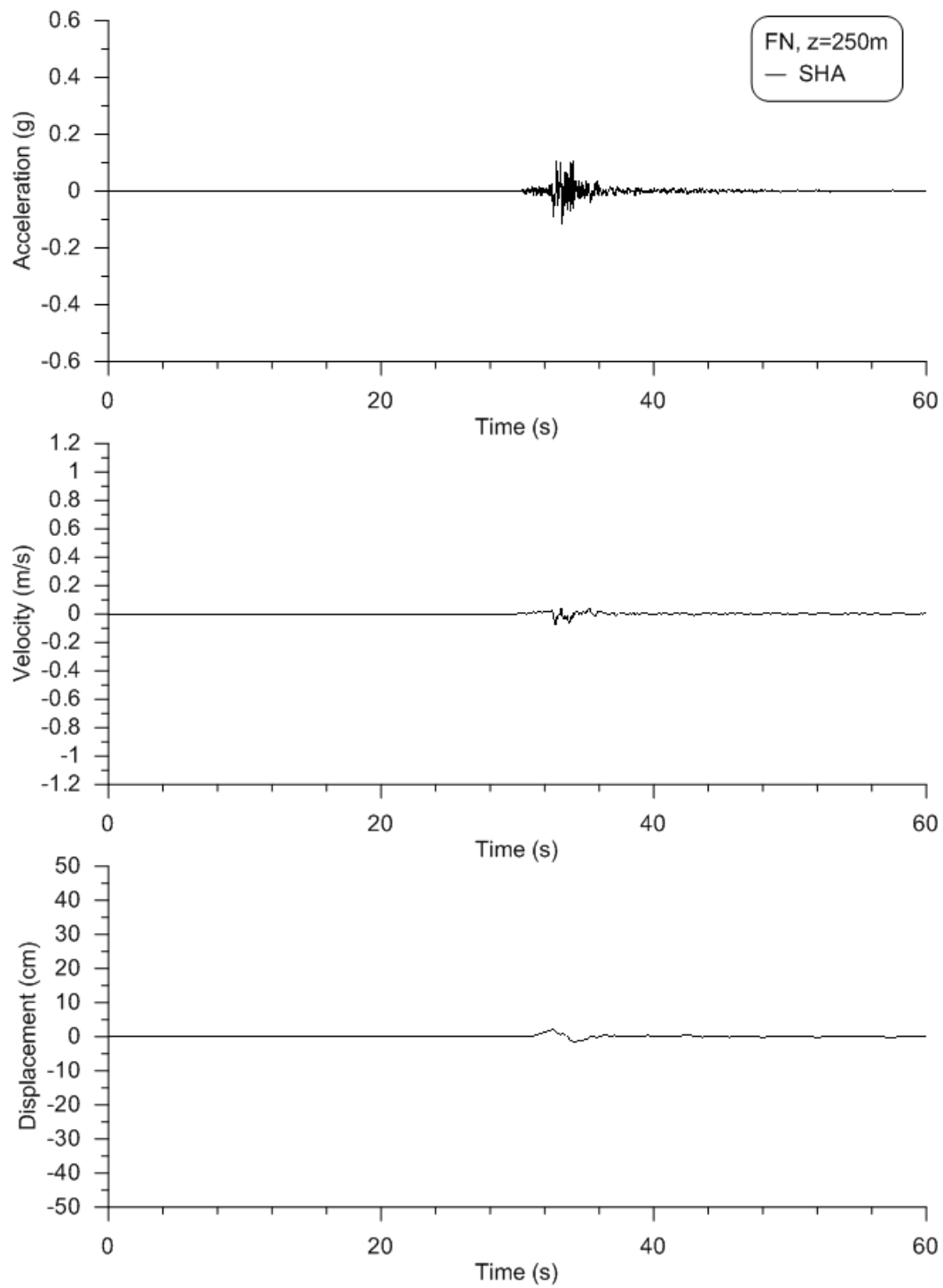


**Figure C4. Corrected acceleration, velocity, and displacement histories for fault normal direction at a depth of 250m.**

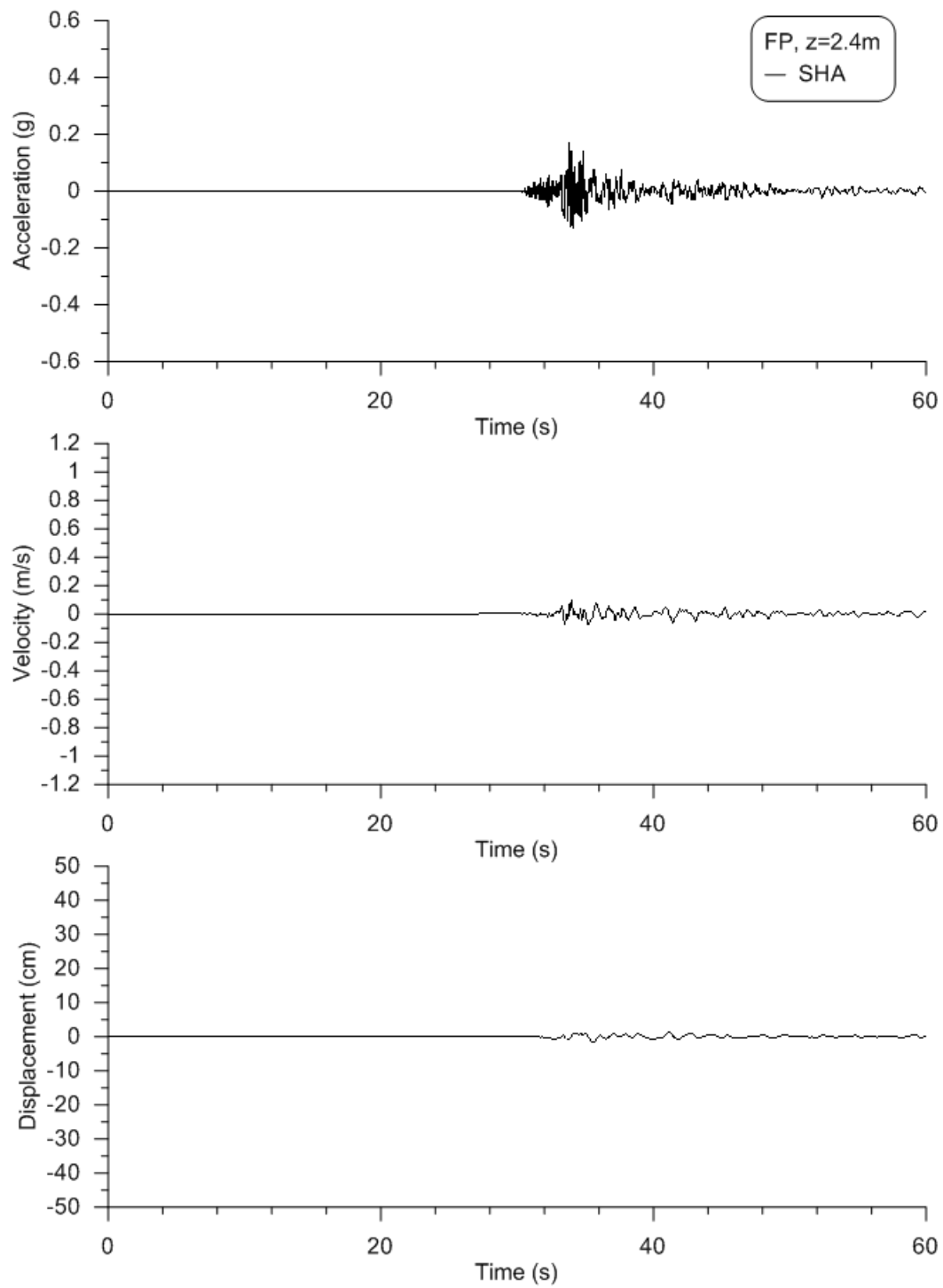


**Figure C5. Corrected acceleration, velocity, and displacement histories for fault parallel direction at a depth of 2.4m.**

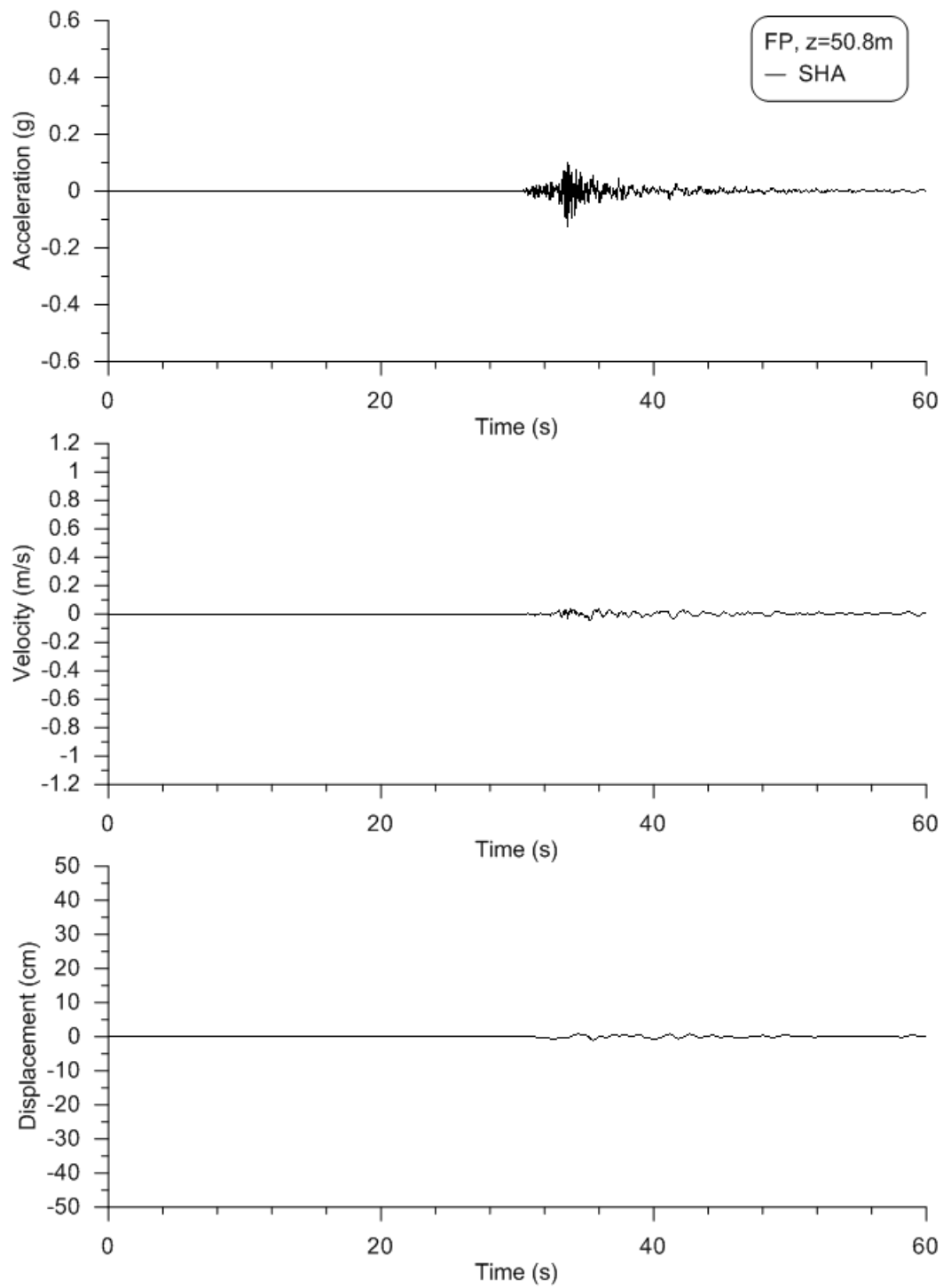


**Figure C6. Corrected acceleration, velocity, and displacement histories for fault parallel direction at a depth of 50.8m.**

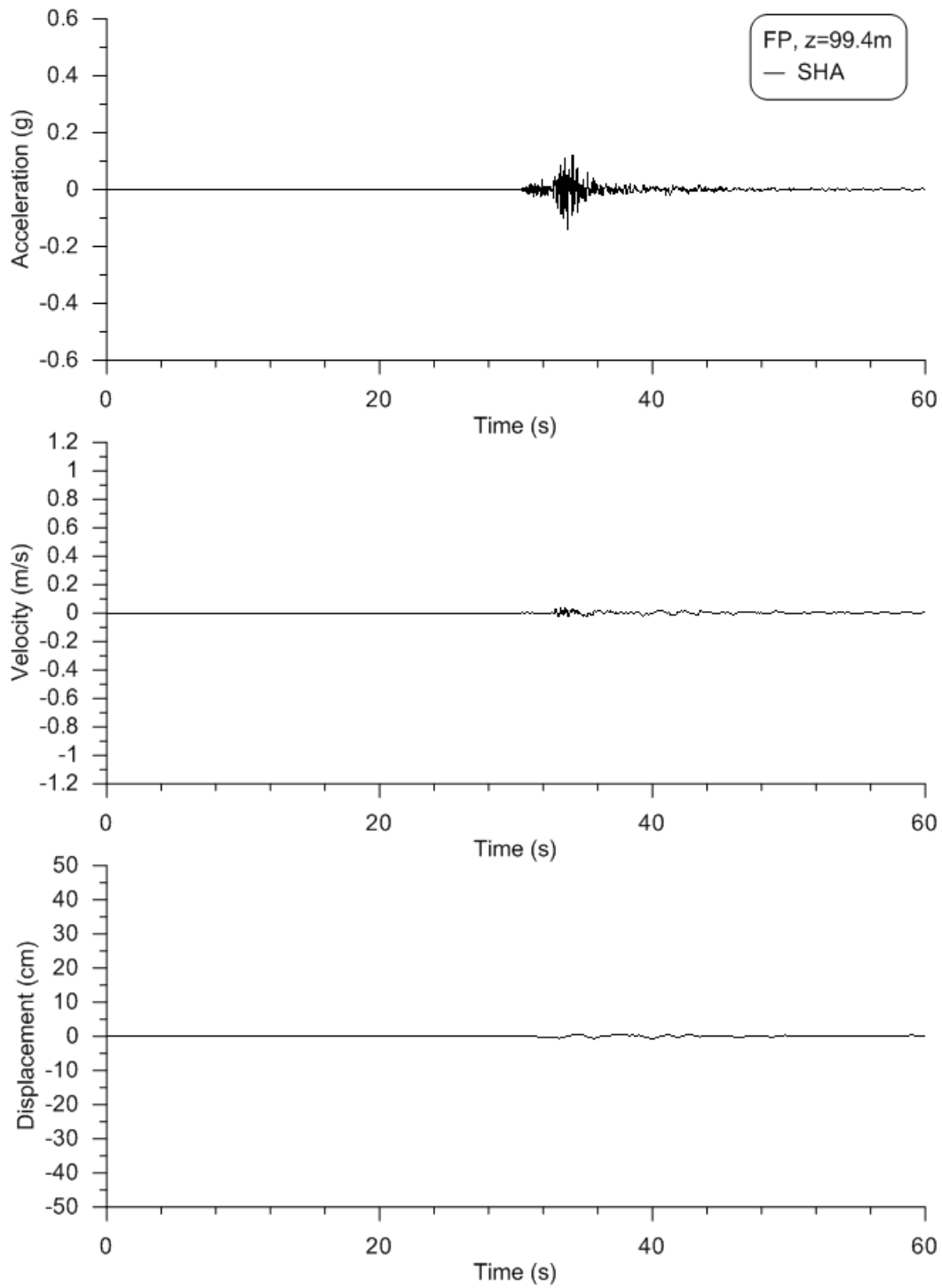


**Figure C7. Corrected acceleration, velocity, and displacement histories for fault parallel direction at a depth of 99.4m.**

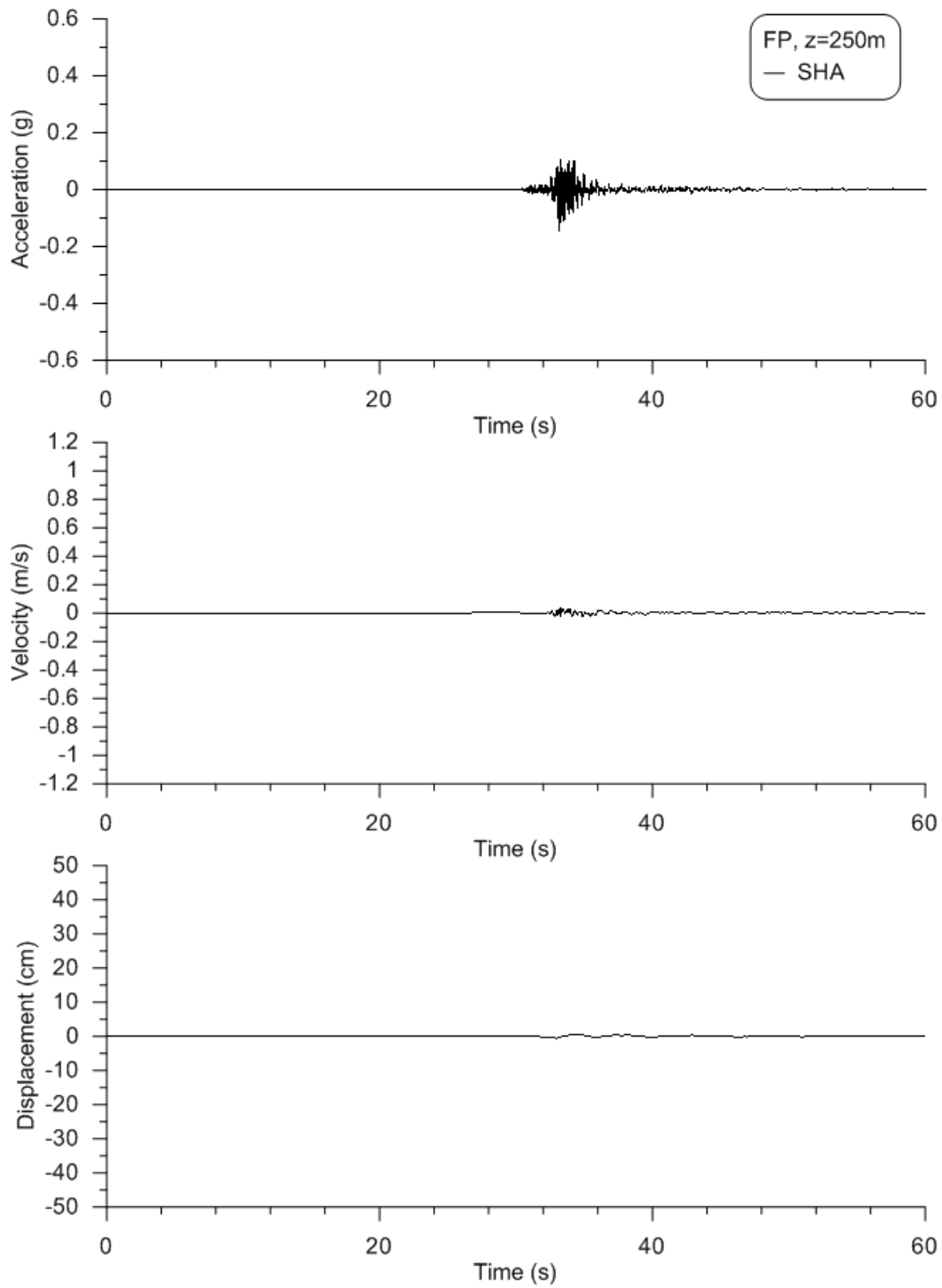


**Figure C8. Corrected acceleration, velocity, and displacement histories for fault parallel direction at a depth of 250m**



## **Appendix D:    Acceleration, Velocity, and Displacement History for Aftershock S**

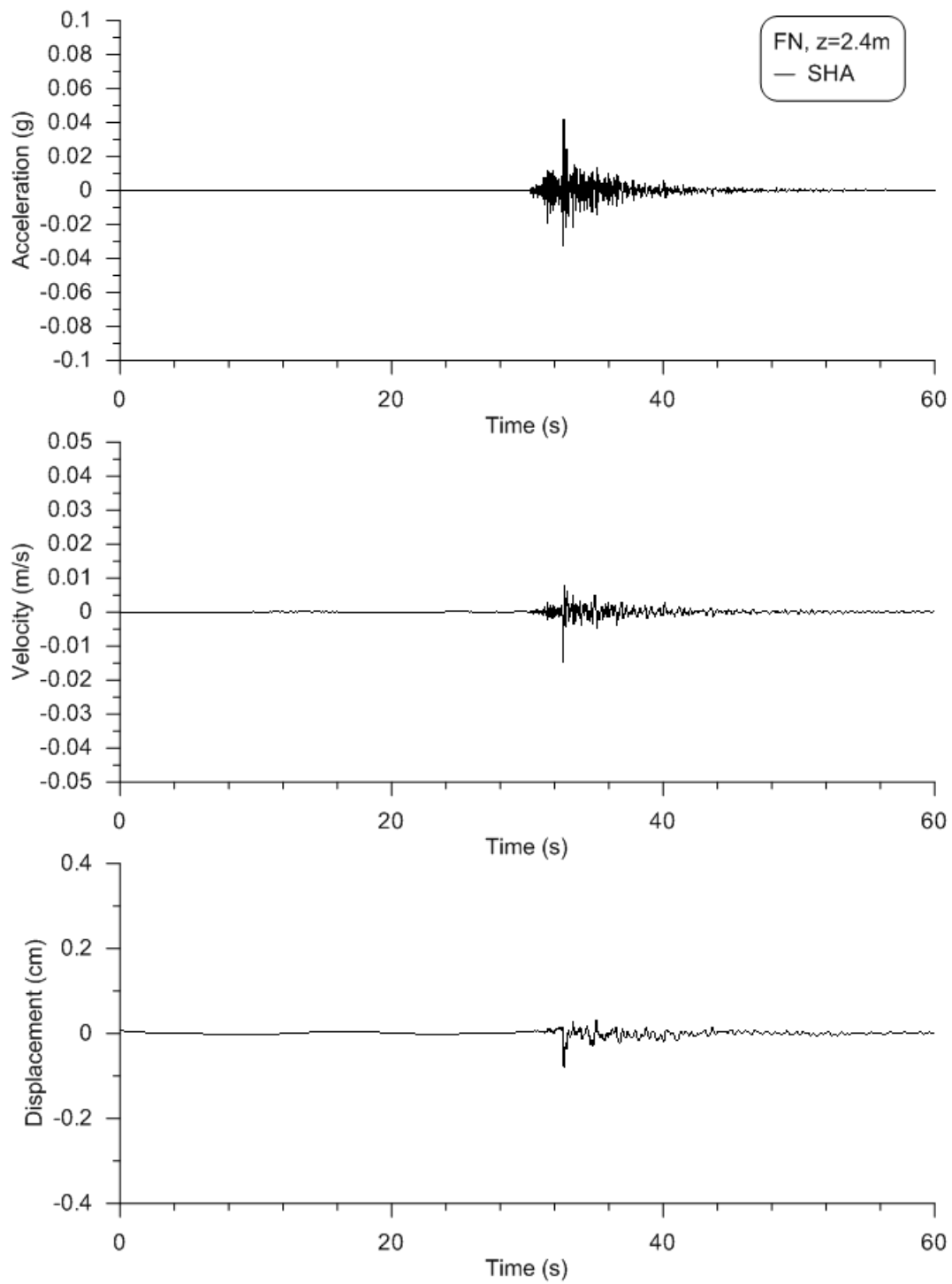


**Figure D1. Corrected acceleration, velocity, and displacement histories for fault normal direction at a depth of 2.4m.**

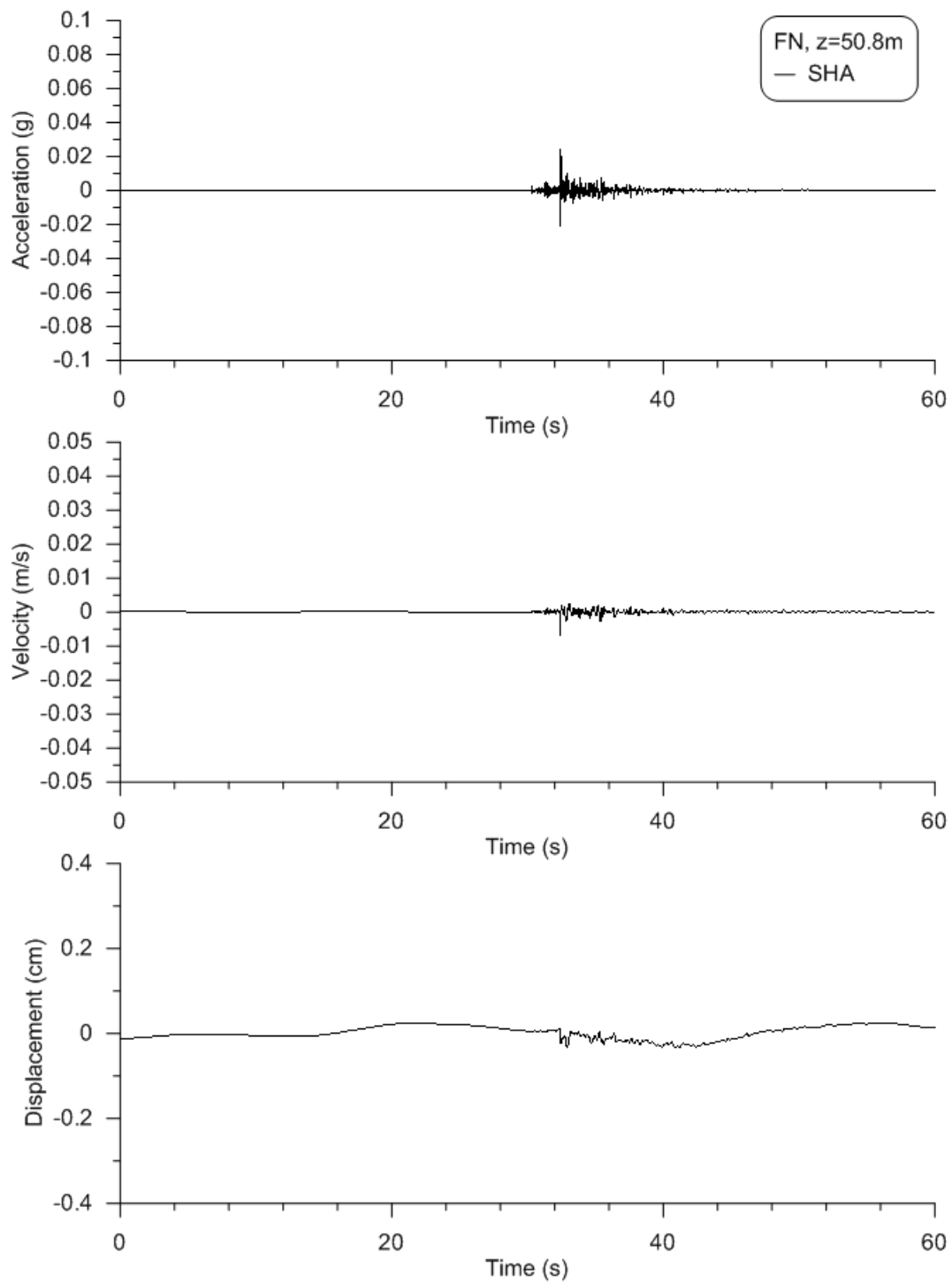


**Figure D2. Corrected acceleration, velocity, and displacement histories for fault normal direction at a depth of 50.8m.**

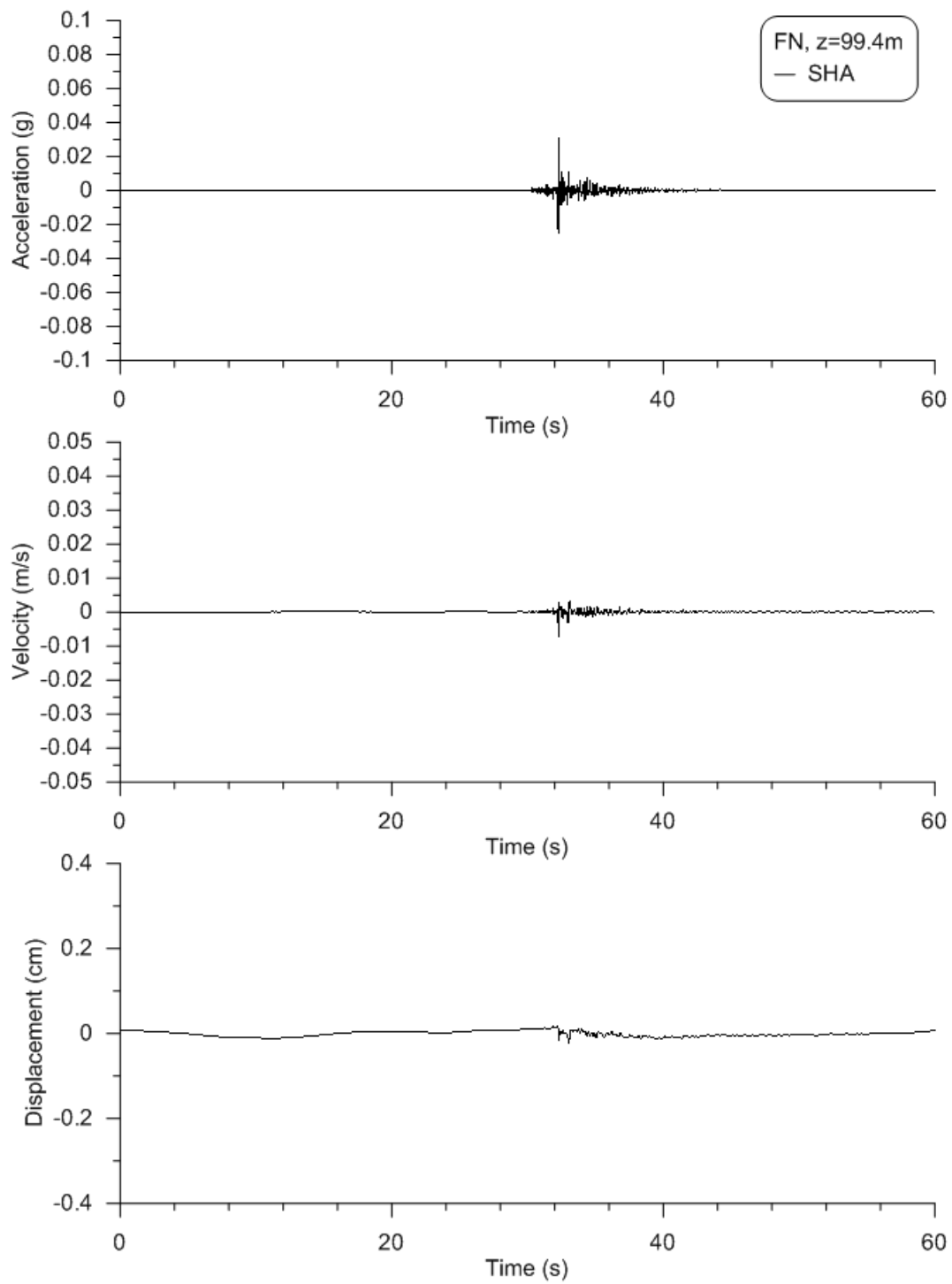


**Figure D3. Corrected acceleration, velocity, and displacement histories for fault normal direction at a depth of 99.4m.**

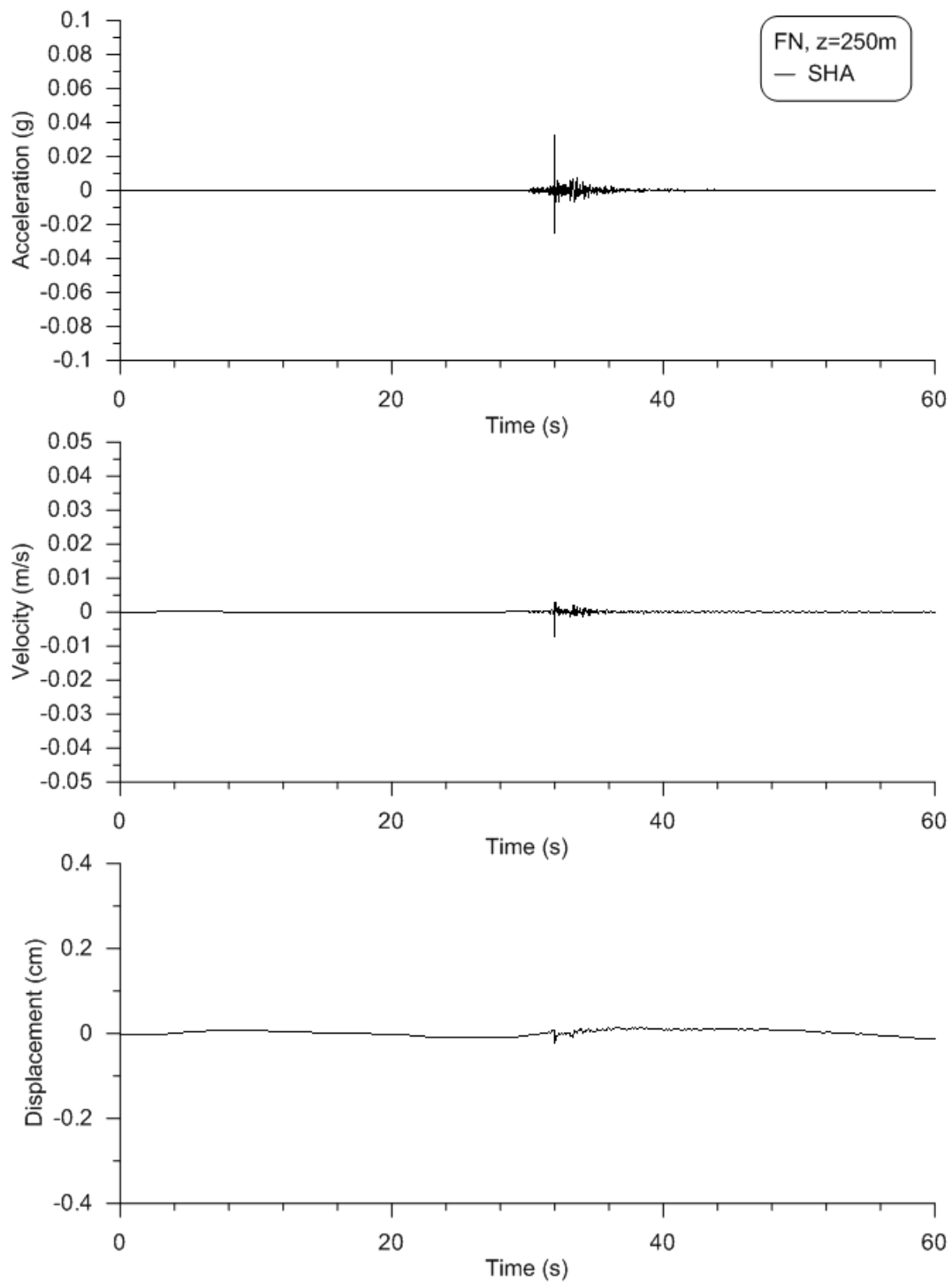


**Figure D4. Corrected acceleration, velocity, and displacement histories for fault normal direction at a depth of 250m.**

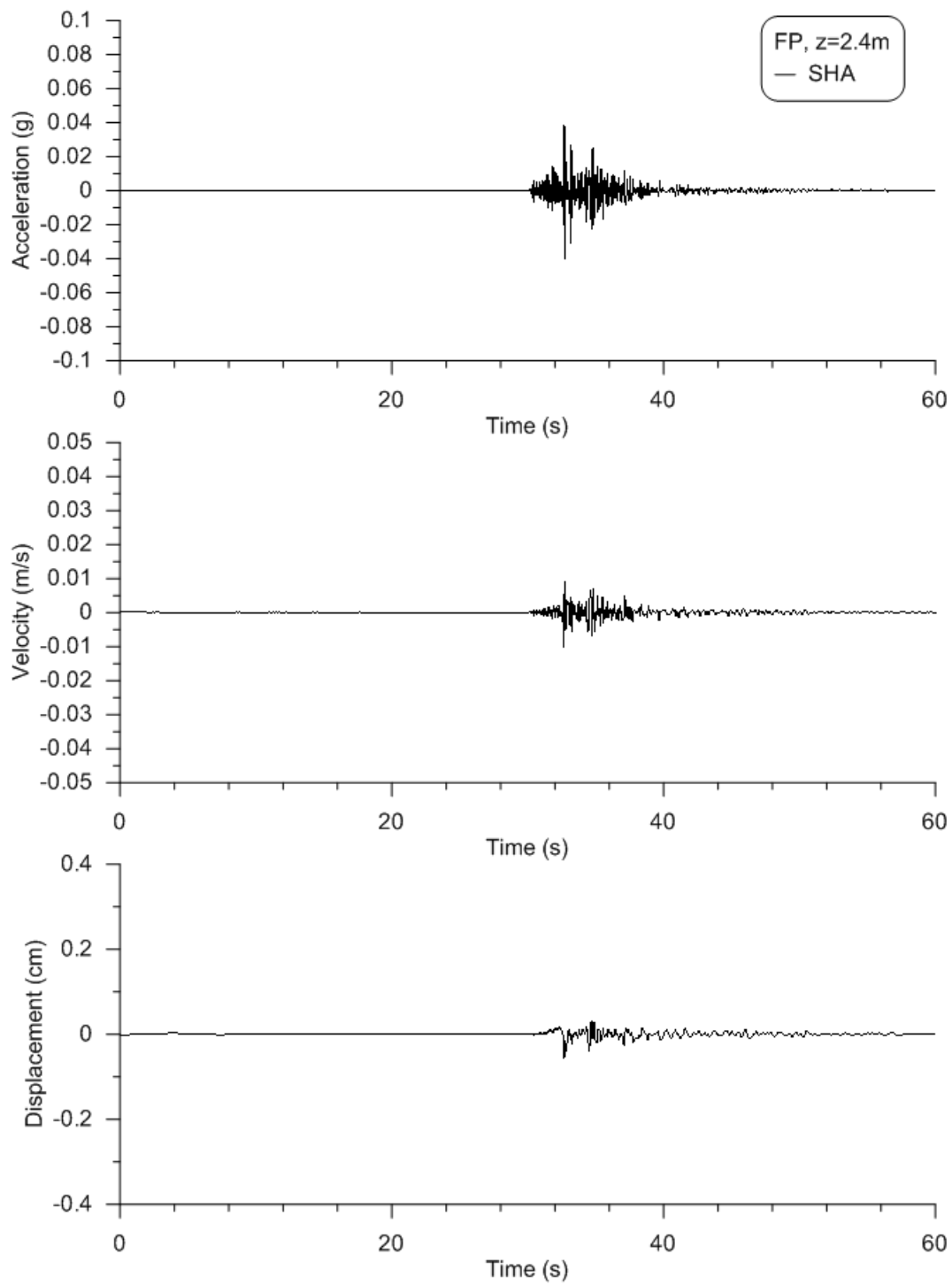


**Figure D5. Corrected acceleration, velocity, and displacement histories for fault parallel direction at a depth of 2.4m.**

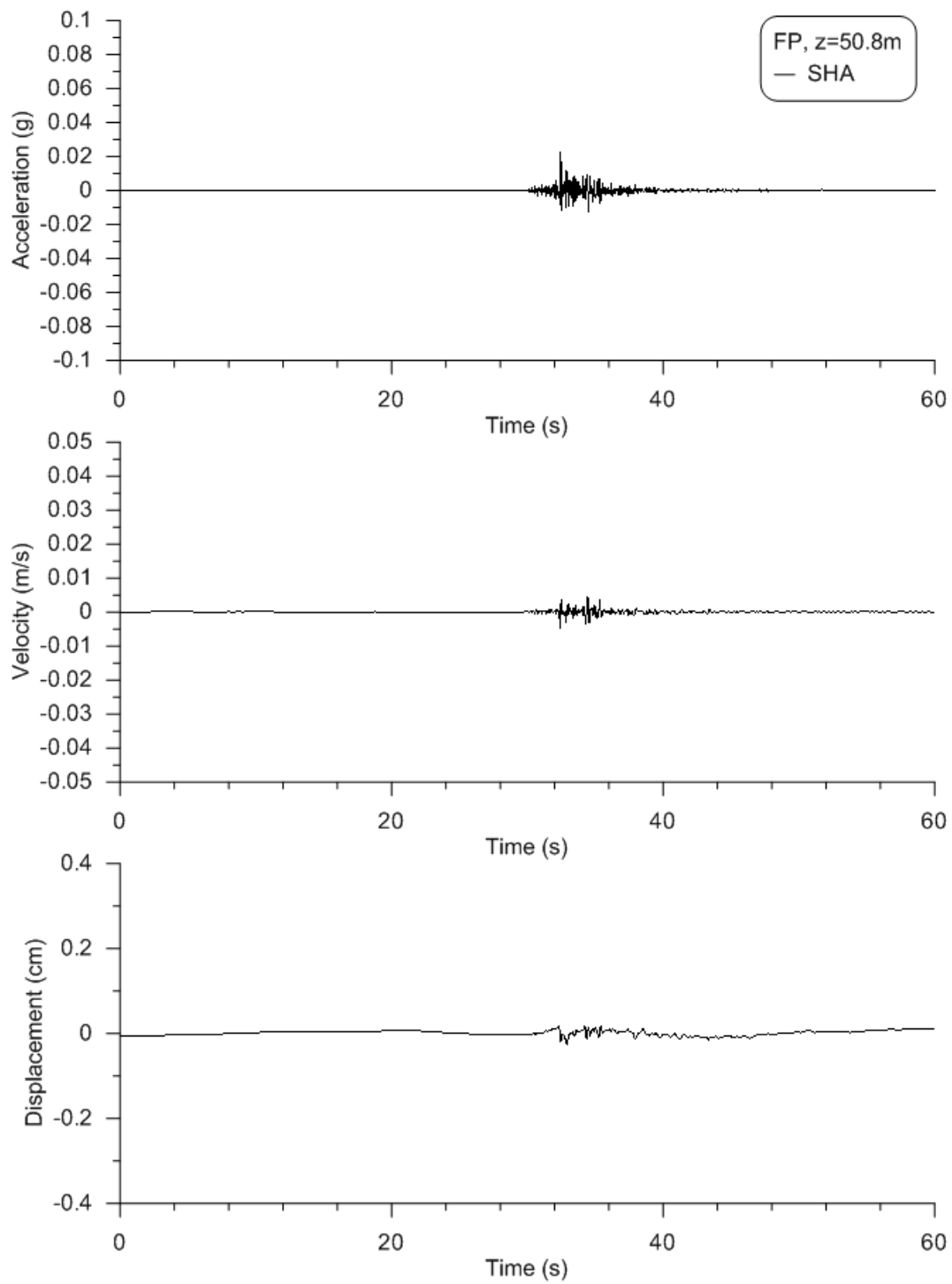


**Figure D6. Corrected acceleration, velocity, and displacement histories for fault parallel direction at a depth of 50.8m.**

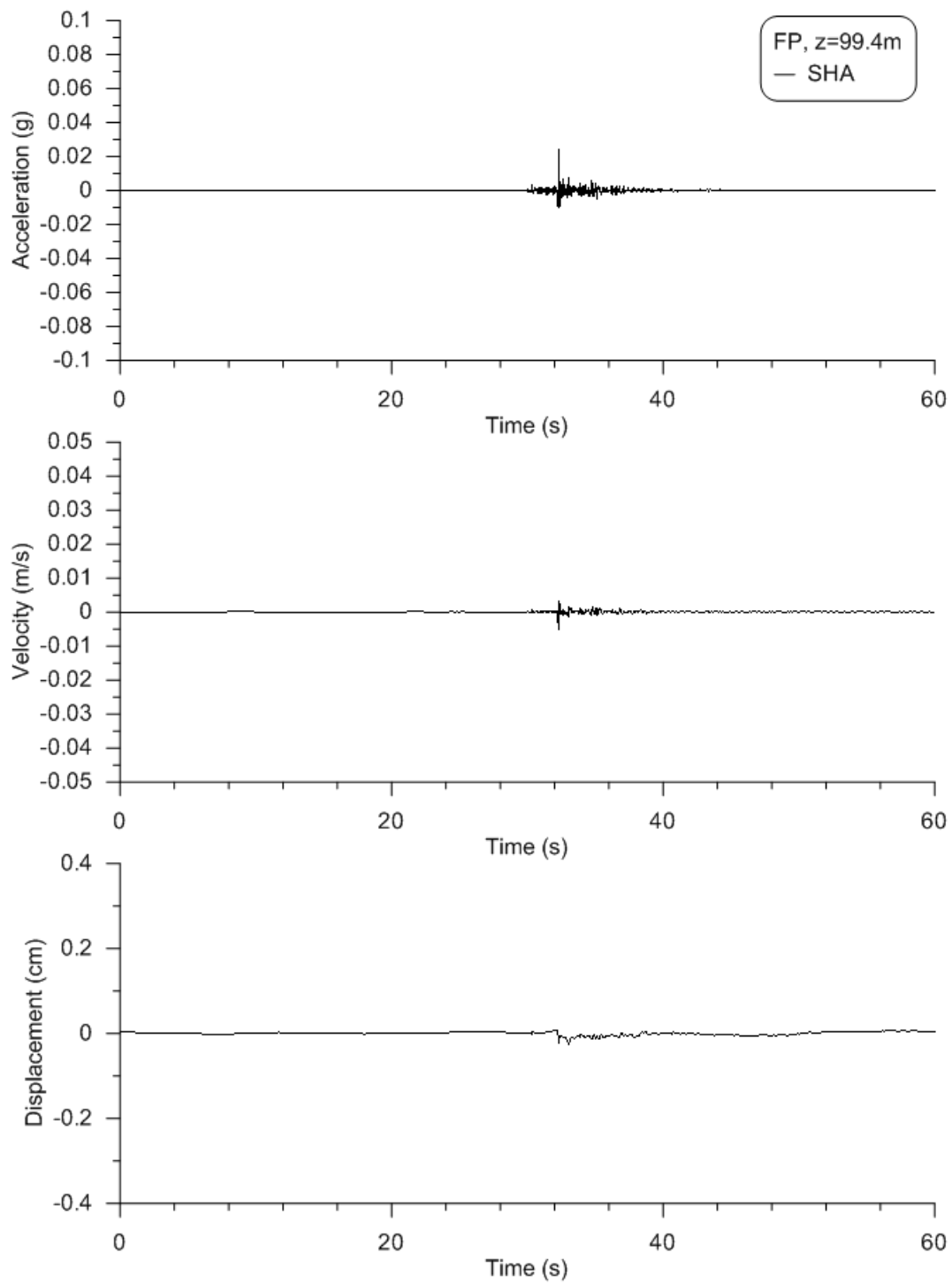


**Figure D7. Corrected acceleration, velocity, and displacement histories for fault parallel direction at a depth of 99.4m.**



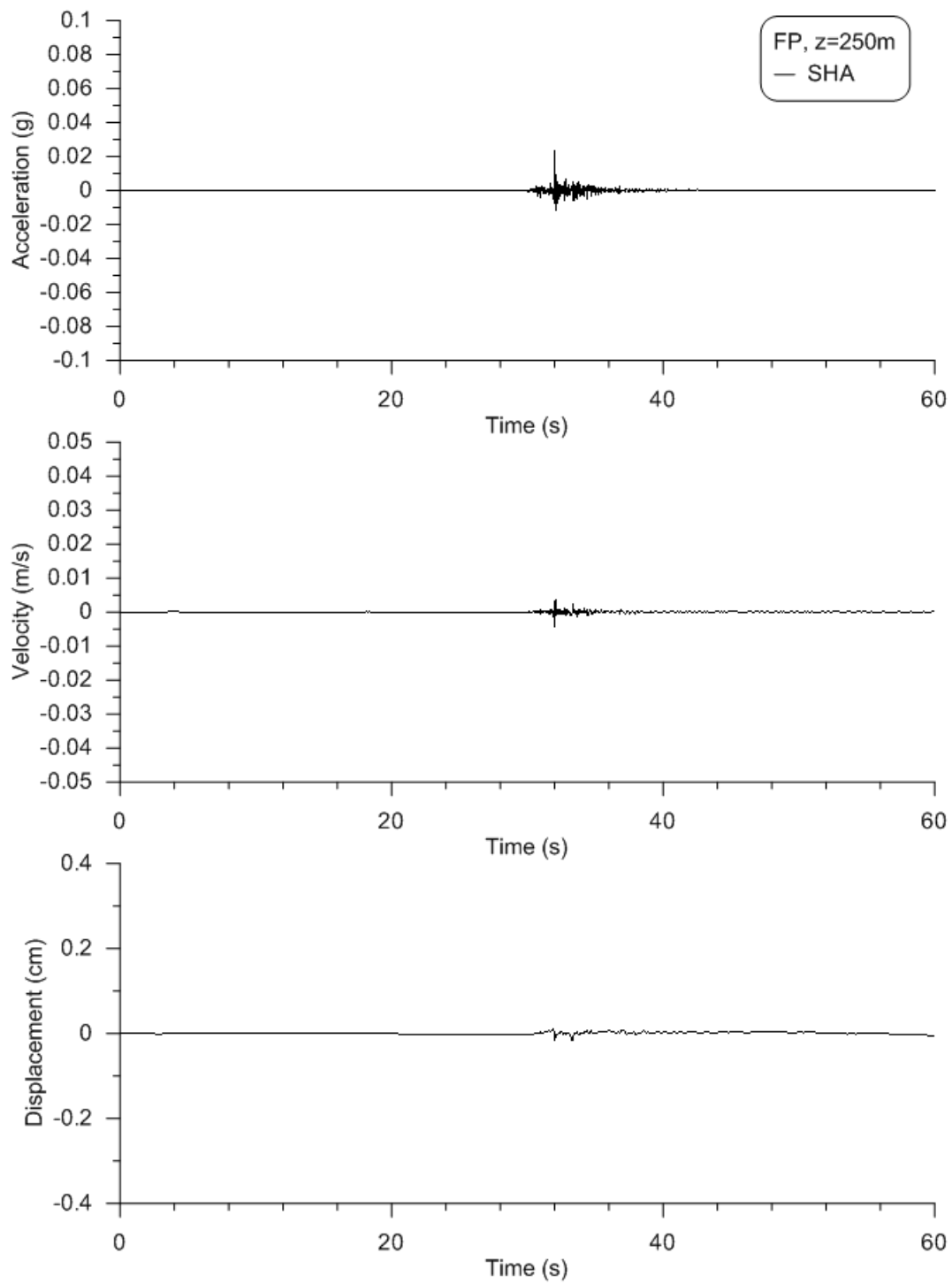


**Figure D8. Corrected acceleration, velocity, and displacement histories for fault parallel direction at a depth of 250m**